Development of High-resolution Tandem Mass Spectrometer with Floated Collision Cell and Curved-field Reflectron

LI, Gang

A Thesis Submitted in Partial Fulfillment
of the Requirements for the Degree of
Master of Philosophy
in
Chemistry

The Chinese University of Hong Kong

December 2007

Thesis/Assessment Committee

Professor Man Chor Chan (Chair)

Professor T-W. Dominic Chan (Thesis Supervisor)

Professor Bo Zheng (Committee Member)

Professor Zongwei Cai (External Examiner)

TABLE OF CONTENTS

Abstract

Since the first introduction of matrix-assisted laser desorption / ionization (MALDI) in 1988, it has become one of the most important mass spectrometry methods for analysis of biomolecules. Because of the pulse-nature of the MALDI method, it is typically coupled to time-of-flight (TOF) mass spectrometer. MALDI-TOFMS can also produce structurally important information by using post-source-decay (PSD) analysis. PSD analysis relies on the analysis of metastable decay fragments of a pre-selected ion using a series of spectra obtained with different reflectron mirror potentials when a dual-stage reflectron is used. Intrinsically, PSD is a relatively low-sensitivity method and is amendable for molecules which can easily undergo metastable dissociation under typical MALDI conditions.

In the project, a home-built collision cell was introduced into our MALDI-TOFMS and the dual-stage reflectron was replaced with a curved-field reflectron to improve the efficiency of a MALDI-TOF instrument for structural analysis. In the design of collision cell, three geometries of collision cells were tested and the field-sharped cylindrical collision cell has the best performance. In the design of curved-field reflectron, analytical equations were used to investigate temporal focusing properties of curved-field reflectron. The method has the advantage of locating the temporal focal points of precursor ions and fragment ions with minimum simulation time. Theoretically, curved-field reflectron should be able to reflect parent ions and daughter ions simultaneously without the necessity of stepping down the reflection voltage. However, our preliminary results indicated that the new curved-field reflectron could only reflect a certain range of masses. It was realized that the origin of this limitation lies on the lateral dispersion of ions of different kinetic energies. With an off-axial detector with limited active area, only a fraction of the fragment/precursor ions could be reflected at a time. To resolve this situation, a coaxial detector has been acquired to improve the transmission efficiency.

摘要

自從 1988 年基質輔助鐳射解吸電離（MALDI）技術被發明，它已經成爲幾種重要的分析生物分子的質譜方法之一。由於它的脈衝的本質，它被應用於飛行時間質譜。通過應用後源破碎分析基質輔助鐳射解吸電離飛行時間質譜能夠給出生物分子重要的結構資訊。通過改變二級反射器的反射電壓，能夠獲得一系列的某個選定的分子離子的亞穩態碎裂碎片的譜圖，後源破碎分析就是基於這些譜圖進行分析。根本上講，後源破碎技術是一種低靈敏度的方法，只適用於分析那些在基質輔助鐳射解吸電離條件下很容易放出亞穩態碎裂碎片的分子。

在本文的研究課題裏，我們試圖給現有的基質輔助鐳射解吸電離飛行時間質譜加進一個自製的碰撞室，將二級反射器替換爲曲線場反射器以提高現有儀器結構分析的效率。在碰撞室的設計中，我們嘗試了三種不同形狀的碰撞室，最後發現尖銳場碰撞室的表現最好。在曲線場反射器的設計中，我們用數學分析方程的方法去分析它的時間聚焦特點，這種方法能夠用最少的模擬時間定位分子離子以及碎片離子的時間焦點。理論上講，曲線場反射器能夠同時聚焦分子離子以及碎片離子而不用調整反射器的反射電壓了。然而我們初步的結果表明曲線場反射器只能夠在一定的質量範圍裏聚焦分子離子和碎片離子。這種限制根源於不同能量的離子在垂直方向的位置分散。離軸檢測器由於具有較小的檢測面積因而只有一部分的碎片及母離子能被同時檢測，爲瞭解決這個問題，我們將會換用同軸檢測器去提高檢測效率。

ACKNOWLEDGEMENT

Deepest gratitude is given to my supervisor, Dr. Dominic T.-W. Chan, for his fruitful as well as unfruitful advices, unlimited patience, guidance and counseling throughout these years. I also want to give my thanks to Ms P. K. Chan for her advices about my project and showing me how to operate the instrument at the beginning of my project. I would like to appreciate Mr. C. B. Leung in the workshop for processing the components used in the new instrument. Besides, thanks are also given to Mr. K. K. Ng, Mr. C. C. Chan, Mr. X. F. Chen and Mr. K. –F. Wu for their technical and professional support in the electronics and computing works, and labmates and roommates in LG52 and LG54 for their encouragement.

Finally, I would like to appreciate my families and friends for their understanding and support these years.

TABLE OF CONTENTS

LIST OF FIGURES

LIST OF TABLES

ABBREVIATIONS

α-CCA	α-cyano-4-hydroxycinnamic acid
ACN	Acetonitrile
AgII	AngiotensinII
CAD	Collisionally activated dissociation
CFR	Curved-field reflectron
CID	Collision induced dissociation
DE	Delayed extraction
DIET	Desorption Induced by Electronic Transition
FWHH	Full width half height
HB	Homogeneous bottleneck
HS	Hard-sphere
IR	Infrared
K.E.	Kinetic energy
LD	Laser desorption
LFR	Linear-field reflectron
MALDI	Matrix-assisted laser desorption/Ionization
m/z	Mass-to-charge ratio
MCP	Microchannel plate
PAGE	Polyacrylamide gel electrophoresis
PSD	Post source decay
SDS	Sodium dodecyl sulphate
SEM	Secondary electron multipliers
TIS	Time ion selector
TOFMS	Time-of-flight mass spectrometer
VUV	Vacuum-ultraviolet

Chapter One
Introduction

1.1 Matrix-assisted laser desorption/ionization (MALDI)

1.1.1 Laser Desorption

The use of laser photons to assist desorption and ionization of involatile and thermal liable compounds can be traced back to early 1970's.[1-5]. Lasers emitting photons of various wavelengths, ranging from vacuum-ultraviolet (VUV) up to infrared (IR), have been used in mass spectrometry. Both continuous and pulsed lasers have also been used. Depending on the wavelength of the laser and the duration of the laser pulse, different mechanisms of desorption/ionization have been postulated. Pulsed lasers have generally been found to be more useful in desorption and ionization of organic molecules. The absorption coefficient of the analyte molecules at the wavelength of the laser photons has been found to influence the success of the laser desorption measurement. For samples with little or no absorption at the laser wavelength, extensive fragmentation of the analyte molecules usually occurs. Intact molecular ions larger than 700 Daltons could not normally be observed. For samples with high absorption coefficient at the wavelength of the laser, intact molecule ions as large as 1,000 Daltons could be observed under suitable laser fluence. All attempts to analyze larger molecules (>2,000 Daltons) failed under direct laser desorption conditions.

1.1.2 Matrix-assisted Laser Desorption/Ionization

Matrix-assisted laser desorption/ionization mass spectrometry was first introduced in 1988.[6,7] It is now one of the powerful analytical techniques for analysis of biomolecular including oligonucleotides,[8] carbohydrates,[9,10] and proteins,[11] In comparison to the common methods used in biomedical sciences for measuring molecular weight, i.e. sodium dodecyl sulphate polyacrylamide gel electrophoresis (SDS-PAGE),[12,13] the MALDI method offers several advantages, such as shorter

analysis time, higher sensitivity and precision of measurement. Although the accessible mass range of MALDI method remains inferior to SDS-PAGE, protein molecules with masses up to several hundred kiloDalton[14,15] have been successfully analyzed at picomole to femtomole level.[16,17,18,19]

The main difference between conventional laser desorption methods and MALDI technique is the use of the "matrix" materials. In MALDI, the sample is normally mixed with a solution of liquid or solid matrix in a molar ratio of analyte-to-matrix in the range of 1:100-1:50,000.[20,21,22,23,24,25] The roles of the matrix in the desorption and ion formation processes have been widely discussed.[26,27,28,29] It is a general consensus that it absorbs laser irradiation and leads to the breakup of a microvolume of the solid materials. Besides, it prevents association or aggregation among sample molecules. It has been postulated that potential matrix materials should have the following properties:[30,31,32,33,34,35] (a) it should have a reasonable high molar extinction coefficient at the wavelength of the laser; (b) it should dissolve in solvent(s) that is/are miscible with that of analyte solution; (c) it should have relatively low heat of sublimation, good vacuum stability and low reactivity with the analyte molecules. In order to be an efficient matrix, it must also be able to generate a high yield of ions from the desorbed analyte molecules[36]. Even though many studies have been conducted on the properties of the matrix materials, discovery of new and effective matrices is still acquired by trial and error method. The structures of commonly used matrices in MALDI are shown in Figure 1.1.1.

Many investigations[37,38,39,40] have been focused on the study of the process(es) of desorption and ionization under MALDI conditions. Different hypotheses have been developed to explain different aspects of the MALDI processes. In the "cool plume model",[41,42] the scenario about the heating and phase transition by laser energy was outlined. After photo energy is deposited onto the matrix, the surface temperature is elevated above the sublimation temperature of the matrix. The matrix molecules are sublimed to gas phase. The plume undergoes a gas dynamic expansion and the

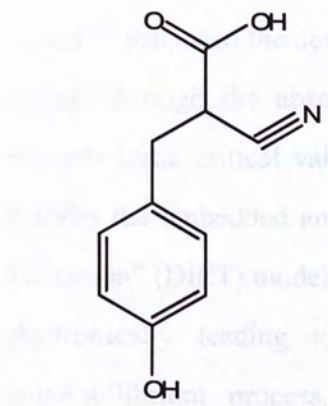

alpha-cyano-4-hydroxycinnamic acid

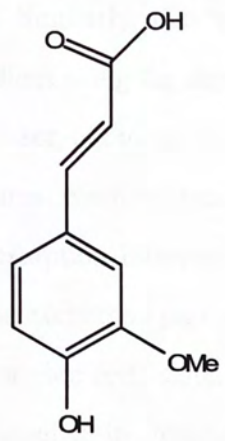

3-methoxy-4-hydroxycinnamic acid

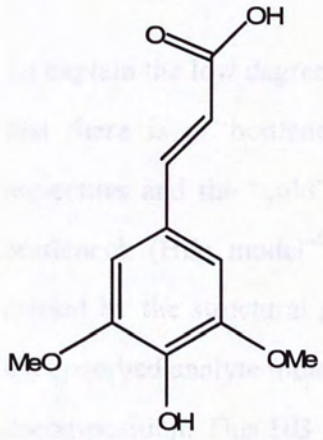

3,5-dimethoxy-4-hydroxycinnamic acid

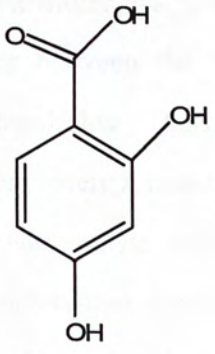

2,5-dihydroxybenzoic acid

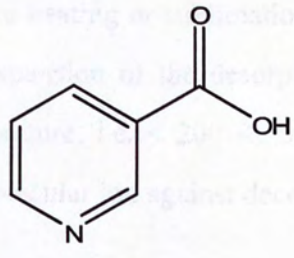

Nicotinic acid

Figure 1.1.1 Structures of common matrices in MALDI.

embedded analyte molecules are desorbed together. Similarly, the "pressure pulse model"[43] proposed the development of a pressure gradient along the depth of the solid sample through the absorption of the penetrating laser photons. As the pressure exceeds some critical values, the surface layer ruptures. Such molecular expansion desorbs the embedded analyte molecules. In the "Desorption Induced by Electronic Transition" (DIET) model,[44,45] the absorbate (matrix) is excited by photons electronically leading to an anti-bonding state or ionized state. As it is a non-equilibrium process, the excited states are usually in repulsive range of interaction potential. Then, the excited particle will experience a repulsion field and leave the surface with some kinetic energies.

To explain the low degree of fragmentation for the analyte molecules, it was proposed that there is a "bottleneck" in which energy transfer between the "hot" matrix molecules and the "cold" analyte molecules is exceptional slow. The homogeneous bottleneck (HB) model[46] proposed that such inefficient energy redistribution was caused by the structural mismatch between the matrix and analyte molecules. Since the desorbed analyte molecules remain internally cold and are therefore not prompt to decomposition. This HB model is further supported by classical molecular dynamics simulation and kinetic models[47]. In the simulation, the analyte molecules/ions were found to have considerately lower temperature than the solid surface provided that the surface heating or sublimation rate is fast enough. In addition, it is also believed that the expansion of the desorption plume might actually cool the plume to very low temperature, i.e. < 200 K. Such cooling effect might further stabilize the entrained biomolecular ion against decomposition.

From the experiments with molecular thermometer, the possibility of having thermal ionization was eliminated. The generally accepted channel of molecular ion formation is chemical in nature, such as proton transfer and adduct-ions formation. Gimon and co-worker have suggested[40] that the formation of analyte ions results from proton-transfer reactions between the electronically excited matrix molecule and the

co-desorbed analyte molecules. Since matrix materials with and without acidic groups were reported effective for MALDI experiments, simple acid-base reaction between matrix and analyte could not be used to explain the ionization process(es) under MALDI conditions. Proton-transfer reactions between analyte and electronically (for UV-laser) or ro-vibrationally (for IR-laser) excited matrix molecules appear to be more promising in explaining ionization process(es) in MALDI.

1.2 Time-of-flight Mass Spectrometry (TOFMS)

The principle of TOFMS is simple. It separates ions of different mass-to-charge ratios based on their respective time-of-flights through the mass spectrometer. The resolving power of time-of-flight is limited but it is still very popular and universal.[48,49] Apart from simple instrumentation, there are many advantages over other mass analyzers. First the operation is simple and the analysis time is short (in microseconds). Second, it has theoretically unlimited mass range. Third, its transmission efficiency and hence the sensitivity is high. Useful spectra can be obtained with very low sample consumption (i.e. fmol to atomol range). Finally, the instrument is relatively inexpensive.

1.2.1 Linear Time-of-flight Mass Spectrometry

A time-of-flight mass spectrometer measures the mass-dependent time for the ions of different mass-to-charge ratios to move from the ion source to the detector (Figure 1.2.1.). This requires a well-defined start time. Therefore, ions are either formed by a pulsed ionization method (e.g. matrix-assisted laser desorption/ionization, or MALDI), or extracted by a rapid electric field switching to release the ions from the ion source within a very short time.

The kinetic energy (KE) of an ion leaving the ion source is given by:

$$KE = zeV = \frac{1}{2}mv^2 \qquad (1.2.1)$$

where z is the number of charge of the ion, e is the unit electronic charge, V is the acceleration voltage in the ion source, m is mass of the ion, and v is velocity of the ion after leaving the ion source. The flight time (t) of an ion from the ion source to the detector is:

$$t = \frac{L}{v} \qquad (1.2.2)$$

where L is the length of flight tube of the mass spectrometer. Substituting equation (1.2.2) into equation (1.2.1), the relationship between flight time (t) and mass-to-charge ratio (m/z) of the ion is given:

$$t = L\sqrt{\frac{m}{e}\frac{1}{2V}} \qquad (1.2.3)$$

Using equation 1.2.1-1.2.3, the mass of an ion from its flight time in the mass spectrometer can be determined.

1.2.2 Reflectron Time-of-flight Mass Spectrometer

Reflectron (or ion mirror) was first introduced by Mamyrin[50] to improve mass resolution in time-of-flight mass spectrometry. Since then, numerous development of reflectrons have been made for the purpose of enhancing energy focusing power. Reflectron is a time-compensating device, which corrects the time dispersion due to the initial kinetic energy distribution of the ions. It compensates the initial energy spread by adjusting the length of flight path for ions of different kinetic energies: high energy ions can penetrate deeper into the reflectron and spend more time in the reflectron than the low energy ions. However, in the drift region the high energy ions spend less flight time than the low energy ion, so high and low energy ions may reach the detector at the same time and resulting in higher time resolution.

The reflectron is located at the end of the linear flight tube (Figure 1.2.1.). It usually

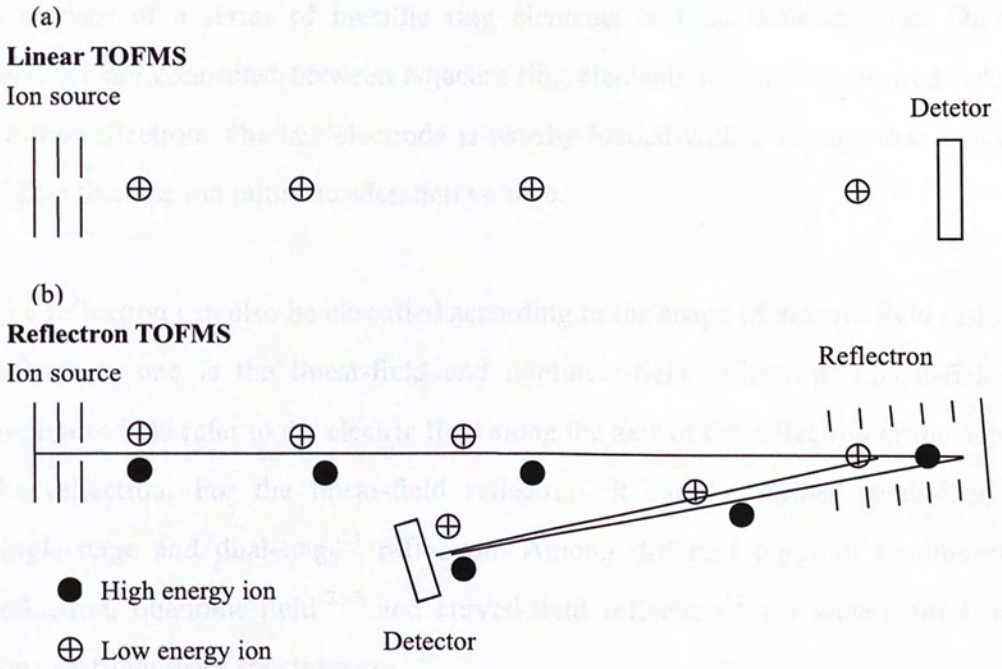

Figure 1.2.1 Schematic diagram of linear (a) and reflectron (b) TOFMS.

comprises of a series of metallic ring elements with or without grids. Different resistors are connected between adjacent ring elements to generate desired potential on the reflectron. The last electrode is usually loaded with a voltage that is slightly higher than the ion initial acceleration voltage.

The reflectron can also be classified according to the shape of electric field inside the reflectron: one is the linear-field and nonlinear-field reflectron. Linear-field and nonlinear-field refer to the electric field along the axis of the reflectron or the depth of the reflectron. For the linear-field reflectron, it can be further subdivided into single-stage and dual-stage[51] reflectron. Among different types of nonlinear-field reflectron, quadratic-field[52,53] and curved-field reflectron[54] are widely used in the time-of-flight mass spectrometry.

1.2.2.1 Linear-field Reflectron

The single-stage reflectron is the simplest type of ion reflectron. A homogeneous reflecting electrostatic field is created between two parallel flat grids. The first grid constitutes the entrance of the ion mirror, and the second the end. A detector is usually places behind the reflectron for linear time-of-flight experiments when the reflectron is grounded. In order to improve the homogeneity of the field in the reflectron a number of equally spaced ring electrodes are usually placed between the end and the first electrodes, connected by a chain of equal value resistors. Mass measurement in a single-stage ion reflectron is obtained by applying the following equation:

$$\frac{m}{q} = (at + b)^2 \qquad (1.2.4)$$

where t is the time-of-flight, m and q are the mass and charge of the ion, respectively, a and b are calibration constants that depend on instrument dimensions. In practice, a and b are determined experimentally using the flight times of two or more calibrant ions in a mass spectrum.

The mass resolution that can be obtained using this type of mass spectrometer is limited by the temporal width of the initial ion pulse from the ion source, and the initial kinetic energy distribution of the ions, as it only corrects to the first order of approximation for the initial velocity spread:

$$t = \frac{L}{v_0}\left[2 + \left(\frac{\delta}{v_0}\right)^2 - \left(\frac{\delta}{v_0}\right)^3 + ...\right] \qquad (1.2.5)$$

where t is the time-of-flight, v_0 is the initial velocity of the ions and δ is a deviation in the initial velocity.

In a two-stage reflectron, two separate homogeneous field regions, of different potential gradient, are utilized. A schematic diagram demonstrating the use of two-stage ion reflectron is shown in Figure 1.2.2. By choosing mirror voltages and dimensions to match the lengths of the field-free region, it has been shown that it is possible to solve Equation 1.2.5 to the second order of approximation.[110,111,112] The geometry is particularly useful for analyzing ion beams with broad kinetic energy distributions.

Using the conventional linear-field reflectron, flight time dispersion for ions of the same mass-to-charge (*m/z*) ratio but slightly different kinetic energies can be minimized. However, this type of reflectron time-of-flight instrument has limited capability in acquiring structural information by measuring fragment ions derived from metastable dissociation (or the so-called post-source decay) or collision-induced dissociation of a time-gated precursor ion. Using a single-stage linear reflectron, all fragment ions can, in principle, be detected simultaneously together with the residual precursor ions. Because of the large dispersion of kinetic energy, fragment ions of different m/z values are however focused at different temporal positions. Using a point detector, only one particular m/z ion can be time-focused. This leads a significant deterioration of the spectral resolution. One practical solution involves the use of two-stage reflectron mirror. By systematically reducing the reflectron voltage, the time-focusing position for fragment ions of different *m/z* value can be shifted to

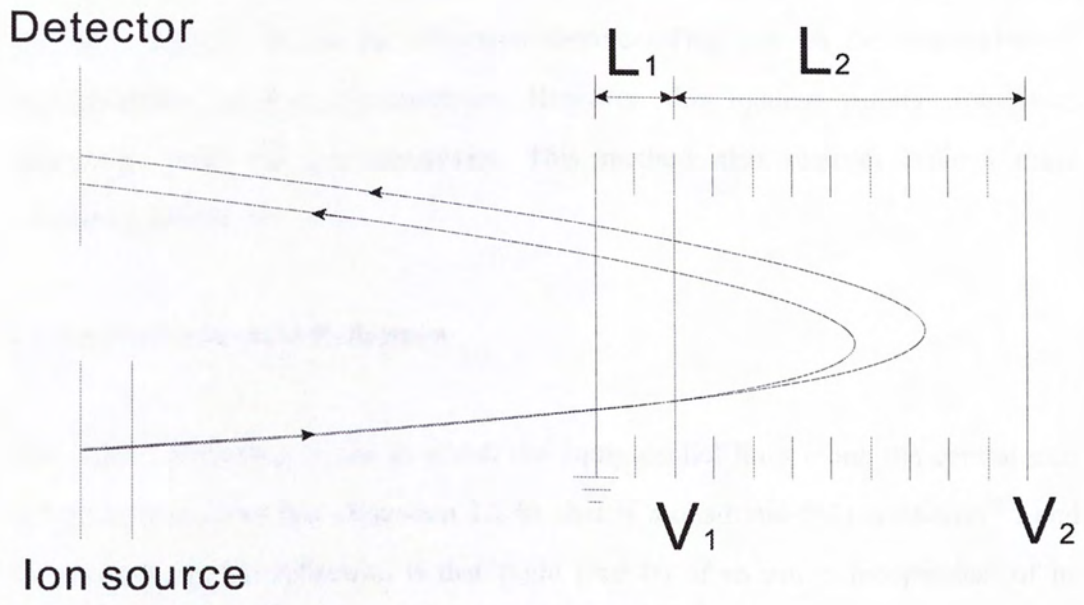

Figure 1.2.2 Schematic diagram of two-stage reflectron.

V_1 — Applied potential to create first homogeneous field region.

V_2 —Applied potential to create second homogeneous field region.

L_1 —Length of first potential gradient of ion mirror.

L_2 —Length of second potential gradient of ion mirror.

the same location, i.e. at the reflectron detector. This enables the acquisition of high-resolution product ion spectrum. However, this method suffers from long acquisition time and low sensitivity. This method also requires tedious mass calibration procedure.

1.2.2.2 Nonlinear-field Reflectron

The "ideal" reflectron is one in which the equipotential lines along the central axis follow a square root law (Equation 1.2.6), that is a quadratic-field reflectron[113], and the property of this reflectron is that flight time (t) of an ion is independent of its kinetic energy to infinite order (Equation 1.2.7):

$$V = ax^2 \tag{1.2.6}$$

$$t = C + \pi\left(\frac{m}{2ea}\right)^{1/2} \tag{1.2.7}$$

where V is the potential along the central axis, a is the slope of the quadratic field, x is the distance into the reflectron from its entrance, C is a constant and m is mass of the ion. Since quadratic field reflectron focuses the ions at the entrance and exit of the reflectron, there is no drift space[114] from the ion source to the detector. This imposes a practical problem in other accessories, such as mounting collision cell and time ion selector within the spectrometer. A system including two ion mirrors[115] may be a solution to this problem. In such a system, the first reflectron is a linear-field reflectron, which provides the temporal focus necessary for the second quadratic-field reflectron. The collision cell as well as the detector is mounted at the entrance and the exit of the second reflectron.

Another type of nonlinear-field reflectron is curved-field reflectron (CFR) proposed by Cotter's group, which offers a superior mean to focus product ions and parent ions simultaneously as compared to the linear-field reflectron (LFR).[116,117,118] In a TOF equipped with a CFR, fragment ions and precursor ions in PSD and CID analysis are

time-focused at nearby positions in the field-free region, so that product ions and precursor ions can be detected simultaneously with reasonable resolution using a point detector. There is no need to mount the collision cell and the detector at the entrance and exit of the reflectron.

1.3 Structural Analysis Using Time-of-flight Mass Spectrometry

MALDI-TOFMS can also provide the structural information of biomolecules (protein, peptide,[57,58] oligonucleotides,[59] oligosaccharides[60,61,62,63] and conjugates[64] etc.) by using post-source decay (PSD) analysis.[65,66,67,68,69] The term post-source decay refers to the fragmentation of molecular ions during their flight time before the ion reached the detector of the mass spectrometer (Figure 1.3.1.). Ions are formed and accelerated in the ion source. After leaving the ion source, all ions have the same kinetic energy, most of them are still unfragmented precursor molecular ions and they have already acquired sufficient internal energy by various means (gas-phase collisions, laser irradiation, thermal mechanisms, etc.). During their flight through the field-free drift region some of the ions undergo unimolecular dissociation into product ions. The product ions have basically the same velocity as their precursors, but differ in their kinetic energies depending on the product ion mass:

$$E_f = \frac{m_f}{m_p} E_p \qquad (1.3.1)$$

where m_f and E_f are mass and kinetic energy of product ions respectively, m_p and E_p are mass and kinetic energy of precursor ions respectively.

Since the product ions and precursor ions have the same velocity, they will spend the same flight time passing through the flight tube in the linear TOFMS. As a result, the linear TOFMS cannot differentiate the product ions and precursor ions based on their flight times. In the case of the reflectron TOFMS, the product ions and precursor ions

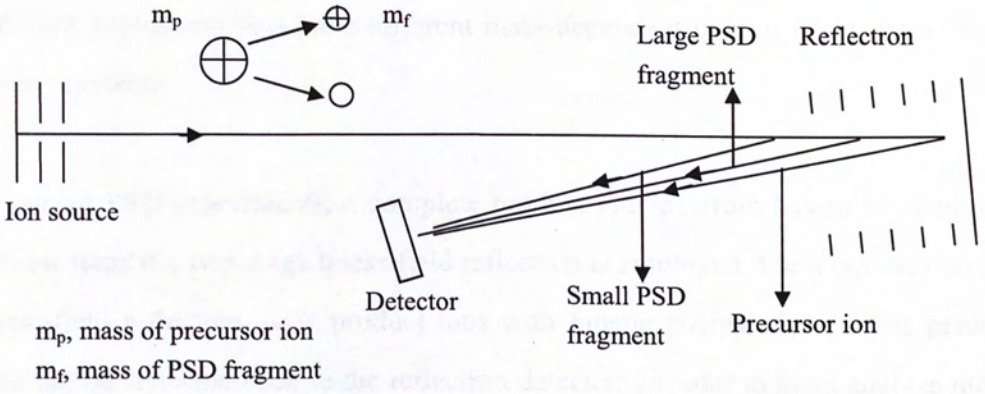

Figure 1.3.1 Principle of PSD analysis in MALDI-TOFMS.

have different mass-dependent kinetic energy, and will be reflected in the reflectron at different depths and thus have different mass-dependent overall flight times through the instrument.

In typical PSD experiments, a complete product ion spectrum has to be acquired in several steps if a two-stage linear-field reflectron is employed. For a typical two-stage linear-field reflectron, only product ions with kinetic energy close to the precursor ions can be reflected back to the reflectron detector. In order to mass analyze the low kinetic energy product ions (i.e. low mass product ions), multiple spectra have to be acquired with the reflectron voltages being reduced successively. Finally, segments of these spectra will be concatenated by the software and mass calibrated.[70] This method of fragment ion detection is not unique to MALDI analysis and has been employed earlier in PDMS and SIMS studies for metastable ions.[71,72]

In addition to the linear-field reflectron,[73] some kinds of nonlinear-field reflectron[74] such as quadratic-field reflectron and curved-field reflectron[75] have also been used for PSD analysis. These nonlinear-field reflectron allows the acquisition of all metastable ions in one spectrum without the need for stepping down the reflection voltage.

Post-source decay analysis has some intrinsic limitations, such as low fragmentation efficiency, long acquisition time and high detection limit. For instance, some analytes may not dissociate into fragments during their flight times under MALDI conditions, hundreds of laser shots are therefore needed to co-added to obtain good intensity of the peaks for the product ions. The amount of sample required in a typical PSD analysis is substantially more than that of other tandem mass spectrometry methods.

Regarding to the fragmentation efficiency, it can be improved by using the technique of collision-induced dissociation (CID).[110,111,112,113] Collision-induced dissociation (CID), also known as collisionally activated dissociation (CAD), is a method to fragment molecular ions in the gas phase (Figure 1.3.2.).[114] The molecular ions are

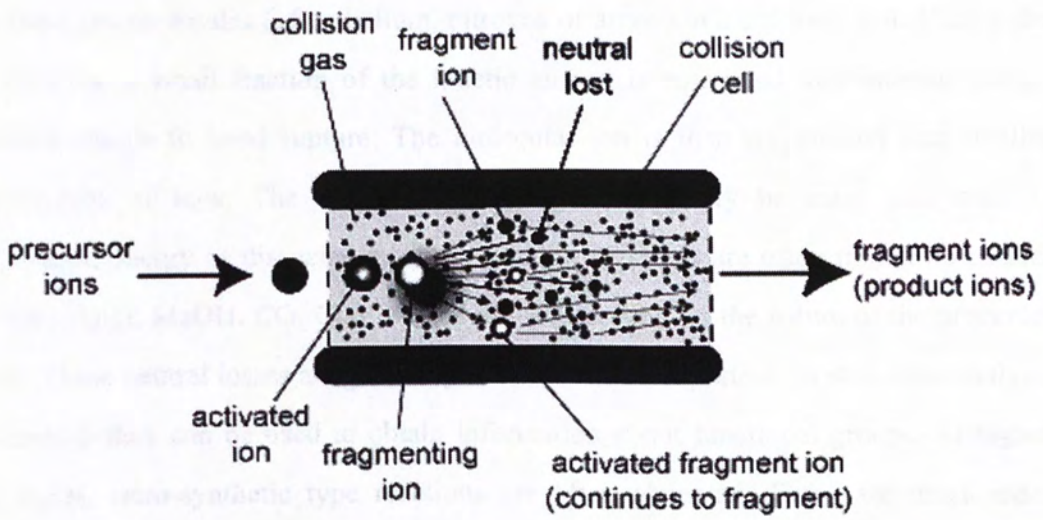

Figure 1.3.2 Schematic diagram of collision-induced dissociation (CID) process.

usually accelerated to high kinetic energy, selected and then allowed to collide with neutral gas molecules (often helium, nitrogen or argon) in a collision cell. During the collisions, a small fraction of the kinetic energy is converted into internal energy which results in bond rupture. The molecular ion is then fragmented into smaller molecules of ions. The fragment ions can subsequently be mass analyzed. At threshold energy of dissociation, fragmentation reactions are often limited to neutral losses (H_2O, MeOH, CO, CO_2, MeCN etc.) depending on the nature of the precursor ion. These neutral losses are generally not considered important for structural analysis, although they can be used to obtain information about functional groups. At higher energies, retro-synthetic type reactions are often observed. These are much more important for structure characteristic, and often result in cleavage of the molecule at characteristic positions. If the energy is too high, C-C bond cleavage might occur leading to uncontrolled fragmentation.

1.4 Project Objectives

The fragmentation efficiency of PSD analysis can be improved by introducing a collision cell into the field free region of the TOF analyzer for collision-induced dissociation (CID) analysis. With collision-induced dissociation,[76,77] higher fragmentation efficiency of the precursor ions and the employment of a curved-field reflectron can reduce the acquisition time of obtaining a complete spectrum of product ions.

In this project, a matrix-assisted laser desorption/ionization time-of-flight mass spectrometry (MALDI-TOFMS) was modified into a tandem mass spectrometry (MS/MS) by replacing the two-stage linear-field reflectron with a curved-field reflectron and adding a home-built collision cell in the field free region of the flight tube. By incorporating the collision cell, not only PSD analysis but the CID analysis can also be performed in the instrument. In the design of collision cell, spatial and

temporal dispersions of the CID fragment ions generated in three geometries of collision cells (segmented cylindrical collision cell, cylindrical collision cell with a focus lens and field-sharped cylindrical collision cell) were investigated. In the design of curved-field reflectron, the temporal focusing properties of curved-field reflectron were studied using the analytical equations. Based on the simulation results a curved-field reflectron was constructed and tested.

Chapter Two
Instrumentation and Experimental

2.1 Instrumentation

In the Bruker MALDI-TOFMS (Figure 2.1.1), there are two operation modes: linear and reflectron mode. In linear mode, a detector is located at the end of flight tube (after the reflectron). After leaving the ion source, ions arrive at the detector and signal is recorded by the acquisition system. In reflectron mode, a two-stage reflectron is mounted at the end of flight tube, ions are reflected by the reflectron before they reach the reflectron detector. As mentioned previously, the reflectron is an energy-compensation device, so the mass resolution of reflectron mode analysis is higher than that of linear mode.

The Bruker MALDI-TOFMS consists of following parts: Laser system, Ion source, Deflector, Time ion selector, Reflectron and Detector (Figure 2.1.1.).

2.1.1 Laser System

The laser system provides a pulsed laser light at defined wavelength and intensity on a small target. The system consists of a pulsed UV N_2 laser with 337 nm wavelength and 3 ns pulse width. An attenuator allows fine adjustment of the laser fluence. The beam splitter is used to direct 5% of the laser light to a photodiode thus starting the time-of-flight measurement and triggering data acquisition by the digitizer. In addition, a lens system was installed to focus the laser beam and a mirror system to direct the beam into ion source on the target.

2.1.2 Flight Tube and Vacuum System

The flight tube is made of stainless steel and is about 120 cm long. The instrument is evacuated to a pressure of 10^{-6} to 10^{-7} mbar by a turbomolecular pump (balzer, Germany) backed by a rotary pump. Pressure inside the instrument is monitored by an

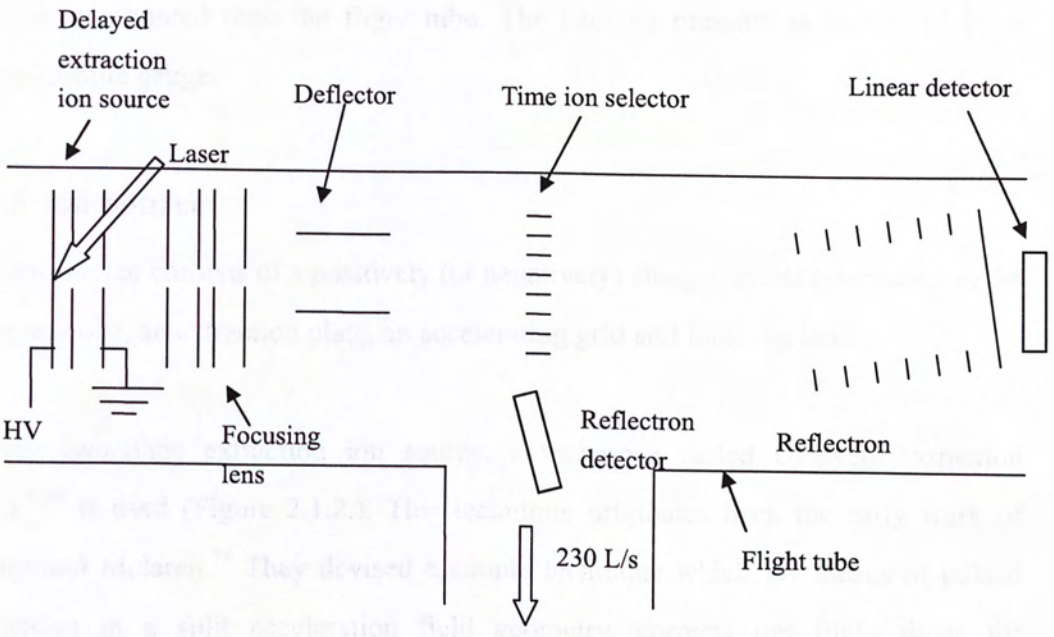

Figure 2.1.1 Schematic diagram of MALDI-TOFMS.

ion gauge mounted onto the flight tube. The backing pressure is monitored by a thermocouple gauge.

2.1.3 Ion Source

The ion source consists of a positively (or negatively) charged metal electrode, i.e. the sample probe, an extraction plate, an accelerating grid and focusing lens.

In this two-stage extraction ion source, a technique called Delayed Extraction (DE)[78,79] is used (Figure 2.1.2.). This technique originates from the early work of Wliey and Mclaren.[78] They devised a simple technique which, by means of pulsed extraction in a split acceleration field geometry, corrects ion flight times for distributions of either initial ion velocity or ion position (but not for both at the same time). Fortunately enough, in MALDI spatial and velocity distributions of freely expanding particles are correlated to each other which allows one to find conditions for a simultaneous velocity and spatial focusing. While delayed extraction parameters (delay time, pulsed field strength) which must be applied for ultimate improvements are mass dependent, broader m/z ranges of several kDa can be covered at slightly compromised performances.

Delayed extraction technique uses a pulsed, time-delayed two-stage extraction potential to avoid the undesired initial conditions.[80,81,82] During the formation of ions in the source, ions with the same mass may have different initial velocity, which can cause poor mass resolution in the mass spectrum. In order to compensate the initial velocity distribution, time-delay extraction is proposed:[83,84,85,86,87,88] extraction voltage is applied to the extraction plate after a delay time rather than immediately when the ions are formed. Under delayed extraction, ions with low initial velocity can obtain more kinetic energy in the acceleration region than the ions with high initial velocity, so the ions with the same mass may have almost the same kinetic energy after leaving the ion source, and can reach the detector at the same time, which results in an

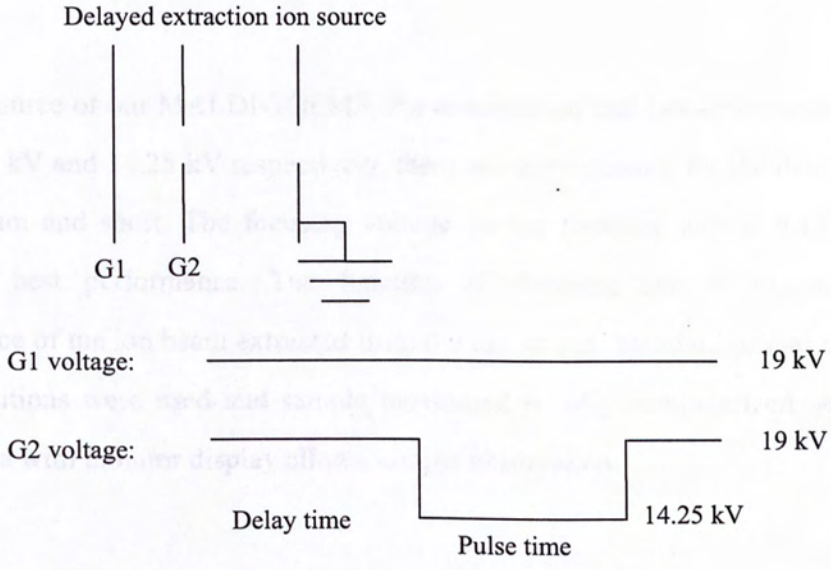

Figure 2.1.2 Principle of delayed extraction (DE). When the delay extraction is on, an extraction voltage (14.25 kV) is applied to G2 after a delay time. The ions are extracted by the electric field force between G1 and G2 during the pulse time.

improvement in the mass resolution.

In the ion source of our MALDI-TOFMS, the acceleration and extraction voltage are set at 19.00 kV and 14.25 kV respectively, there are three choices for the delay time: long, medium and short. The focusing voltage on the focusing lens is 9.15 kV to obtain the best performance. The function of focusing lens is to minimize thedivergence of the ion beam extracted from the ion source. Standard probes with 10 defined positions were used and sample movement is fully computerized. A video CCD camera with monitor display allows sample observation.

2.1.4 Deflector and Ion Selector

Deflector is used to remove the unwanted low mass ions, such as matrix and matrix cluster ions. Deflecting these ions can improve the sensitivity of high mass ions because detector saturation is avoided. The deflector is mounted behind the ion source and consists of two electrodes which are applied with 1.5 kV/cm. The electric field is orthogonal to the ion beam and is on off for a short period of time after the ion generation event. By the orthogonal field, ions are deflected away from the central optical axis thus cannot reach the detector.

In PSD analysis, precursor ions have to be selected to enter the reflectron but ions with other masses are not desired to be detected, while the time ion selector can allow the selected-ion to pass through but deflect ions with different mass, which can be achieved by a time-dependent pulse voltage applied to the time ion selector.

The time ion selector in our MALDI-TOFMS consists of 10 parallel 20 mm-length 2 mm-width nickel-chromium ribbon spaced 2 mm apart to form a venetian blind structure (Figure 2.1.3). The pulse on the five of ten ribbons is from 700 V to ground then to 700 V, and the other five ribbons are pulsed from -700 V to ground then to

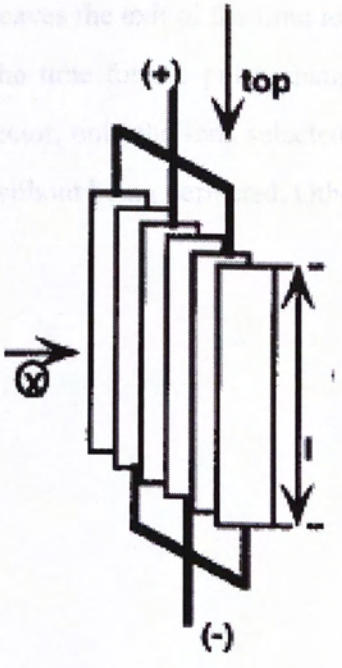

Figure 2.1.3 The schematic diagram of time ion selector. '+' and '-' mean the voltage applied to the metal strip is positive or negative.

-700 V, the pulse is shown in Figure 2.1.4. The pulse start time is the time when the selected-ion reaches the entrance of the time ion selector, and the pulse end time is the time when the selected-ion leaves the exit of the time ion selector. 20 ns indicated in the figure is the rise time: the time for the pulse change from 700 V/-700 V to ground. Under the time ion selector, only the ions selected can pass through the ion selector and reach the detector without being deflected. Other ions would be deflected and hit the wall of flight tube.

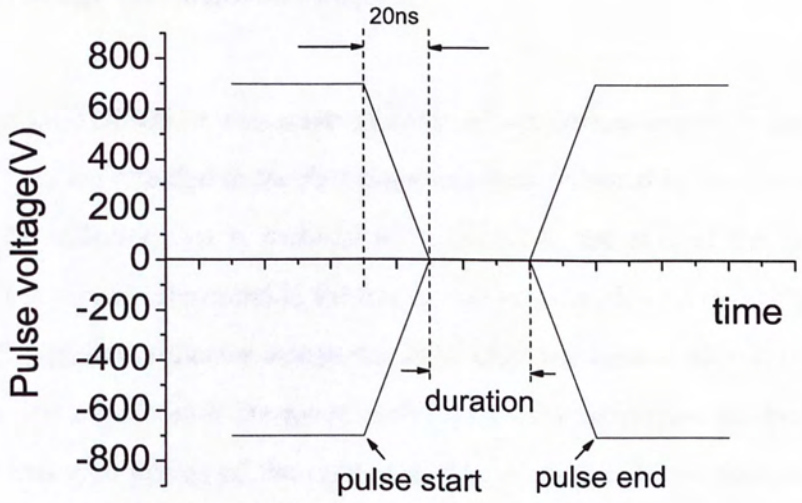

Figure 2.1.4 Pulse applied to the single-stage time ion selector. 20 ns indicated in the figure is the rise time: the time for the pulse change from 700 V/-700 V to ground. Duration is the time of pulse applied.

2.1.5 Two-stage Gridless Reflectron

In the MALDI-TOFMS, a two-stage gridless reflectron/ion mirror is employed. In this setup, ions are retarded in the first stage and then reflected by the second stage at +20 kV. The reflector axis is inclined with respect to the axis of the ion beam to reflect the ion packets generated in the ion source onto an off-axis microchannel plate detector. The gridless reflector design results in high ion transmission and resolution. In addition, the sensitivity is increased by focusing of the divergent ion beam because of the ion lens type design of the reflectron. The two-stage linear-field reflectron in the current instrument consists of 15 metal rings (80 mm outer diameter, 40 mm inner diameter and 1 mm thickness) with the overall length 140 mm. There are 14 resistors welded between two adjacent metal rings, and the resistance of first two resistors is 27.5 MΩ and the rest are 5 MΩ. The potential inside the reflector is presented in Figure 2.1.5.

2.1.6 Detectors, Digitizer and Computer system

For the detection of ions, either discrete dynode secondary electron multipliers (SEM) of the venetian blind or focused mesh type are used, as well as microchannel plate detectors (MCP) or a combination of both, with a single MCP, followed by an SEM. In all of these cases, the dependence of the ion-electron conversion on the impact velocity of the ions is a major problem for the detection of high mass ions.

Off-axis detector and coaxial detector are two kinds of detectors used in TOFMS (Figure 2.1.6.). Off-axis[102] detection has the advantage of geometrically blanking all secondary ions or electrons formed at the grids of the reflector. As can be seen from the figure, however, they require a much larger detector, since PSD ions reflected at different positions within the reflector are laterally spread over the detector. Coaxial[103] detection, on the other hand, is possible with a simpler instrumental setup,

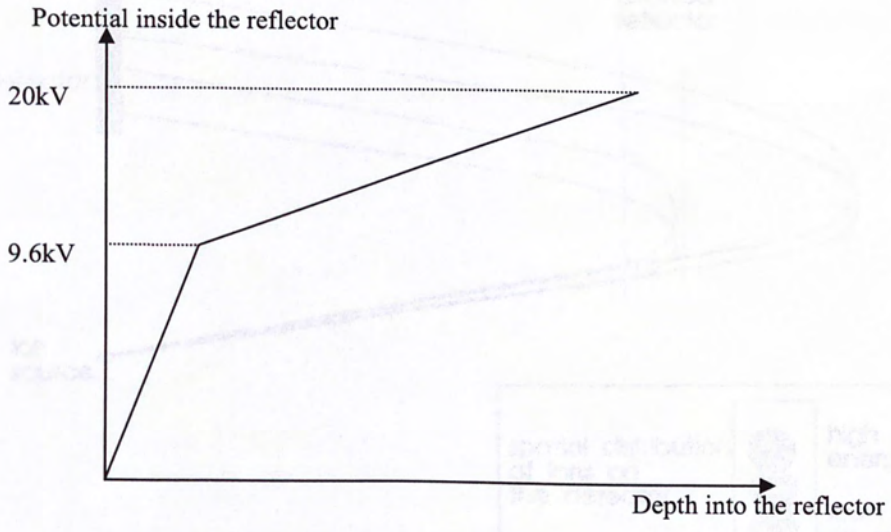

Figure 2.1.5 Potential inside the two-stage linear-field reflectron.

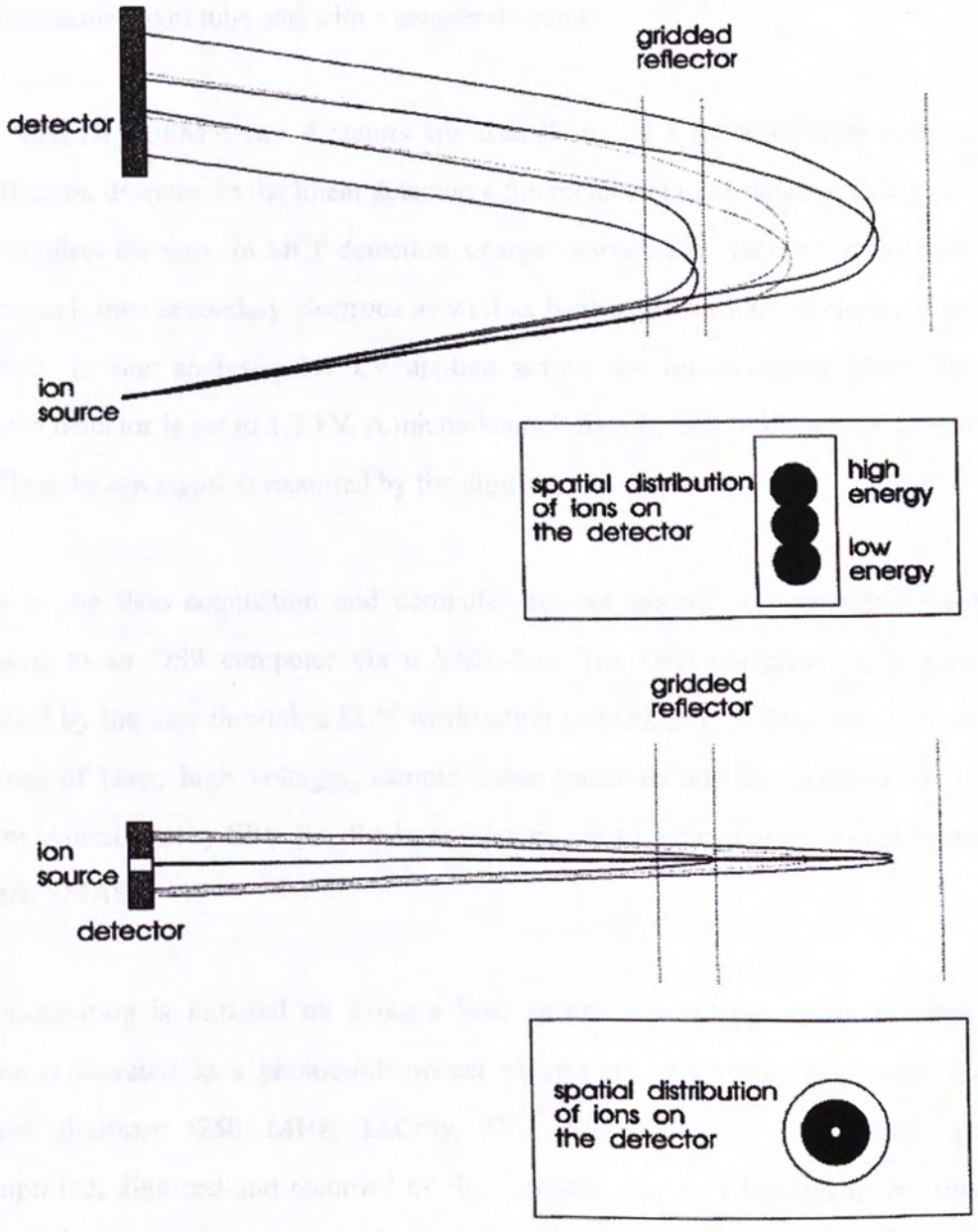

Figure 2.1.6 Scheme of coaxial detector (lower) and off-axis detector (upper).

within the same flight tube and with a smaller detector.

In the MALDI-TOFMS, two detectors are used (Figure 2.1.1.). The linear detector and reflectron detector. In the linear detector, a microchannel plate detector (MCP) is used to collect the ions. In MCP detection, charged particles are incident at the input of a channel, then secondary electrons as well as further generations of electrons are generated. In our analysis, 1.5 kV applied across the microchannel plate. The reflectron detector is set to 1.7 kV. A microchannel plate is used to detect the formed ions. Then the ion signal is recorded by the digitizer.

Center to the data acquisition and computer control system is a microprocessor interfaced to an OS9 computer via a VME-bus. The OS9 computer is, in turn, controlled by the user through a SUN workstation (SPARC20) via Ethernet. Settings for firing of laser, high voltages, sample target positions and the position of the gradient neutral density filter (i.e. the laser fluence) are all computer-controlled by the software XMASS.

Data acquisition is initiated by firing a laser pulse. A small portion of the laser photons is directed to a photodiode which in turn triggers a start signal for the transient digitizer (250 MHz, LeCroy, US). Signals from the detector are pre-amplified, digitized and recorded by the digitizer. The digitized signals are then transferred to the SUN workstation for display and processing. The SUN workstation serves as a user-friendly terminal for instrument control, data acquisition and also as a powerful data processing device.

2.2 Experimental

To compare the performance of the MALDI-TOFMS before and after modification, PSD spectra of Angiotensin II were acquired.

2.2.1 Sample Preparation

Matrix stock solution was prepared by saturating α-cyano-4-hydroxycinnamic acid (α-CCA) in the solvent (mixture of acetonitrile (ACN) and H_2O in a volume ratio of 1:1). Angiotensin- II stock solution was prepared at a concentration of 4 pmol/μL in H_2O. The sample of Angiotensin II was prepared by mixing the matrix stock solution with the sample stock in a volume ratio of 1:3, resulting in a final sample concentration of 1 pmol/μL. 1.0 μL of the final sample solution was deposited on the sample plate and allow to air dry.

2.2.2 PSD Calibration

Mass calibration in PSD analysis is a topic of great importance. In classical time-of-flight analysis of stable ions, mass calibration is fairly easy. Regardless of the number and nature of static acceleration or deceleration fields within the instrument, the mass-time relationship always follows the equation:

$$t = a + bm^{1/2} \qquad (2.2.1)$$

Any time-of-flight spectrum of stable ions can therefore be calibrated by a two-point or least-squares fit calibration using at least two known ion signal masses from calibration substances.

In PSD analysis, the situation is much more complicated for two-stage reflectron, that's because the reflection voltage is changed when acquiring the spectrum of product ions in the PSD analysis, the traditional calibration method is not available any more.

The procedure of calibration is shown as below:

(1) Calibrate the instrument using normal calibration method.

(2) Obtain the spectrum for each reflection voltage stage, and there are 19 stages in

our calibration method.

(3) To match the spectra obtained from the instrument and the reference spectra from Bruker. (the MALDI-TOFMS is from Bruker)

(4) Revenant peaks were labeled and input in the calpklist provide by Bruker.

(5) Let the calibration program run and a report will be given, check the chi-square value in the report, and eliminate the deviated peak if chi-square value is large than 0.5

(6) Repeat step (4)-(5) until all the chi-square is smaller than 0.5.

(7) Save the calpklist, and paste the spectrum segments.

Chapter Three

Simulation Studies of Time Ion Selector, Collision Cells and Curved-field Reflectron

3.1 Introduction

This chapter aims to conduct systematic simulation studies on three of the critical components in a tandem time-of-flight mass spectrometer, including the time ion selector, the collision cell and the curved-field reflectron. A PC-based computer software, i.e. SIMION[99] (version 7.0) was used. SIMION is a general and time-tested platform for simulating lens, mass spectrometry, and other types of particle optics systems. It provides extensive supporting functionality in (a) defining the workbench and electrodes; (b) developing custom-made user program; and (c) recording, processing and visualization the ion trajectories. A user program is an ASCII file that contains one or more program segments (like sub-programs) written in an HP calculator based RPN language. As an ion flies within any instance tied to a potential array with active user program segments, SIMION automatically calls each program segment at the appropriate time to allow it to control how the ion flies. These program segments can dynamically change fast adjust electrodes; electrostatic and magnetic fields; ion accelerations; and all sorts of other things. A screendump of SIMION is shown in Figure 3.1.1.

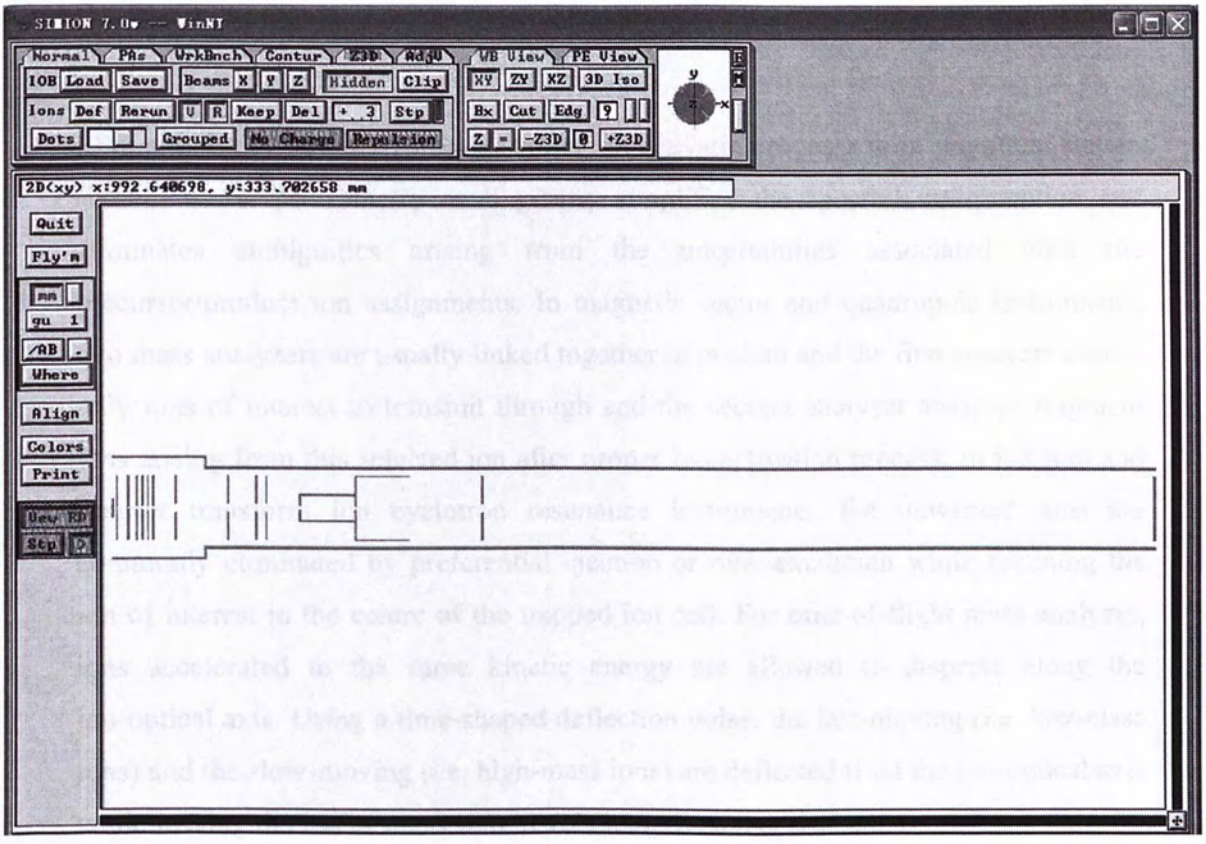

Figure 3.1.1 A screenshot of SIMION.

3.2 Time Ion Selector

Elimination of unwanted ion prior to the ion activation process is an important step in tandem mass spectrometry as it greatly simplifies the spectral interpretation and eliminates ambiguities arising from the uncertainties associated with the precursor/product ion assignments. In magnetic sector and quadrupole instruments, two mass analyzers are usually linked together in tandem and the first analyzer allows only ions of interest to transmit through and the second analyzer analyses fragment ions arising from this selected ion after proper ion activation process. In ion trap and Fourier transform ion cyclotron resonance instruments, the unwanted ions are commonly eliminated by preferential ejection or over-excitation while retaining the ion of interest in the centre of the trapped ion cell. For time-of-flight mass analyzer, ions accelerated to the same kinetic energy are allowed to disperse along the ion-optical axis. Using a time-shaped deflection pulse, the fast-moving (i.e. low-mass ions) and the slow-moving (i.e. high-mass ions) are deflected from the ion-optical axis while leaving the ion of interest to travel along the ion optical axis.

Common time ion selector includes a set of deflection plates[89,90,91,92,93,94] or a single set of interleaved wire-combs.[95,96,97] As is expected, the time resolution of a single deflector gate is severely limited by the sharpness of the leading and trailing edges of the voltage pulse that are used to actuate the gate's shuttering function. It has been postulated[98,99] and later confirmed experimentally that this restriction can be circumvented by sharing the opening and closing actions of the gate between two tandem ion deflectors. A version of this novel dual-stage time ion selector[100] is shown in Figure 3.2.1.

By means of computer simulation, this section aims to study the performance of dual-stage time ion selector in isolating an ion of interest and to obtain critical geometrical information of an optimize system. A parallel simulation study has also been conducted on the built-in ion selector of the Bruker Biflex system. The user program developed to control the on/off voltage pulse is shown in Appendix I. Figure 3.2.2. shows schematic diagrams of the single-stage (a) and dual-stage (b) time ion selectors. In both cases, a pair of parallel grounded electrodes is placed in the front

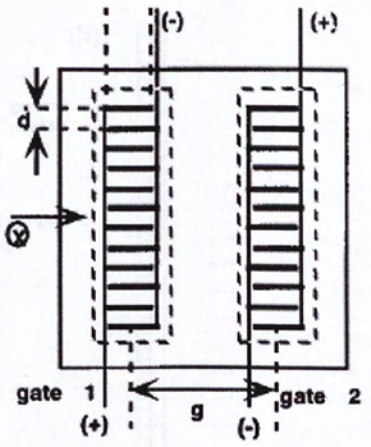

Figure 3.2.1 Schematic diagram of dual-stage ion selector. 'd' is the distance between strips, and 'g' is distance between the two deflectors. '+' and '-' mean the high voltage applied to the metal strip is positive or negative.

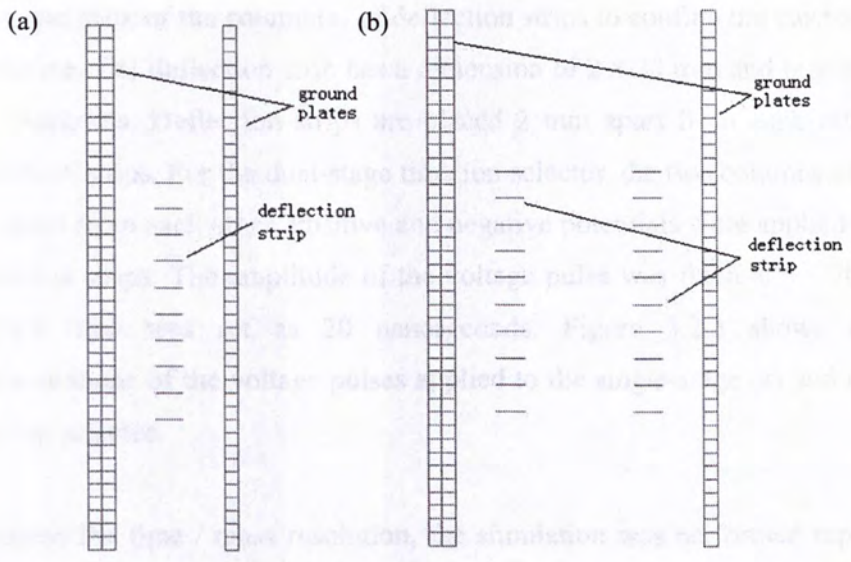

Figure 3.2.2 Schematic diagrams of geometries of the two types of time ion selectors. Single-stage ion selector (a), the width of deflection strip is 2 mm, length is 20 mm, and the distance between adjacent strips is 2 mm. Dual-stage ion selector (b), the width of the deflection strip is 2 mm, length is 20 mm, the distance between adjacent strips is 2 mm, and the distance between two sets of strips is 10 mm. The thickness of deflection strip in both single and dual ion selector is as thin as possible to maximize transmission of the ion beam.

and at the back of the column(s) of deflection strips to confine the electric field within the device. The deflection strip has a dimension of 2 x 20 mm and is assumed to have zero thickness. Deflection strips are placed 2 mm apart from each other to form a column of strips. For the dual-stage time ion selector, the two columns of strips are 10 mm apart from each other. Positive and negative potentials were applied in alternative deflection strips. The amplitude of the voltage pulse was fixed at +/- 700 V; and the rise/fall time was set as 20 nanoseconds. Figure 3.2.3 shows diagrammatic representations of the voltage pulses applied to the single-stage (a) and dual-stage (b) time ion selector.

To assess the time / mass resolution, the simulation was performed repeatedly using ion groups of slightly different *m/z* values. Three hypothetical mass ranges were evaluated, including *m/z* of 1347, 2845 and 5734. For each mass range, a total of 9 ion groups of different *m/z*'s was used. For instance, the ions used in isolating the ion *m/z* 1347, the 9 ion groups are *m/z* 1331, 1335, 1339, 1343, 1347, 1351, 1355, 1359 and 1363. In each ion group, a total of 30 ions were used and were positioned at different positions along axis perpendicular to the ion optical axis. All ions were assumed to fly in parallel and to have the same kinetic energy of 19 keV.

The efficient radius of the detector was defined, if the radial deviation of the ion is smaller than the efficient radius when the ion reaches the detector, the ion will be detected and the intensity of the ion will be summed.

The results of simulations are presented in Figure 3.2.4-3.2.7. The value of FWHH (full width half height) is used to evaluate the performance of ion selection for these two types of time ion selectors. The larger the value of FWHH is, the better ion selection is. From the results, the ion selection in dual-stage time ion selector is much better than that of the single-stage ion selector when isolating both low-mass and high-mass ions.

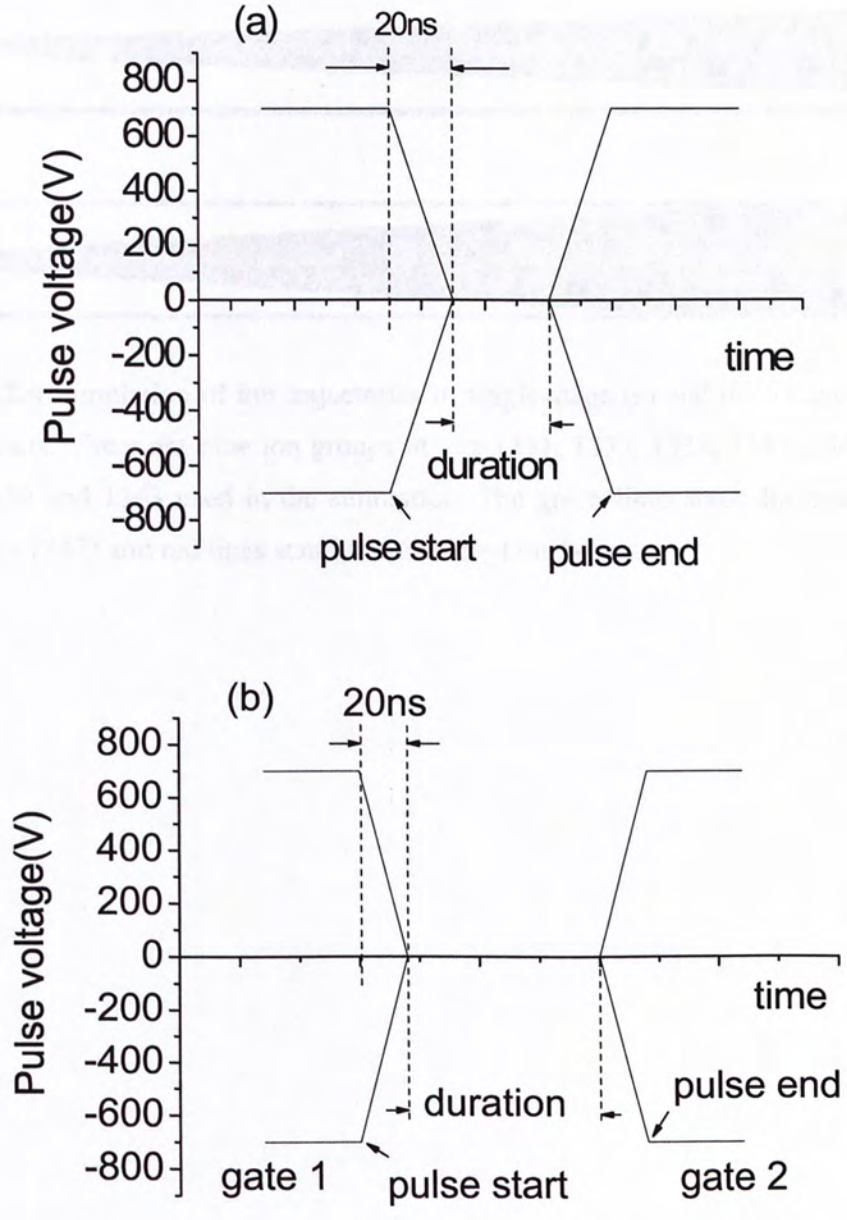

Figure 3.2.3 Pulse applied to the time ion selector, single-stage ion selector (a), dual-stage ion selector (b). For these two ion selectors, the pulse rise time is 20 ns. In the simulation, the pulse start and end time can be adjusted to change the duration time in order to achieve the best performance of ion selection.

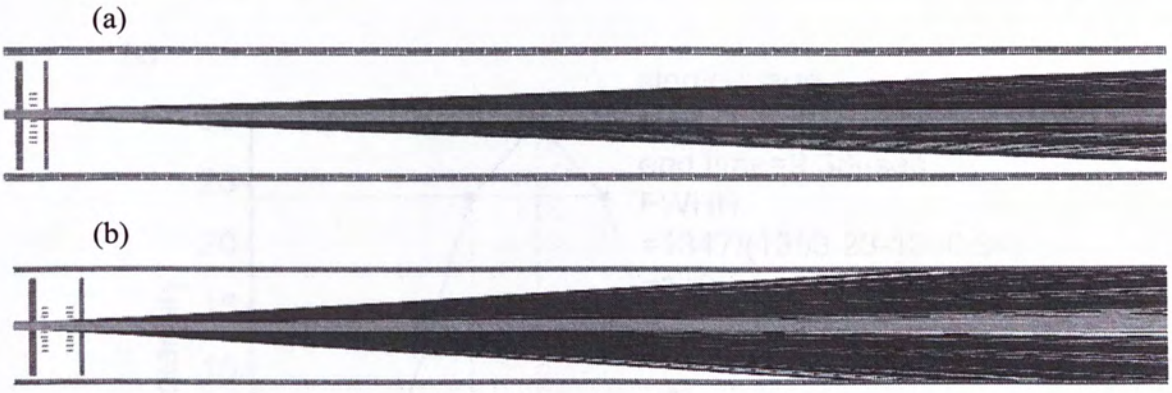

Figure 3.2.4 Simulation of ion trajectories in single-stage (a) and dual-stage (b) time ion selectors. There are nine ion groups of *m/z* 1331, 1335, 1339, 1343, 1347, 1351, 1355, 1359 and 1363 used in the simulation. The green lines stand for selected ion beam (*m/z* 1347) and red lines stand for unwanted ion beams.

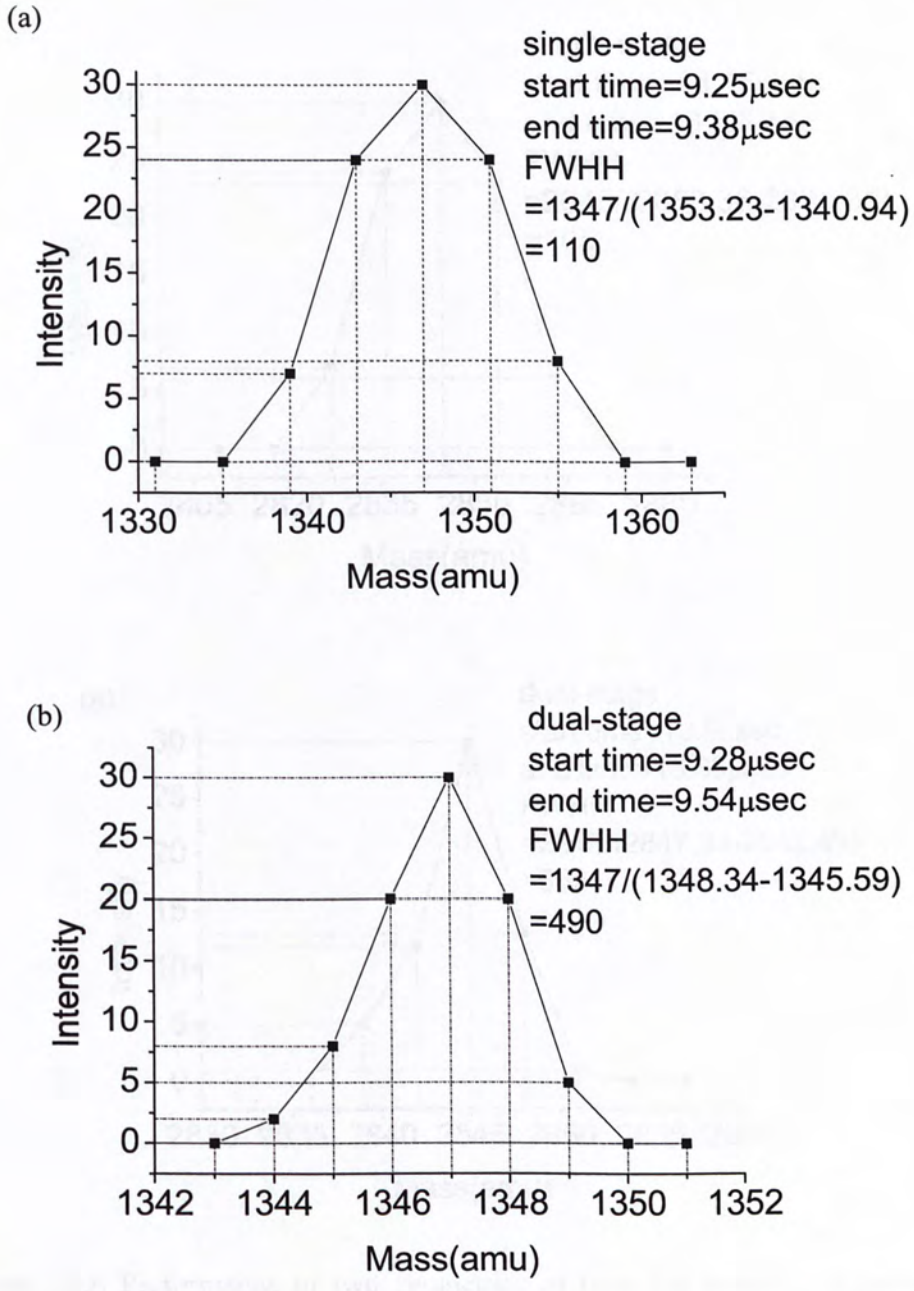

Figure 3.2.5 Performance of two geometries of time ion selector, single-stage (a), dual-stage (b). Use a hypothetical ion of *m/z* of 1347 as the target ion for selection. Start and end time stand for the pulse start and end time. FWHH stands for full-width half-height.

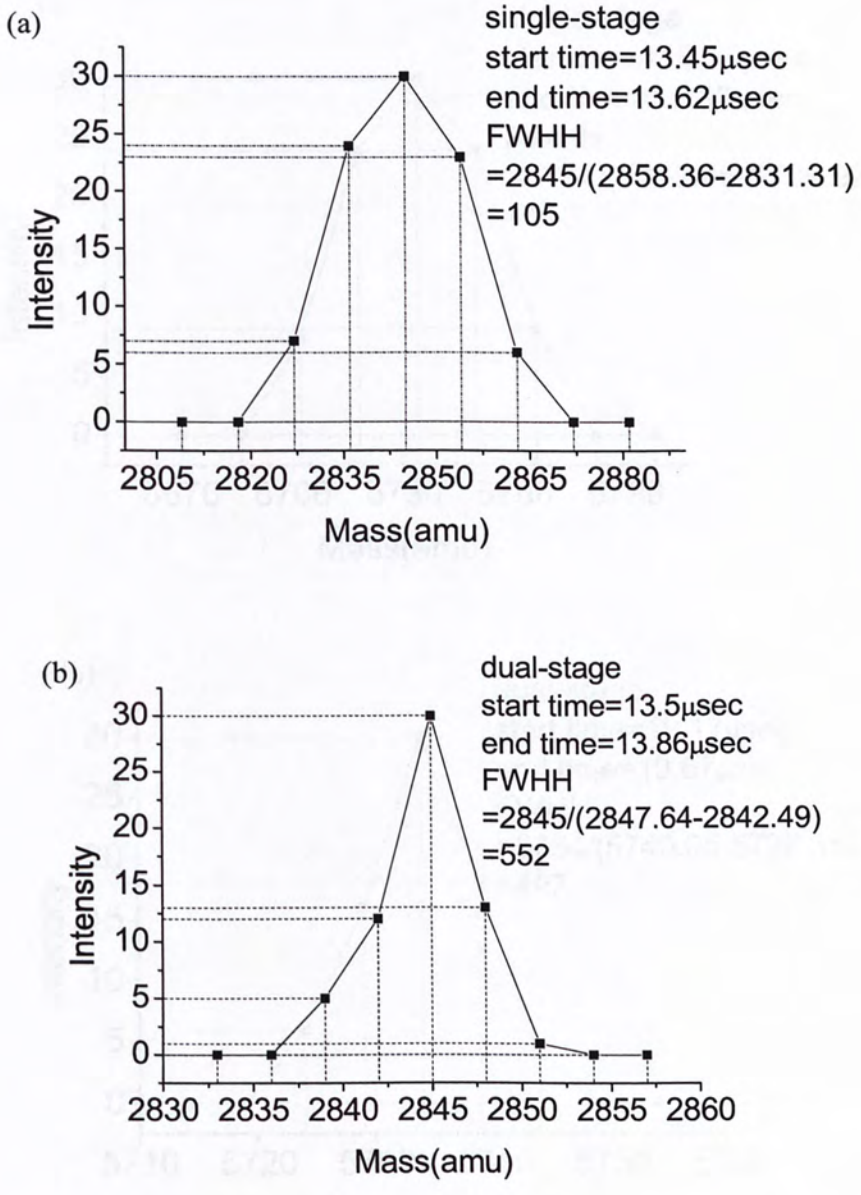

Figure 3.2.6 Performance of two geometries of time ion selector, single-stage (a), dual-stage (b). Use a hypothetical ion of *m/z* of 2845 as the target ion for selection. Start and end time stand for the pulse start and end time. FWHH stands for full-width half-height.

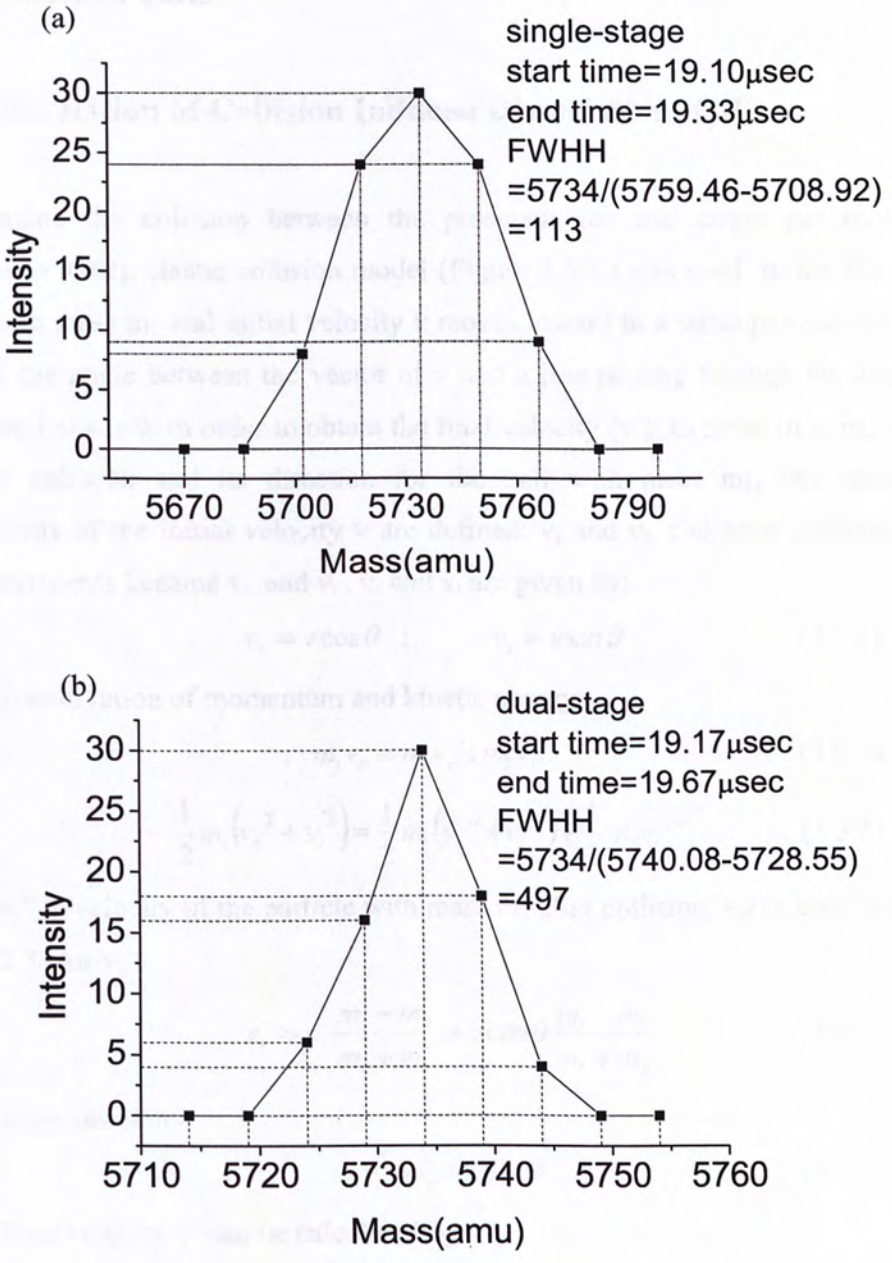

Figure 3.2.7 Performance of two geometries of time ion selector, single-stage (a), dual-stage (b). Use a hypothetical ion of *m/z* of 5734 as the target ion for selection. Start and end time stand for the pulse start and end time. FWHH stands for full-width half-height.

3.3 Collision cells

3.3.1 Simulation of Collision Induced Dissociation (CID)

To simulate the collision between the precursor ion and target gas molecules, hard-sphere (HS), elastic collision model (Figure 3.3.1.) was used. In the HS model, a ball with mass m_1 and initial velocity v moves toward to a static particle with mass m_2, and the angle between the vector of v and a line passing through the centers of these two balls is θ. In order to obtain the final velocity (v'), in terms of v, m_1, m_2 and θ, after collision and its direction for the ball with mass m_1, two orthogonal components of the initial velocity v are defined: v_r and v_t, and after collision, these two components became v_r' and v_t'. v_r and v_t are given by:

$$v_r = v\cos\theta \;; \qquad v_t = v\sin\theta \tag{3.3.1}$$

By the conservation of momentum and kinetic energy:

$$m_1 v_r = m_1 v_r' + m_2 v_r'' \tag{3.3.2}$$

$$\frac{1}{2}m_1\left(v_r^{\,2} + v_t^{\,2}\right) = \frac{1}{2}m_1\left(v_r'^2 + v_t'^2\right) + \frac{1}{2}m_2 v_r''^2 \tag{3.3.3}$$

where v_r'' is velocity of the particle with mass m_2 after collision, solve equation (3.3.2) and (3.3.3) for v_r':

$$v_r' = v_r\frac{m_1 - m_2}{m_1 + m_2} = v\cos\theta\frac{m_1 - m_2}{m_1 + m_2} \tag{3.3.4}$$

and v_t' stays the same:

$$v_t' = v_t = v\sin\theta \tag{3.3.5}$$

So the final velocity v' can be calculated by:

$$v' = \sqrt{v_r'^2 + v_t'^2} = v\sqrt{\left(\cos\theta\frac{m_1 - m_2}{m_1 + m_2}\right)^2 + (\sin\theta)^2} \tag{3.3.6}$$

The angle (θ') between the direction of v' and a line passing through the centers of these two particles is determined by:

$$\theta' = \arctan\frac{v_t'}{v_r'} = \arctan\left(\frac{m_1 - m_2}{m_1 + m_2}\tan\theta\right) \tag{3.3.7}$$

and (θ'-θ) is the deflection angle of the particle of mass m_1.

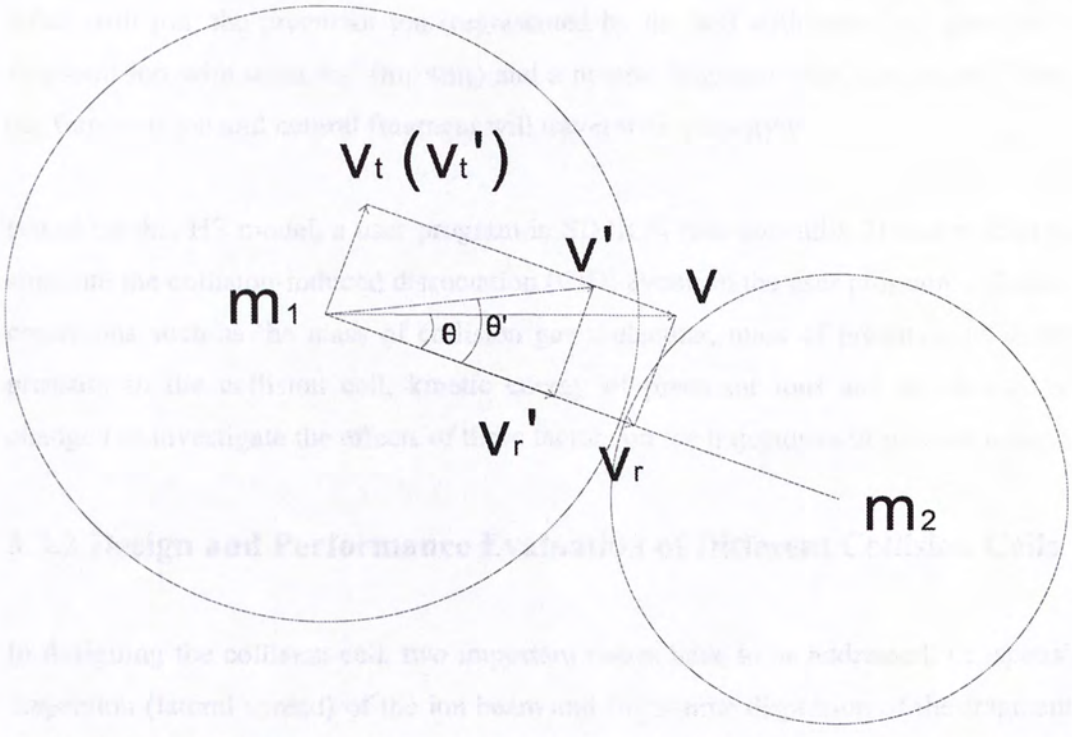

Figure 3.3.1 Hard-sphere (HS) model for simulation of CID. m_1 and m_2 are mass of the two particles for collision. v and v' are initial velocity and velocity after collision of the particle with mass m_1, respectively. v_r and v_t are two orthogonal components of the initial velocity v and after collision, these two components became v_r' and v_t'. The angle between the vector of v and a line passing through the centers of these two particles is θ, and after collision the angle becomes θ'.

After collision, the precursor ion (represented by the ball with mass m_1) generate a fragment ion with mass m_1' (m_1'<m_1) and a neutral fragment with mass m_1-m_1', and the fragment ion and neutral fragment will travel with velocity v'.

Based on this HS model, a user program in SIMION (see appendix 2) was written to simulate the collision-induced dissociation (CID) event. In the user program, collision conditions such as the mass of collision gas molecular, mass of precursor ions, the pressure in the collision cell, kinetic energy of precursor ions and so on can be changed to investigate the effects of these factors on the trajectories of product ions.

3.3.2 Design and Performance Evaluation of Different Collision Cells

In designing the collision cell, two important issues have to be addressed, i.e. spatial dispersion (lateral spread) of the ion beam and flight-time dispersion of the fragment ions. To facilitate the optimization of the performance of the collision cell, a throughout ion trajectory simulation study was conducted using SIMION. Different geometries of collision cell were investigated (Figure 3.3.2.). These included (a) segmented cylindrical collision cell, (b) cylindrical collision cell with a focus lens[113], and (c) field-shaped cylindrical collision cell. To investigate the performance of these collision cell designs, the spatial and flight-time dispersions of the fragment ions (in terms of the percentage of precursor ion mass) were monitored. A hypothetical ion at m/z of 5734 was used as precursor ion, and the mass ratio of product ions to parent ions was systematically varied from 0.1 to 0.9 in steps of 0.1.

In the simulation, the spatial spread was defined as the radial distance from the center of detector when the ions reached the detector, and the flight-time deviation referred to standard deviation of the flight-time for ions when they arrived at the detector. The results of spatial and flight-time dispersions for the fragment ions are shown in Figure 3.3.3 - 3.3.8.

Figure 3.3.3 and 3.3.4 show the spatial and time dispersions of fragment ions in the segmented cylindrical collision cell. The segment potentials were 5, 4, 3, 2, 1 kV. From the figures, when the ion has low mass, the time dispersion is large. The largest

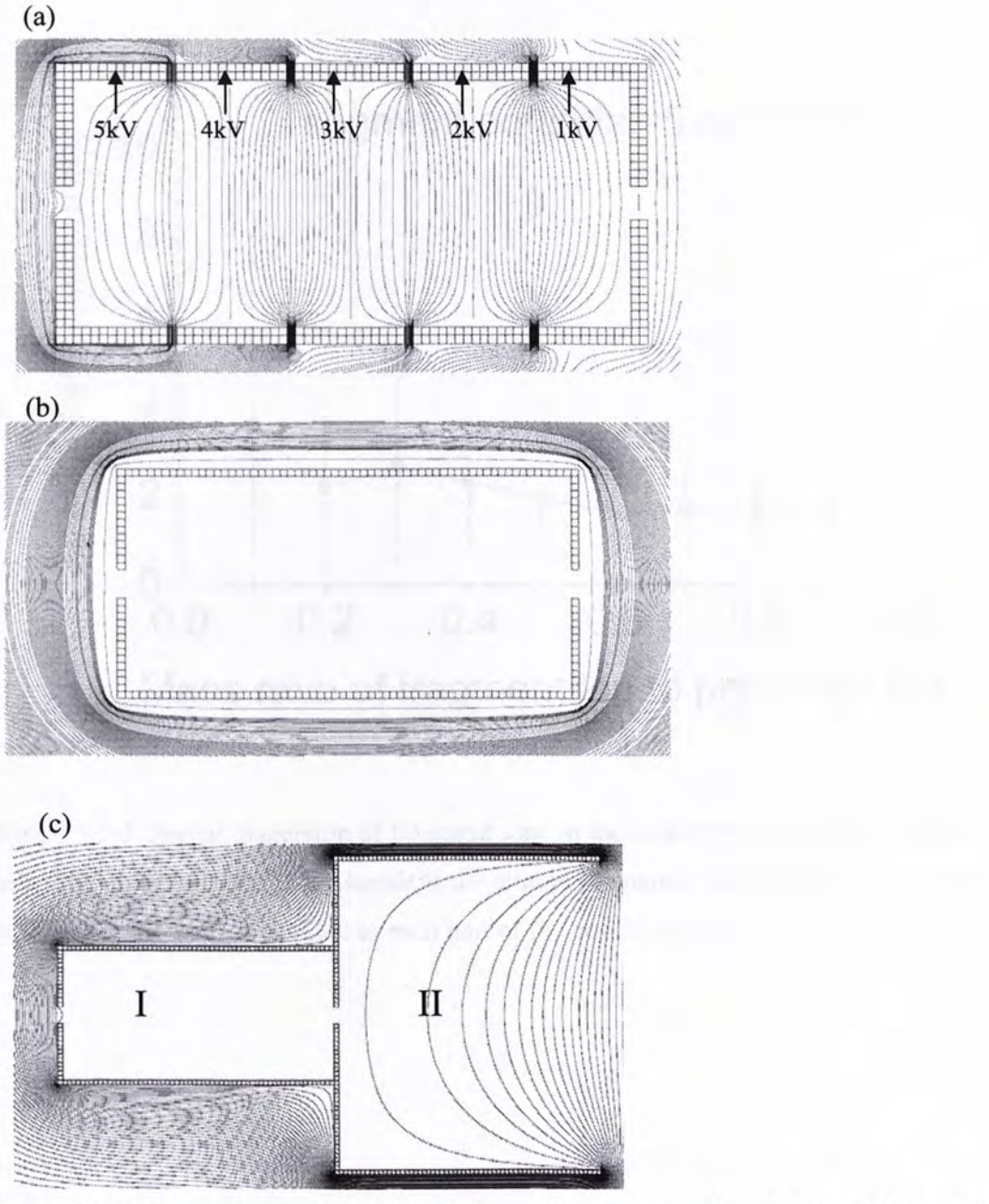

Figure 3.3.2 Three geometries of collision cells were used in the simulation and equipotential lines of floated collision cells are indicated. (a) Segmented cylindrical collision cell. 5, 4, 3, 2, 1 kV are segment potentials applied to each part of the collision cell. (b) Cylindrical collision cell with 6 kV floating voltage applied. (c) Field-shaped cylindrical collision cell. In the region II of field-shaped cylindrical collision cell, which is lifted to 8 kV, bending equipotential lines generate a focusing region for the ions and region I is the collision region.

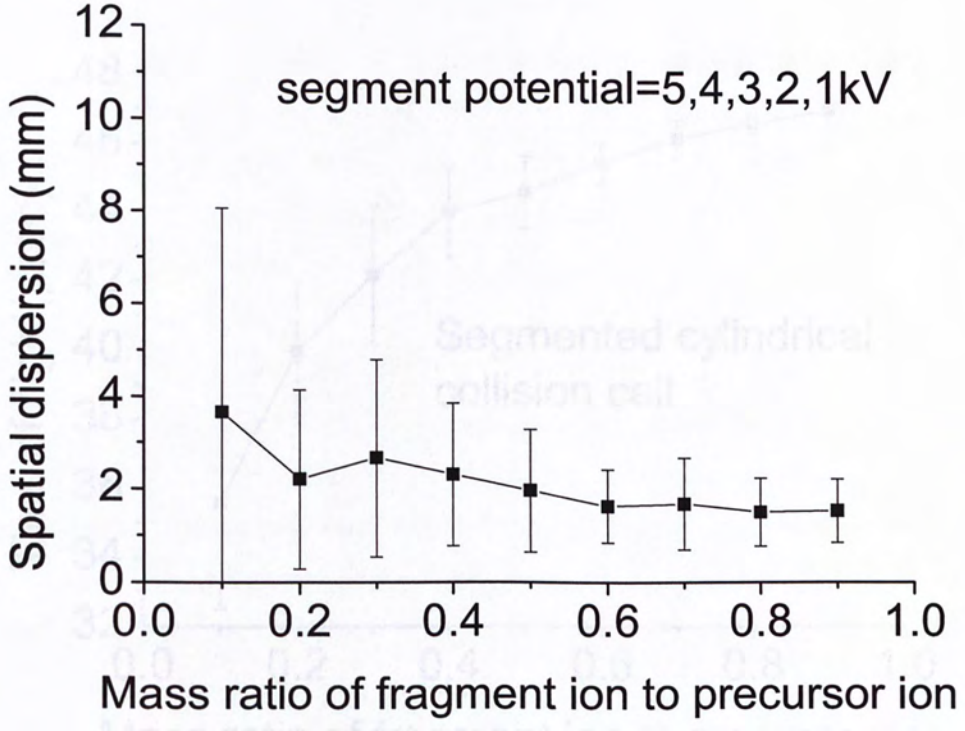

Figure 3.3.3 Spatial dispersion of fragment ions in the segmented cylindrical collision cell. The error bars stand for standard deviations of spatial dispersions. The segment potential is the voltage applied to each part of the collision cell.

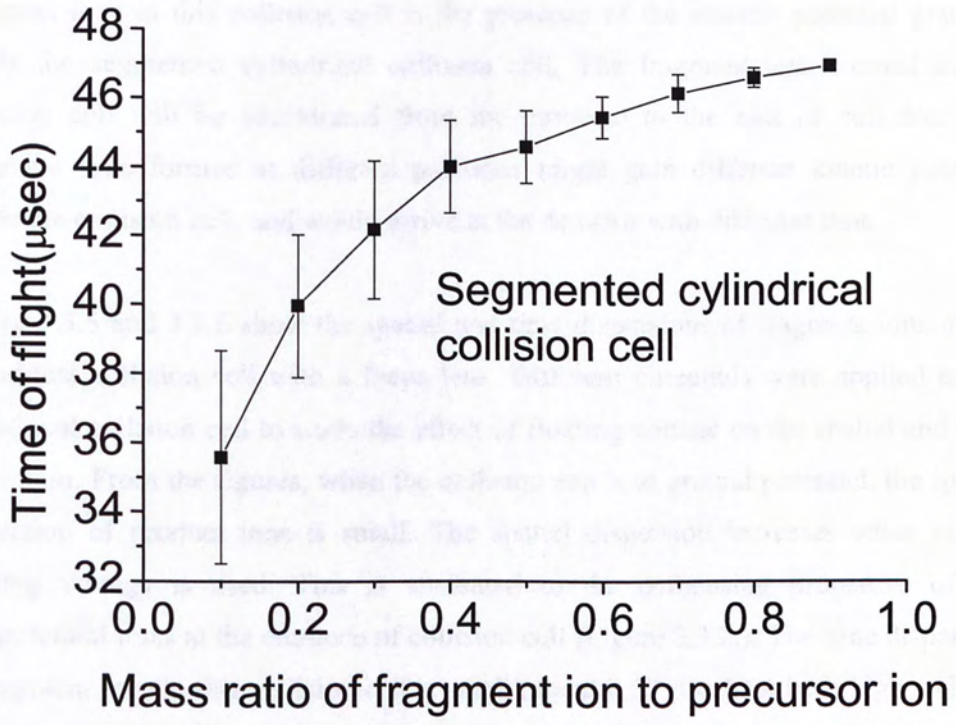

Figure 3.3.4 Time dispersion of fragment ions in the segmented cylindrical collision cell. Error bars standard for the flight time deviations.

time dispersion is about 2.5 μsec. The spatial dispersion of fragment ions is small for both high and low mass ions. A possible explanation on the large time dispersion of fragment ions in this collision cell is the presence of the electric potential gradient inside the segmented cylindrical collision cell. The fragment ions formed in the collision cell will be accelerated from the entrance to the exit of collision cell. Fragment ions formed at different positions might gain different kinetic energies inside the collision cell, and would arrive at the detector with different time.

Figure 3.3.5 and 3.3.6 show the spatial and time dispersions of fragment ions in the cylindrical collision cell with a focus lens. Different potentials were applied to the cylindrical collision cell to study the effect of floating voltage on the spatial and time dispersion. From the figures, when the collision cell is at ground potential, the spatial dispersion of product ions is small. The spatial dispersion increases when higher floating voltage is used. This is attributed to the defocusing properties of the equipotential lines at the entrance of collision cell (Figure 3.3.2.). The time dispersion of fragment ions in this collision cell is small (about 0.02 μsec) for both high and low mass fragment ions and is independence of the potential of the collision cell.

Figure 3.3.7 and 3.3.8 show the spatial and time deviations of fragment ions in the field-shaped cylindrical collision cell. The floating voltage on the collision cell was set at different values to investigate the effect of floating voltage on the spatial and time dispersion. From the figures, the spatial and time dispersion are both small compared with the other two types of collision cell.

Floating the collision cell at high potential has two effects, inducing a reduction of the collision energy between precursor ions and collision gas; and a reduction of the energy range of product ions. Product ions with a narrower energy range can be then focused better by the reflectron. In summary, floating the collision cell at high potential has different effect on different collision cell designs. For segmented cylindrical collision cell, fragment ions will be collected with large time dispersion; whereas for cylindrical collision cell, fragment ions will be collected with large spatial dispersion. Field-shaped cylindrical collision cell has the best performance in terms of minimizing both spatial and time dispersion. The smallest spatial dispersions in the cylindrical collision cell and field-shaped collision cell are presented in Figure 3.3.9.

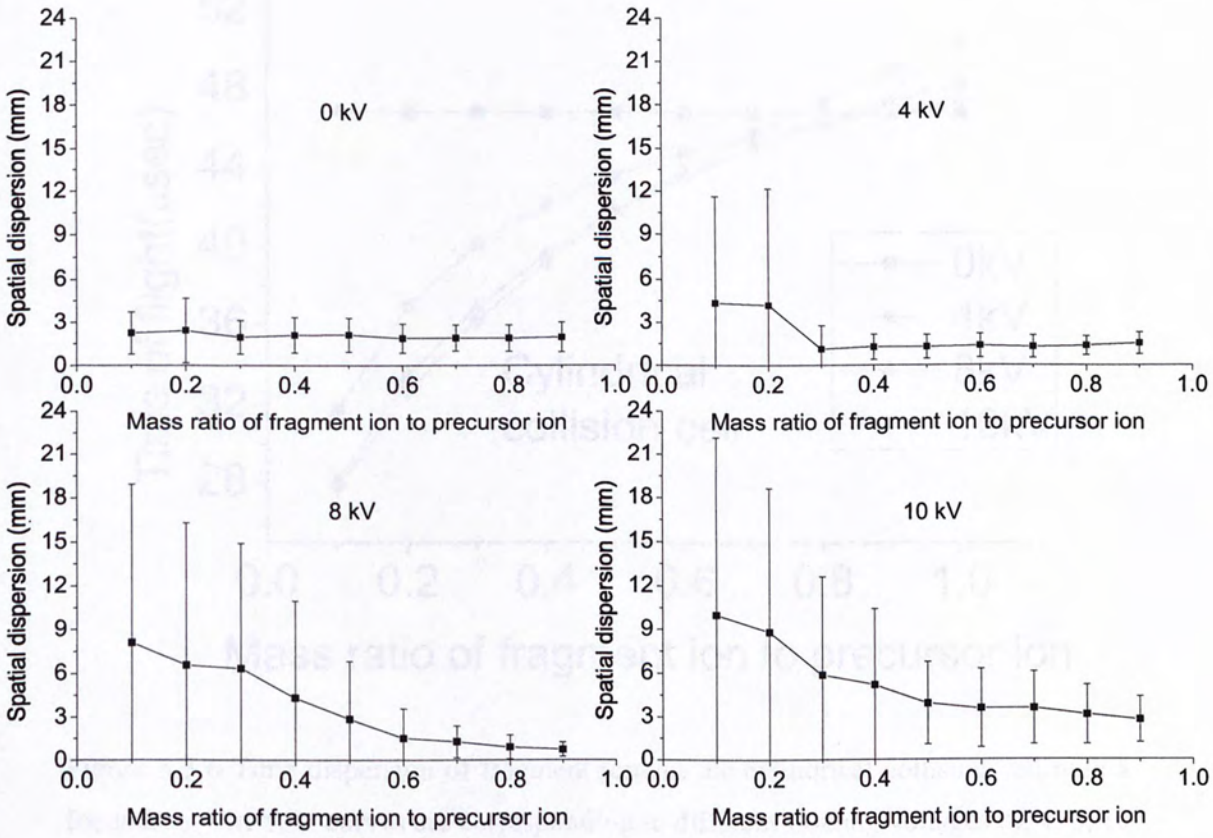

Figure 3.3.5 Spatial dispersions of fragment ions in the cylindrical collision cell with a focus lens. The collision cell was applied with different floating voltage (0, 4, 8, 10 kV). The error bars refer to standard deviations of spatial dispersions.

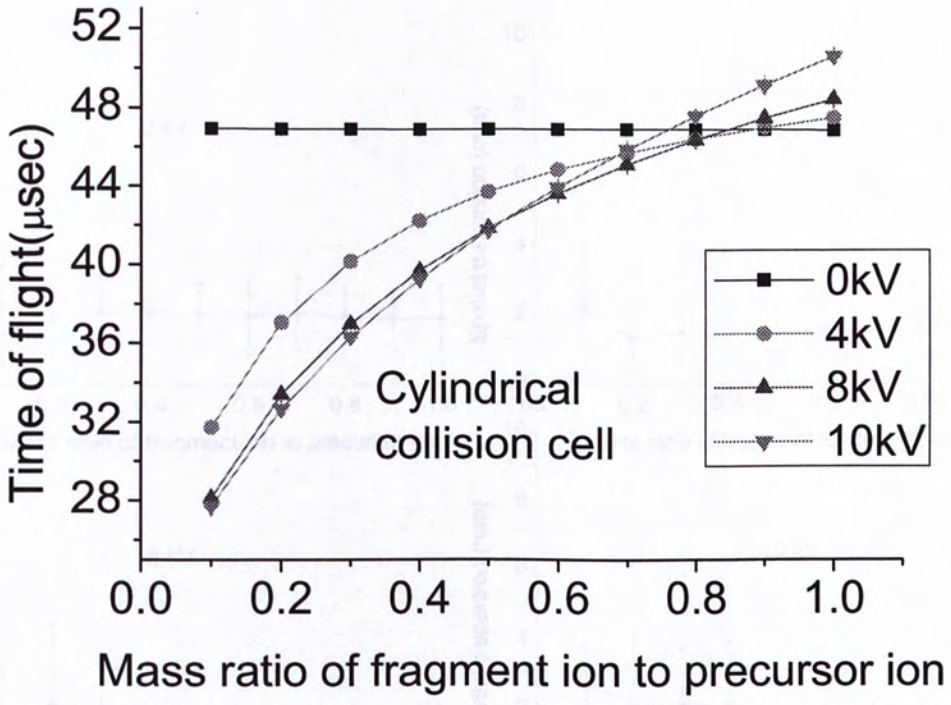

Figure 3.3.6 Time dispersion of fragment ions in the cylindrical collision cell with a focus lens. The four curves are corresponding to different floating voltages (0, 4, 8, 10 kV). Error bars standard for flight time deviations.

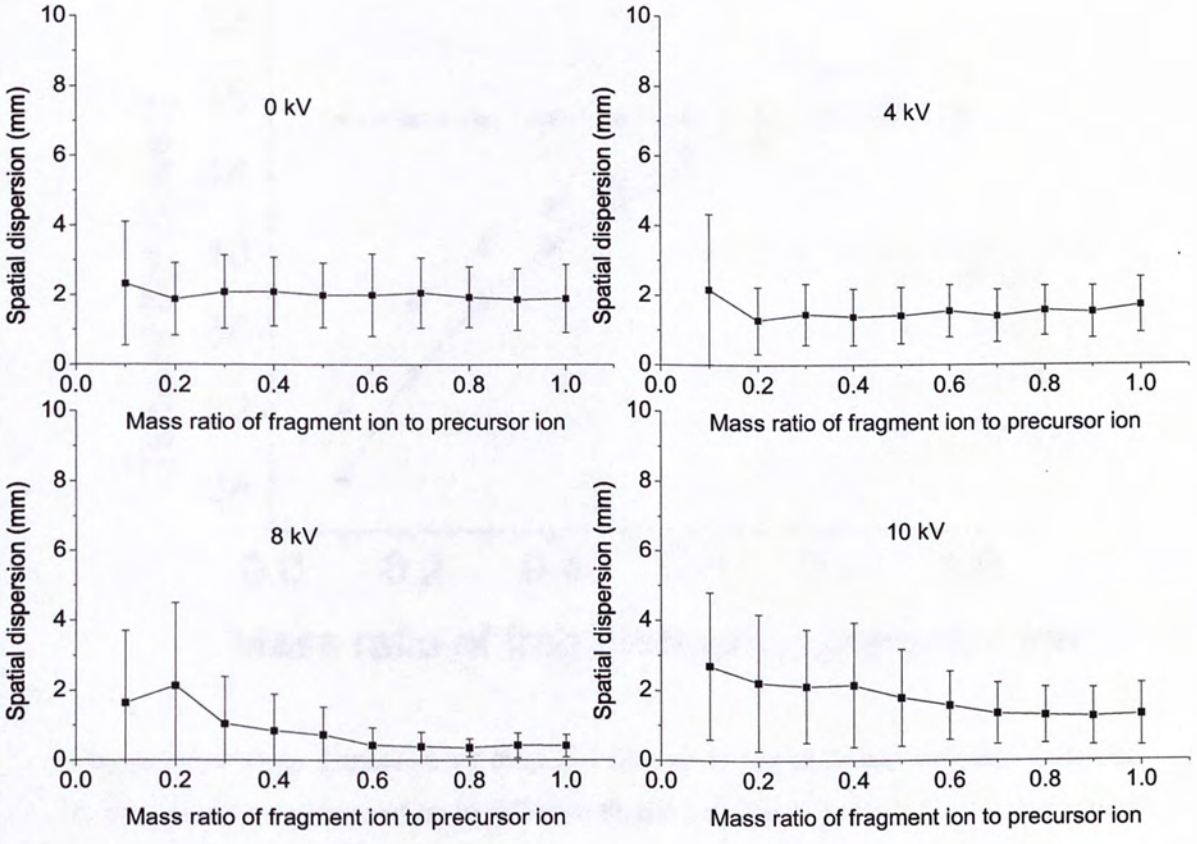

Figure 3.3.7 Spatial dispersion of fragment ions in the field-shaped collision cell. The collision cell was applied with different floating voltage (0, 4, 8, 10 kV). The error bars refer to standard deviations of spatial dispersions.

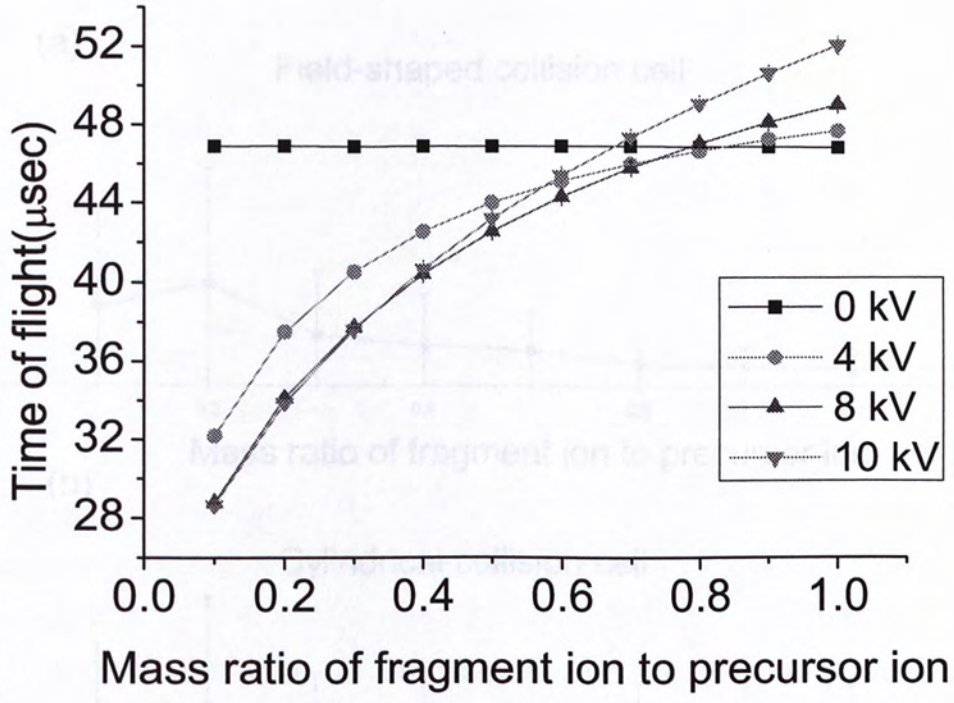

Figure 3.3.8 Time dispersion of fragment ions in the field-shaped collision cell. The four curves are corresponding to different floating voltages (0, 4, 8, 10 kV). Error bars standard for flight time deviations.

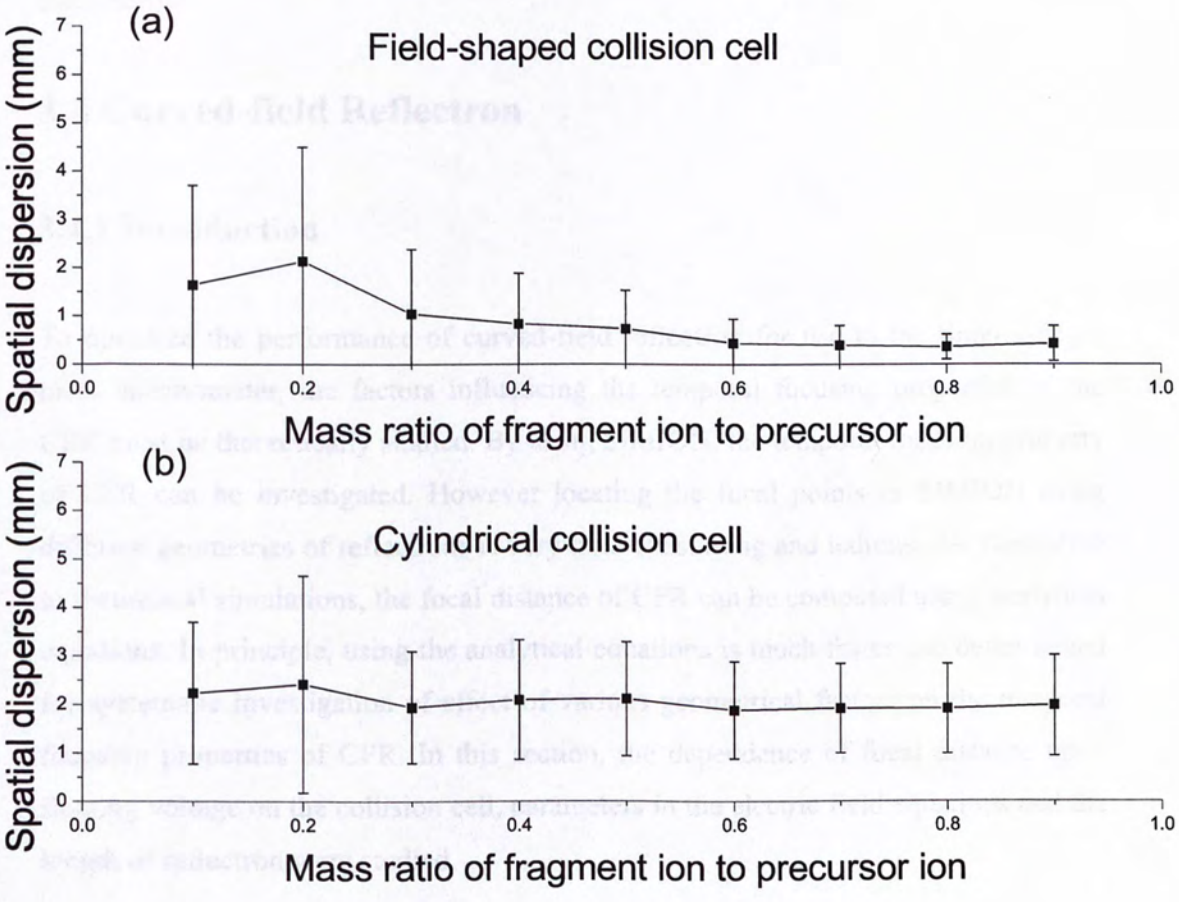

Figure 3.3.9 The smallest spatial dispersions in (a) field-shaped collision cell and (b) cylindrical collision cell with a focus lens. The field-shaped collision cell is applied with 8 kV floated potential and the cylindrical collision cell is ground.

Therefore, the field-shaped cylindrical collision cell will be used for the modified instrument.

3.4 Curved-field Reflectron

3.4.1 Introduction

To optimize the performance of curved-field reflectron for use in the time-of-flight mass spectrometer, the factors influencing the temporal focusing properties of the CFR must be theoretically studied. By using SIMION, the temporal focusing property of CFR can be investigated. However locating the focal points in SIMION using different geometries of reflectrons is very time consuming and tedious. An alternative to theoretical simulations, the focal distance of CFR can be computed using analytical equations. In principle, using the analytical equations is much faster and better suited for systematic investigation of effect of various geometrical factors on the temporal focusing properties of CFR. In this section, the dependence of focal distance upon floating voltage on the collision cell, parameters in the electric field equations and the length of reflectron were studied.

3.4.2 Derivation of Analytical Equations

To locate temporal focal point of the ion, flight time of the ion from the ion source to the detector in the time-of-flight mass spectrometry should be calculated. The overall flight time of an ion is divided into two parts: flight time for passing through the field-free region (t_1) and inside the reflectron (t_2). The flight time in the field-free region is easily calculated using equation 3.4.1.

$$t_1 = \left(\frac{m}{2E}\right)^{1/2} L \qquad (3.4.1)$$

where L is the length of drift region (include the regions before and after the reflectron) , E is kinetic energy of the ion, m is mass of the ion.

The flight time inside the curved-field reflectron depends on the electric field inside the CFR. Since the function of electric field applied to the lens elements of

curved-field reflectron follows the arc of a circle (Figure 3.4.1.), the potential (Vr) along the axis of the reflectron is simply a function of the distance (D) from the entrance:

$$V_r = V_1 - \sqrt{R^2 - \left(\frac{x_2 - x_1}{d} D + x_1\right)^2} \qquad (3.4.2)$$

where d is the length of reflectron, V_1 is given by:

$$V_1 = R\cos\theta \qquad (3.4.3)$$

and

$$x_1 = \sqrt{R^2 - V_1^2} \qquad (3.4.4)$$

$$x_2 = \sqrt{R^2 - V_2^2} \qquad (3.4.5)$$

$$V_2 = V_1 - V_R \qquad (3.4.6)$$

where V_1 , V_2 , R , θ , x_1 and x_2 are variables defined in Figure 3.4.1, V_R is the reflection voltage at the back of reflectron. The flight time of the ion inside the reflectron is therefore given by:

$$t_2 = 2\times \int_0^{D_r} \frac{dD}{\cos\alpha\sqrt{\frac{2(E - V_r)}{m}}} \qquad (3.4.7)$$

where α is the angle between ion velocity and the axis of reflectron, D_r is the distance from the entrance to the reflection point, and is given by :

$$D_r = (\sqrt{R^2 - (V_1 - E\cos\alpha\cos\alpha)^2} - x_1)\frac{d}{x_2 - x_1} \qquad (3.4.8)$$

The total flight time t is:

$$t = t_1 + t_2 \qquad (3.4.9)$$

The temporal focal point for a group of ions is the position in the drift region where the calculated value of $t_{mean}/\Delta t$ is maximized, where t_{mean} is the mean value of flight time, Δt is standard deviation of flight time. To locate the temporal focusing point, $t_{mean}/\Delta t$ is calculated as a function of the distance (L) from the exit of the CFR.

$$t_{mean}/\Delta t = f(L) \qquad (3.4.10)$$

All the calculations were performed using a user program designed using MATHEMATICA (the program used for calculation is shown in the appendix 3). The

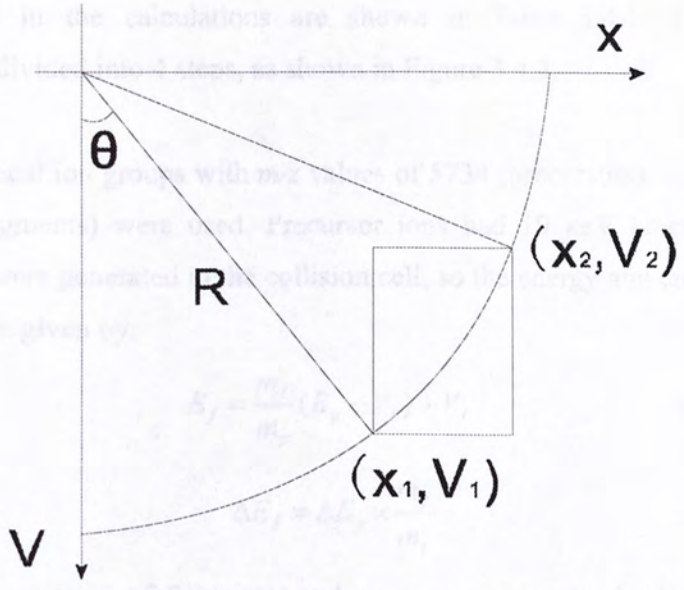

Figure 3.4.1 Plot of the potential versus depth into the curved-field reflectron. The function of the electric field follows the arc inside the square. R is the radius of the circle, θ is an angle related to the arc, V is the voltage on the lens element, x is depth from entrance of the reflectron, x_1 and x_2 are x coordinates for the entrance and exit of reflectron respectively, V_1 and V_2 are two variables related to voltages on the first and last lens elements of the reflectron respectively.

variables used in the calculations are shown in Table 3.4.1. The process of calculations is divided into 4 steps, as shown in Figure 3.4.2.

Three hypothetical ion groups with *m/z* values of 5734 (precursors), 2867 (fragments) and 573.4 (fragments) were used. Precursor ions had 19 keV kinetic energy, and fragment ions were generated in the collision cell, so the energy and energy difference of fragments are given by:

$$E_f = \frac{m_f}{m_p}(E_p - V_f) + V_f \qquad (3.4.11)$$

$$\Delta E_f = \Delta E_p \times \frac{m_f}{m_p} \qquad (3.4.12)$$

where m_f , m_p are mass of fragments and precursors respectively, E_f, E_p are kinetic energy of fragments and precursors respectively, ΔE_f, ΔE_p are energy difference of fragments and precursors, respectively; and V_f is floating voltage on the collision cell. The mean value of initial desorption velocity of precursor ions was 1000 m/s[54], and the range of initial kinetic energy for precursor ion is varied from 0 to 120 eV in steps of 12 eV. The final kinetic energy range of precursor ions varied from 19000 eV to 19120 eV. The kinetic energy of fragment ions can be acquired using equations 3.4.11 and 3.4.12.

Locating focal points of ions by using analytical equation is fast and precise. To validate analytical method, same calculations were repeated using SIMION simulation. The results are shown in Table 3.4.2. The values of variables used in the calculations are: R is 300 kV, θ is 9.0°, length of reflectron is 290 mm, floating voltage is 8 kV, reflection voltage is 20 kV and α is 1.0°. From Table 3.4.2, the results of calculations by analytical equations and SIMION are almost the same, which proves that the results obtained by analytical equations are precise and creditable. The time spent in these two methods was quite different. It took 1-2 minutes in a calculation by the analytical equations method, while much more time was needed in SIMION simulation. Changing the geometry file, calculating the voltage on each lens element and locating the focal points in SIMION is very time-consuming.

In the following sections, the dependence of focal distance on variables such as

Table 3.4.1 Adjustable variables in the calculation.

Parameter	Description
R	Radius of a circle
θ	Degree of the angle
d	Length of reflectron
m_1	Mass of precursor
m_2	Mass of fragments
m_3	Mass of fragments
E_1	Kinetic energy of precursor
ΔE_1	Energy difference of m_1
α	Angle between ion velocity and axis of the reflectron
V_f	Floating voltage on the collision cell
V_R	Voltage at the back of reflectron

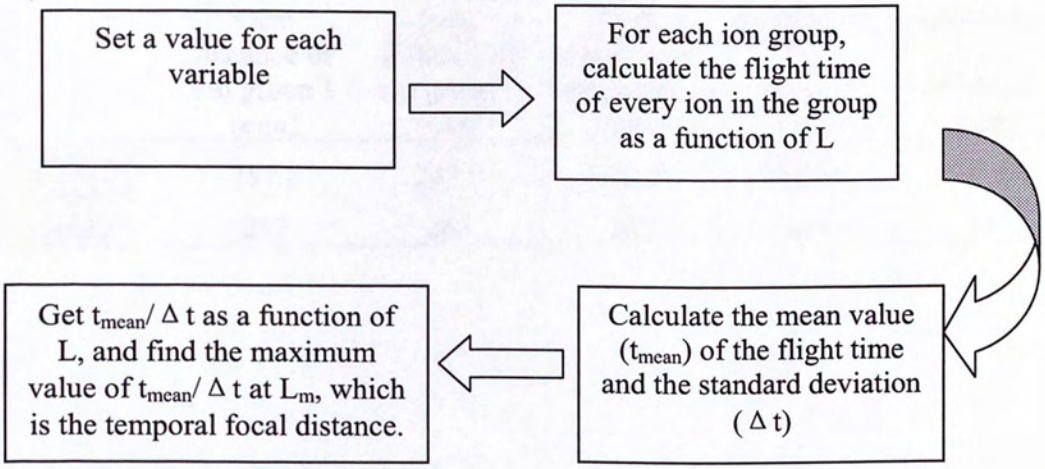

Figure 3.4.2 Flowchart of the calculations using MATHEMATICA.

Table 3.4.2 Results of analytical equation method and SIMION.

	Temporal focal distance of ion group 1 (mm)	Temporal focal distance of ion group 2 (mm)	Temporal focal distance of ion group 3 (mm)	Mean value of temporal focal distance (mm)	Standard deviation of focal distance (mm)
Analytical Equation	257.2	263.7	252.5	257.8	5.6
SIMION	257	263	253	258	5

floating voltage (V_f) on the collision cell, parameters R and θ in the electric field equations and the length of reflectron (d) will be discussed. The focusing power of curved-field reflectron was defined as $L_{mean}/\Delta L$, where L_{mean} is the mean value of focal distances for precursor ions and fragment ions, ΔL is its standard deviation.

3.4.3 Effect of Floating Potential (V_f) of the Collision Cell

Floating voltage applied to the collision cell can change the kinetic energy range of product ions generated in the collision cell. Ground collision cell results in the broadest kinetic energy range for product ions. Lifting collision cell potential can narrow kinetic energy range of fragment ions from Equations 3.4.11 and 3.4.12. Figure 3.4.3 shows focal distances of the precursor ions and fragment ions when different floating voltages were used. The parameters used in the electric field equations were: R = 300 kV, θ = 9.0°, α = 1.0°, length of reflectron is 290 mm and the reflection voltage is 20 kV. From figure 3.4.3, the focal distance of precursor ions (*m/z* = 5734) does not change against different floating voltages, and for high mass fragment ions (*m/z* = 2867) as well as low mass fragment ions (*m/z* = 573.4), there is a cross point with the curve for precursor ions. The crossing point implies that fragment ions and precursor ions have the same focal distance. At this point, the fragment ions and precursor ions can be focused simultaneously by the curved-field reflectron. However, the crossing points are different for fragment ions with different masses.

3.4.4 Effect of Parameters R and θ

R and θ are two major parameters that determine the electric field inside the curved-field reflectron, and can influence the focal distance. Figures 3.4.4-3.4.6 shows the effect of R and θ on focal distance. Precursor ions and fragment ions are plotted against the value of θ, and R was 300 kV, 600 kV and 900 kV, floating voltage was 8 kV, reflection voltage was 20 kV, the length of reflectron was 290 mm. The focal distances of the precursor ions and fragment ions increase as θ arises, while the slopes of the three curves are different, so the curves corresponding to precursor ions (*m/z* = 5734) and fragment ions (*m/z* = 573.4) have a crossing point, at which the deviation of the focal distances is minimized, and at this point $L_{mean}/\Delta L$ has a

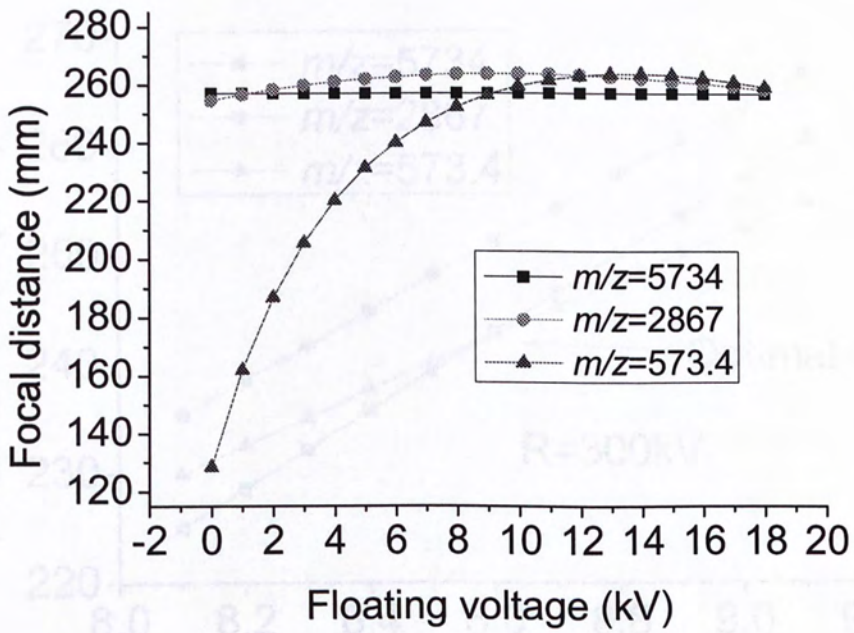

Figure 3.4.3 Focal distances of the precursor ions (*m/z* 5734), high mass fragment ions (*m/z* 2867) and low mass fragment ions (*m/z* 573.4) when different floating voltages were used.

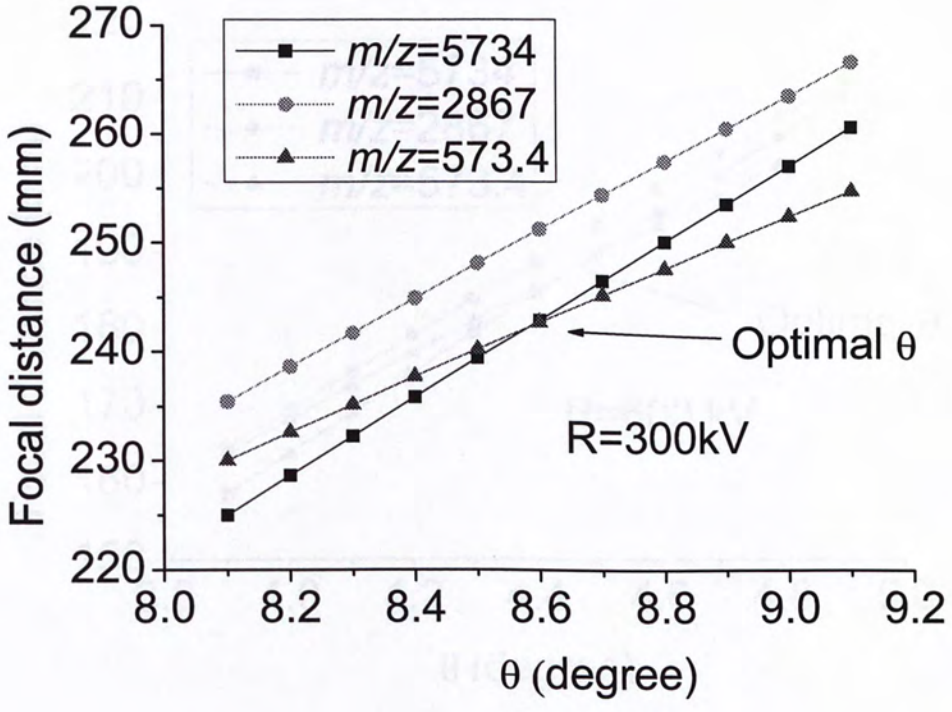

Figure 3.4.4 The relationship of focal distances of precursor ions (*m/z* 5734) and fragment ions (*m/z* 2867 and *m/z* 573.4) versus θ when R is 300 kV. R and θ are two variables in the electric field equation of curved-field reflectron. The optimal θ is at which the standard deviation of focal distances for precursor ions and fragment ions is minimum.

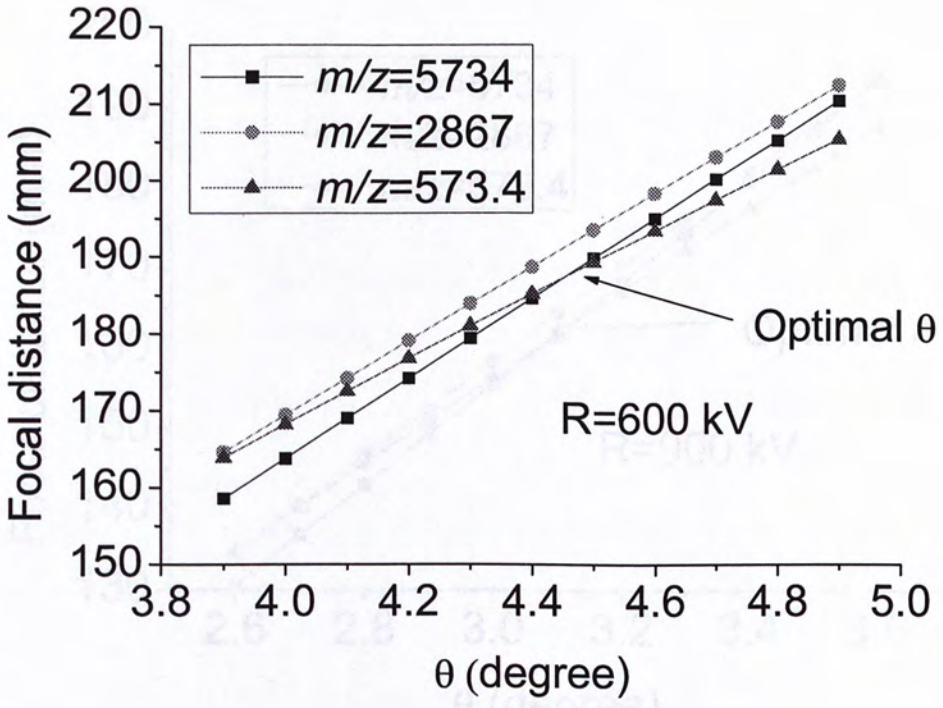

Figure 3.4.5 The relationship of focal distances of precursor ions (*m/z* 5734) and fragment ions (*m/z* 2867 and *m/z* 573.4) versus θ when R is 600 kV. R and θ are two variables in the electric field equation of curved-field reflectron. The optimal θ is at which the standard deviation of focal distances for precursor ions and fragment ions is minimum.

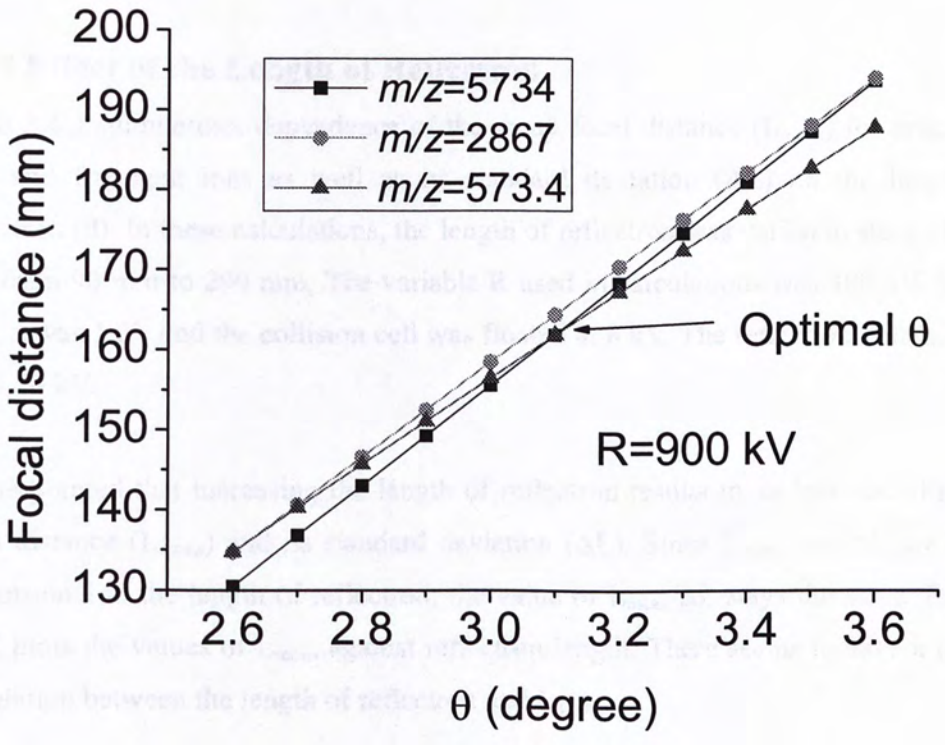

Figure 3.4.6 The relationship of focal distances of precursor ions (*m/z* 5734) and fragment ions (*m/z* 2867 and *m/z* 573.4) versus θ when R is 900 kV. R and θ are two variables in the electric field equation of curved-field reflectron. The optimal θ is at which the standard deviation of focal distances for precursor ions and fragment ions is minimum.

maximum value.

3.4.5 Effect of the Length of Reflectron

Table 3.4.3 summarizes dependence of the mean focal distance (L_{mean}) for precursor ions and fragment ions as well as its standard deviation (ΔL) on the length of reflectron (d). In these calculations, the length of reflectron was varied in steps of 100 mm from 90 mm to 290 mm, The variable R used in calculations was 300 kV, θ was 9.0°, α was 1.0°, and the collision cell was floated at 8 kV. The reflection voltage was set at 20 kV.

It was pointed that increasing the length of reflectron results in an increase of mean focal distance (L_{mean}) and its standard deviation (ΔL). Since L_{mean} and ΔL are both proportional to the length of reflectron, the value of $L_{mean}/\Delta L$ stays the same. Figure 3.4.7 plots the values of L_{mean} against reflectron length. There seems to have a linear correlation between the length of reflectron and L_{mean}.

Table 3.4.3 Dependence of mean focal distance (L_{mean}) on length of reflectron. ΔL is standard deviation of focal distances for the precursor ions and fragment ions. The variable $L_{mean}/\Delta L$ is a factor defined to evaluate the simultaneously focusing power of curved-field reflectron.

Length of reflectron (mm)	L_{mean} (mm)	ΔL (mm)	$L_{mean}/\Delta L$
90	80.0	1.7	45.9
190	168.9	3.7	45.9
290	257.8	5.6	45.9
390	346.7	7.6	45.9
490	435.6	9.5	45.9
590	524.5	11.4	45.9
690	613.4	13.4	45.9
790	702.3	15.3	45.9

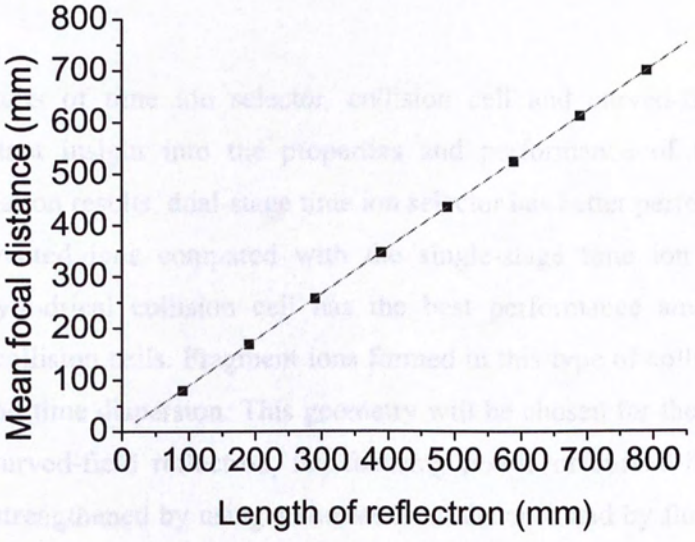

Figure 3.4.7 Plot of mean value of temporal focal distance against length of reflectron.

3.5 Conclusions

Simulation results of time ion selector, collision cell and curved-field reflectron provide important insight into the properties and performance of these devices. From the simulation results, dual-stage time ion selector has better performance on the selection of wanted ions compared with the single-stage time ion selector. The field-shaped cylindrical collision cell has the best performance among the three geometries of collision cells. Fragment ions formed in this type of collision cell have small spatial and time dispersion. This geometry will be chosen for the new collision cell. For the curved-field reflectron, the focusing power of curved-field reflectron (CFR) can be strengthened by using a shorter focal distance and by floating collision cell at high voltage. Under this condition, floating the collision cell at 8 kV gives the best spatial focusing properties. Due to the physical dimensions of current MALDI-TOF instrument, focal distance should be at least 280 mm. The optimized curved-field reflectron is 290 mm long with R being 230 kV; θ being 11.1°. This geometry gives an optimized focal distance of 280 mm with a standard deviation of 5.5 mm.

Chapter Four

Construction and Performance Evaluation of Modified Time-of-flight Mass Spectrometer

4.1 Benchmark Results for the Origin Reflectron Time-of-flight Mass Spectrometer

The PSD spectrum of Angiotensin II (DRVYIHPF, m/z 1047) is presented in Figure 4.1.1. The b, y ions[104,105] can be identified in Figure 4.1.1. The b, y ions are the fragment ions generated from breaking of the peptide bond. The PSD spectrum was obtained by pasting 19 segment spectra into a single spectrum. The reflection voltage corresponding to each segment spectrum is 20, 18.5, 15.65, 12.65, 10.45, 8.45, 6.9, 5.7, 4.55, 3.72, 2.98, 2.38, 1.96, 1.58, 1.27, 1.02, 0.84, 0.69 and 0.57 kV. The first segment spectrum was acquired under 10-20 laser shots, and the other segment spectrums were acquired under 50-200 laser shots. Generally speaking, at lower reflection voltage, the sensitivity is lower and thus requiring more acquisition to give desirable signal-to-noise ratios. It is important to note that different segments were acquired using different number of laser shots, the relative abundance information obtained from the PSD spectrum has no direct relationship with the ease of fragment ion formation under PSD conditions.

4.2 Hardware Modifications of Reflectron Time-of-flight Mass Spectrometer

The modification of our current instrument involves incorporating an extension tube, a collision cell and a curved-field reflectron. Due presumably to the introduction of new extension tube (with some welding joints), the pressure inside the instrument was increased from 3 x 10^{-7} mbar to 5×10^{-6} mbar. In order to avoid any discharges during the delay extraction event, and an extra turbomolecular pump was installed to maintain the pressure at 5×10^{-7} mbar. The schematic diagram and photograph of the modified instrument is shown in Figure 4.2.1 and Figure 4.2.2.

4.2.1 Collision Cell

The collision cell is made of aluminum alloy, and has the overall length of 137 mm

with 60 mm-length collision region (Figure 4.2.3 and Figure 4.2.4).

The collision gas was introduced through a 200 mm-length (Ø 0.53 μm) GC column into the collision cell. The ions enter and leave the collision cell through an orifice. The diameter of the orifice can be adjusted so that the pressure inside the collision cell is much higher than that outside the collision cell without decreasing the transmission of ion beam.

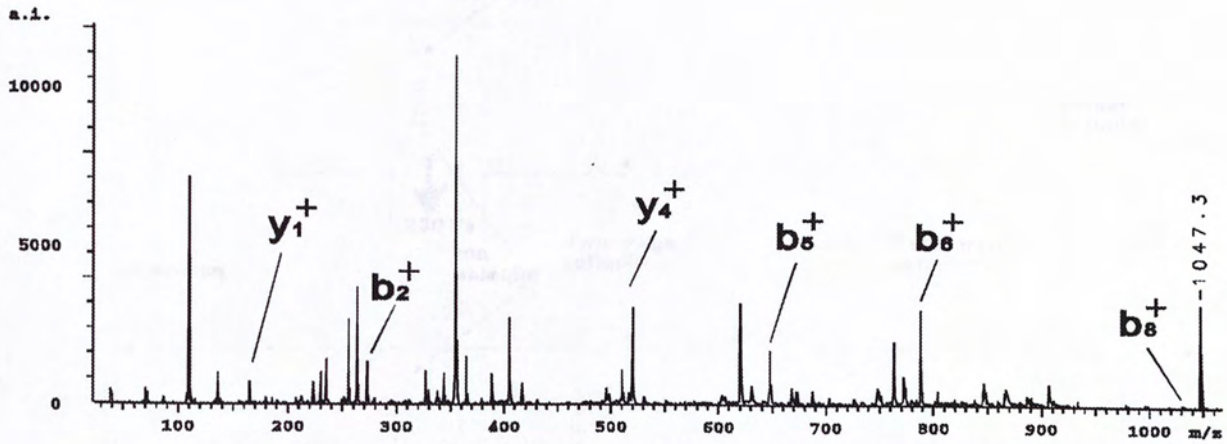

Figure 4.1.1 PSD spectra of AngiotensinII for the two-stage reflectron time-of-flight mass spectrometer.

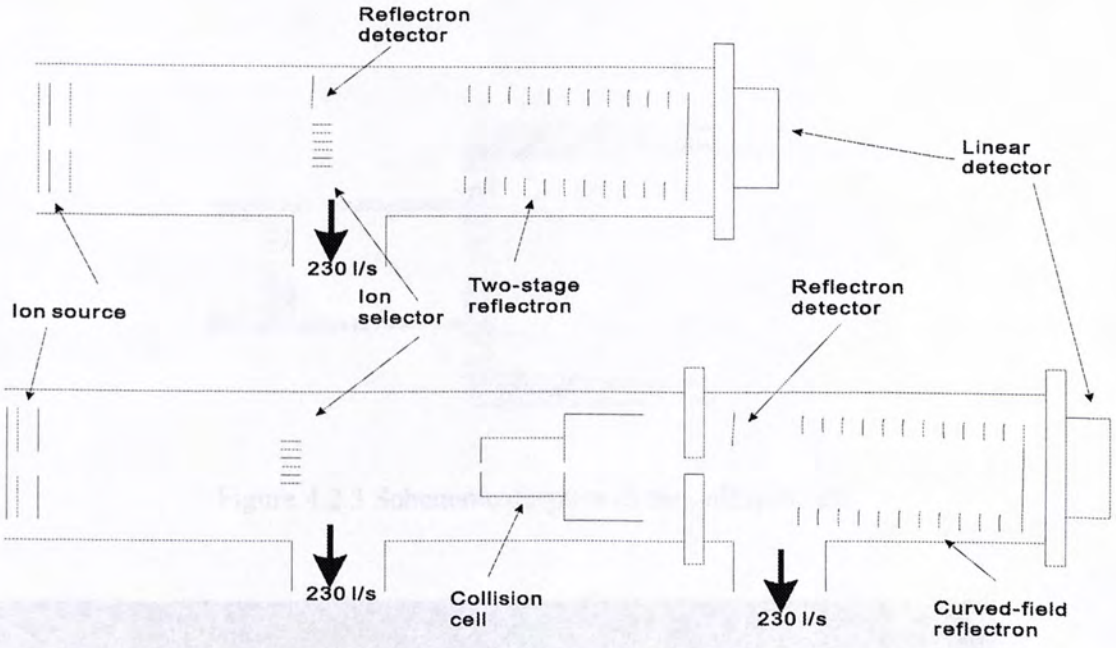

Figure 4.2.1 Schematic diagram of instrument before (top) and after (bottom) modification.

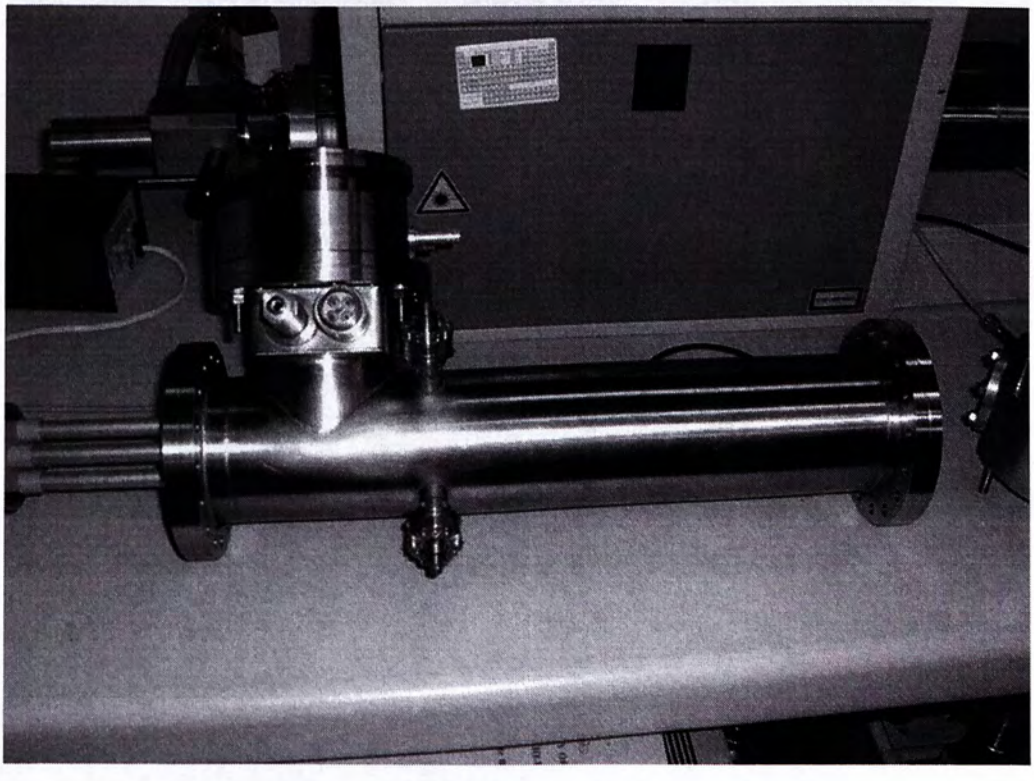

Figure 4.2.2 A Photograph of extension tube.

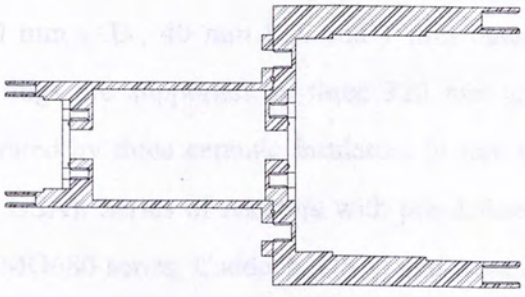

Figure 4.2.3 Schematic diagram of the collision cell.

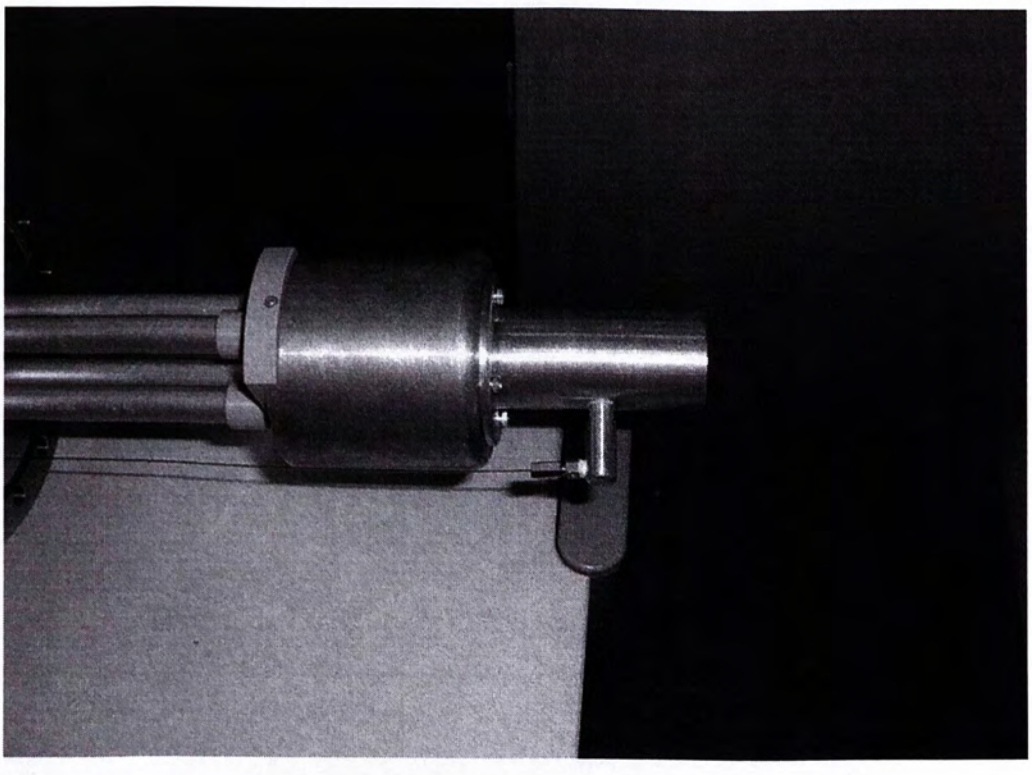

Figure 4.2.4 A photograph of the collision cell.

4.2.2 Curved-field Reflectron

The curved-field reflectron (Figure 4.2.5 and Figure 4.2.6) is made up of 31 stainless steel plates (80 mm O.D., 40 mm I.D. and 1 mm thickness, Lesker, USA). These stainless steel rings are supported by three 320 mm-length plastic rods. Adjacent plates are separated by three ceramic insulators (9 mm O.D., 5 mm I.D. and 9 mm thickness, SIS, USA). Series of resistors with pre-defined resistances were obtained commercially (MG680 series, Caddock, USA) and were spot-welded on the stainless steel plates.

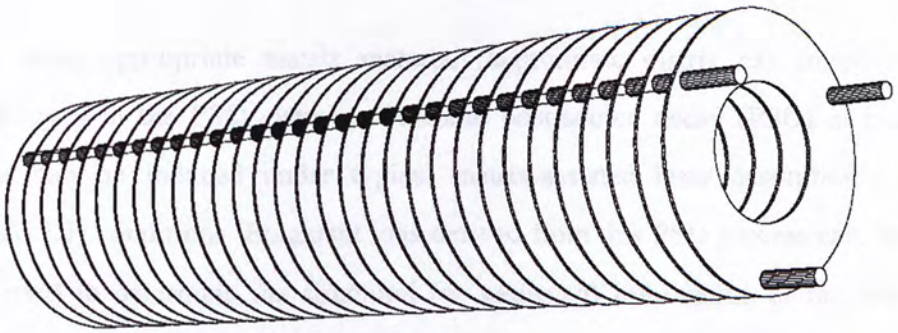

Figure 4.2.5 Schematic diagram of the curved-field reflectron.

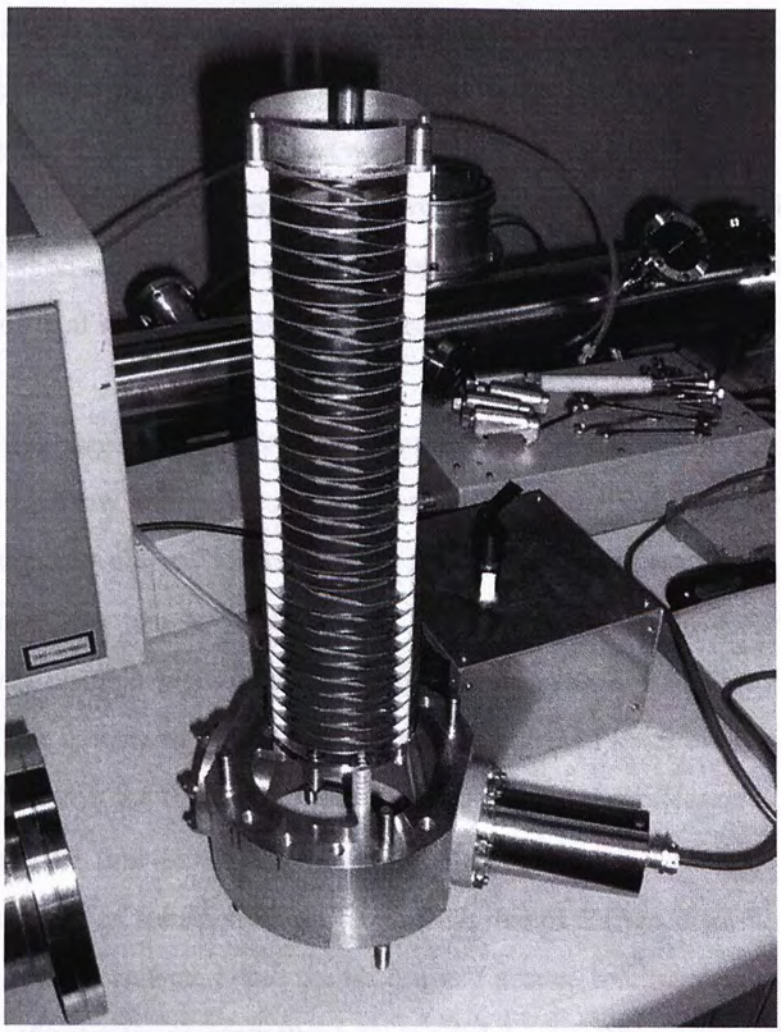

Figure 4.2.6 A photograph of curved-field reflectron.

4.3 Evaluation of the Curved-field Reflectron

By using appropriate matrix material (appropriate matrix can improve fragment efficiency in the PSD event), substantial post-source decay (PSD) of biomolecular ions can be induced under typical matrix-assisted laser desorption / ionization (MALDI) conditions. Fragment ions derived from this PSD process can, in principle, be used to determine the structural (or sequence) information of the selected ions. Using linear time-of-flight mass analyzer, this information cannot normally be retrieved because the same arrival time of the residual precursor ions and the resulting PSD fragment ions. In high vacuum conditions, fragment ions of different *m/z* ratios derived from the same precursor ions will retain the same velocity as that of the precursor ions. Therefore, there is no variation of time-of-flight for these ions to travel through the same distance of field-free region before impinging onto the detector. Situation becomes more complicated when a reflectron (an ion mirror) is placed at the end of the field-free region. Since a reflectron is an energy sensitive device, the exact flight path of an ion within the reflectron depends critically on the energies of the ions and the profile of the electric field within the reflectron.

A typical two-stage linear reflectron is designed to provide high-order focusing for ions with a narrow energy distribution, such as those derived from the variation of initial desorption velocity. Therefore, only fragment ions with *m/z* very close to that of the precursor ions can be time-resolved, properly reflected and detected by using conventional channel plate detector. Fragment ions with *m/z* smaller than a certain value will not be able to penetrate to the second potential stage of the reflectron and will be reflected at the first and steeper potential stage to the reflectron detector. These ions will not be time-resolved at the reflectron detector. In addition, the reflection angle is many often substantially different from that of the precursor ions, these ions might not even be reflected onto the reflectron detector. To circumvent this situation, the PSD information is normally be acquired by pasting spectra obtained with

different reflectron voltage while maintaining the acceleration voltage constant. Figure 4.3.1 shows a typical reconstructed PSD mass spectrum of a small peptide, Angiotensin II (MW 1047). Series of b- and y-type fragment ions can clearly be identified.

A single-stage reflectron can, in principal, reflect and time-resolve both the residual precursor ions and fragment ions of different *m/z* values. For the one with a linear retarding field, the time-focusing positions for ions of different energies (i.e. ions of different *m/z* values for PSD fragments) fall onto different locations. Using a typical point detector, only selected ions within a small window of *m/z* values are time-focused. As the *m/z* values of other fragment ions derivate from those selected ions, there is a progressive spreading (or blurring) of their time-focusing points. By properly adjusting the curvature of the retarding field, the spread of the time-focusing positions for ions of different energies can be minimized. Figure 4.3.2 shows the PSD spectrum of Angiotensin II obtained with the curved-field reflectron. The acceleration potential was 18.00 kV and the end-plate of the reflectron was 18.01 kV. Fragment ions with *m/z* larger than 50% of that of the precursor ions can be properly time-focused onto the detector by the curved-field reflectron. The spectral resolution remains more or less constant across the spectrum.

With reference to the Figure 4.3.1, it is important to note that fragment ions with *m/z* smaller than 50% of that of the precursor ions could not be acquired. A plausible explanation is related to the limitation of the off-axis detection system. As shown in Figure 4.3.3(a), ions with different *m/z* values will be reflected at different depths of the reflectron. Even the reflection angle remains the same, there is a lateral dispersion for ions reflected at different depths of the reflectron. Using an off-axis detector with limited detection area, it is conceivable that only a portion of the fragment ions can be sampled by the detector. To validate this argument, additional spectra were acquired with lower end-plate reflectron potentials. As shown in Figure 4.3.3 (b)-(c), reduction of the reflectron potential can move the reflection positions of low-mass fragment

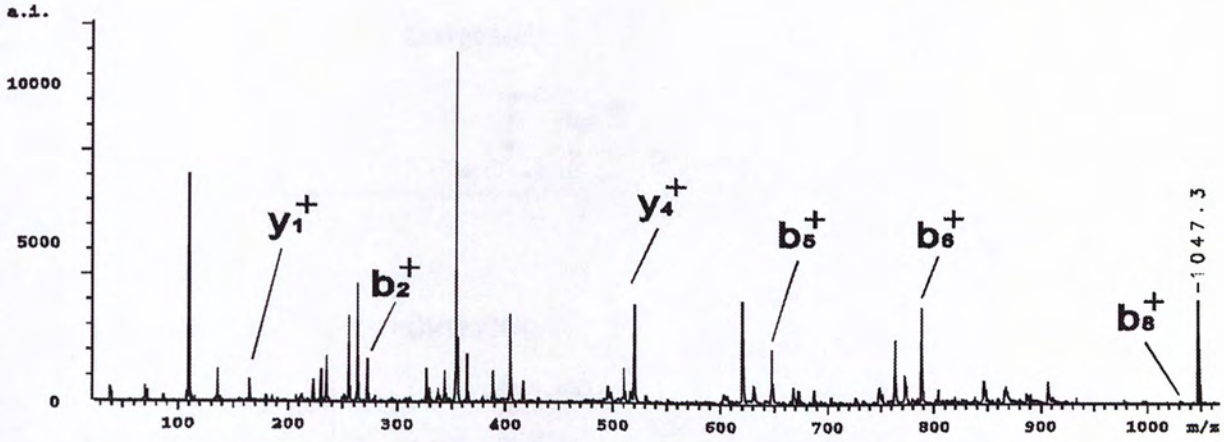

Figure 4.3.1 PSD spectra of AngiotensinII for the two-stage reflectron time-of-flight mass spectrometer.

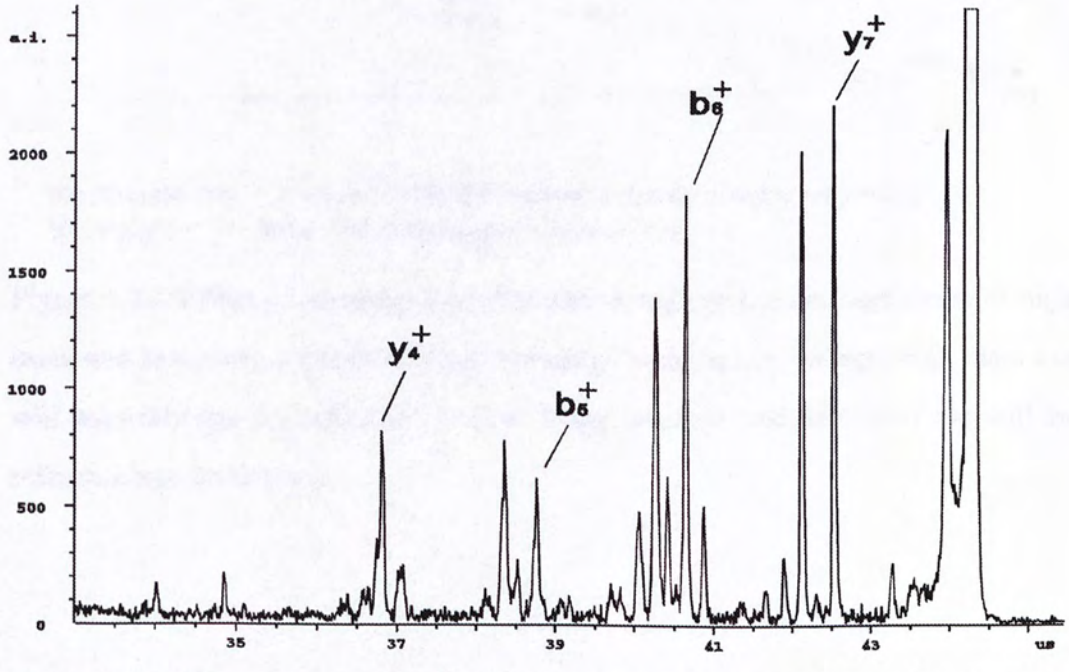

Figure 4.3.2 PSD spectra of AngiotensinII acquired by curved-field reflectron. The reflectron voltage is 18.01kV.

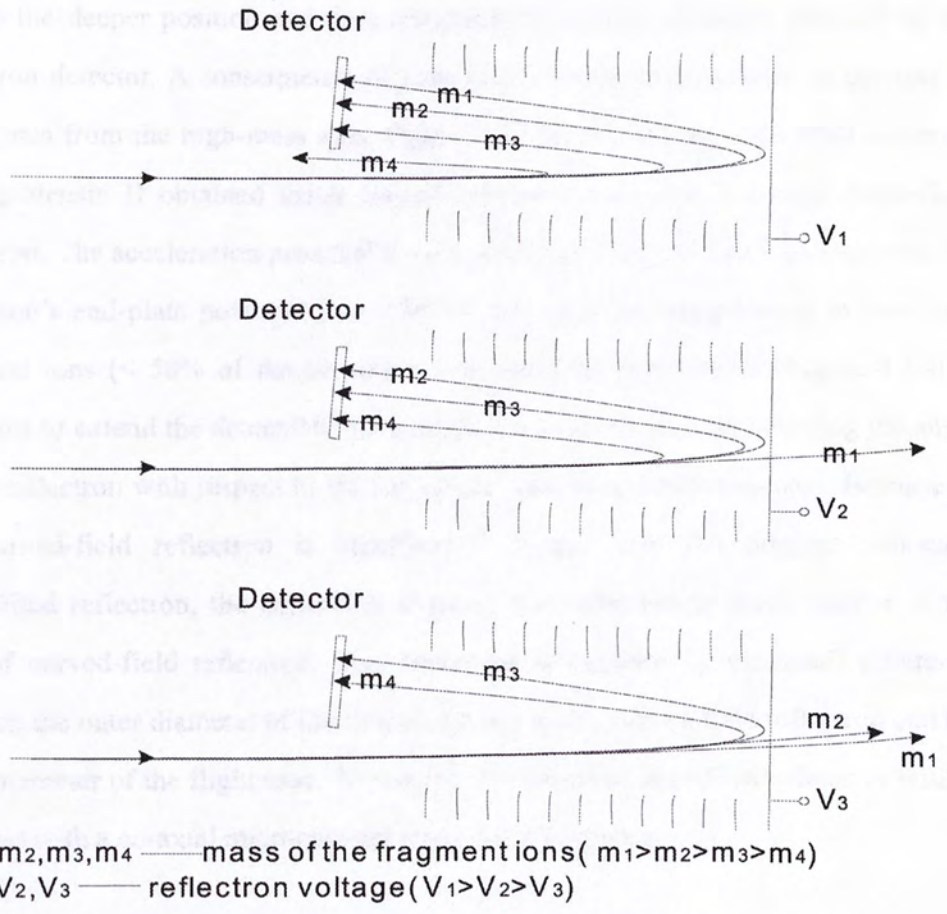

Figure 4.3.3 Effect of scanning the reflectron voltage on the ion trajectories of high mass and low mass fragments. When reducing the reflectron voltage, high mass ion will pass through the reflectron without being detected, and low mass ion will be reflected into the detector.

ions to the deeper position and thus enhancing the chance of being detected by the reflectron detector. A consequence of reducing the reflectron potential is the loss of the signals from the high-mass ions. Figure 4.3.4(a) and (b) show the PSD spectrum of Angiotensin II obtained using curved-field reflectron and two-stage linear-field reflectron. The acceleration potential for the precursor ions was 18.00 kV; whereas the reflectron's end-plate potential was 9.90 kV. Ion signals corresponding to low-mass fragment ions (< 50% of the precursor ion) could be registered in Figure 4.3.4(a). Attempts to extend the detectable mass range for fragment ions by adjusting the angle of the reflectron with respect to the ion optical axis have limited success. Because of the curved-field reflectron is significantly longer than the original two-stage linear-filed reflectron, the adjustable angle of the reflectron is much smaller in the case of curved-field reflectron. This limitation is imposed by the small difference between the outer diameter of the ring electrodes in the curved-field reflectron and the inner diameter of the flight tube. To resolve this situation, the off-axis detector will be replaced with a co-axial microchannel plate (MCP) detector.

Despite of the wider detectable mass range, spectrum obtained with curved-field reflectron is generally of lower resolution in comparison with that obtained with two-stage linear-field reflectron. Figure 4.3.5 shows a hypothetical plot of the distribution of potential along the depth of the reflectron for both two-stage linear-field reflectron and curved-field reflectron. As expected, ions of different *m/z* that could be reflected at the second-stage of the two-stage linear-field reflectron would be reflected at closer positions in the curved-field reflectron. This is essentially implying a general reduction of the spectral resolution in curved-field reflectron in comparison with that of two-stage linear field reflectron.

4.4. Evaluation of the field-shaped cylindrical collision cell

Figure 4.4.1 shows the details schematic diagram of the original wiring and tubing of

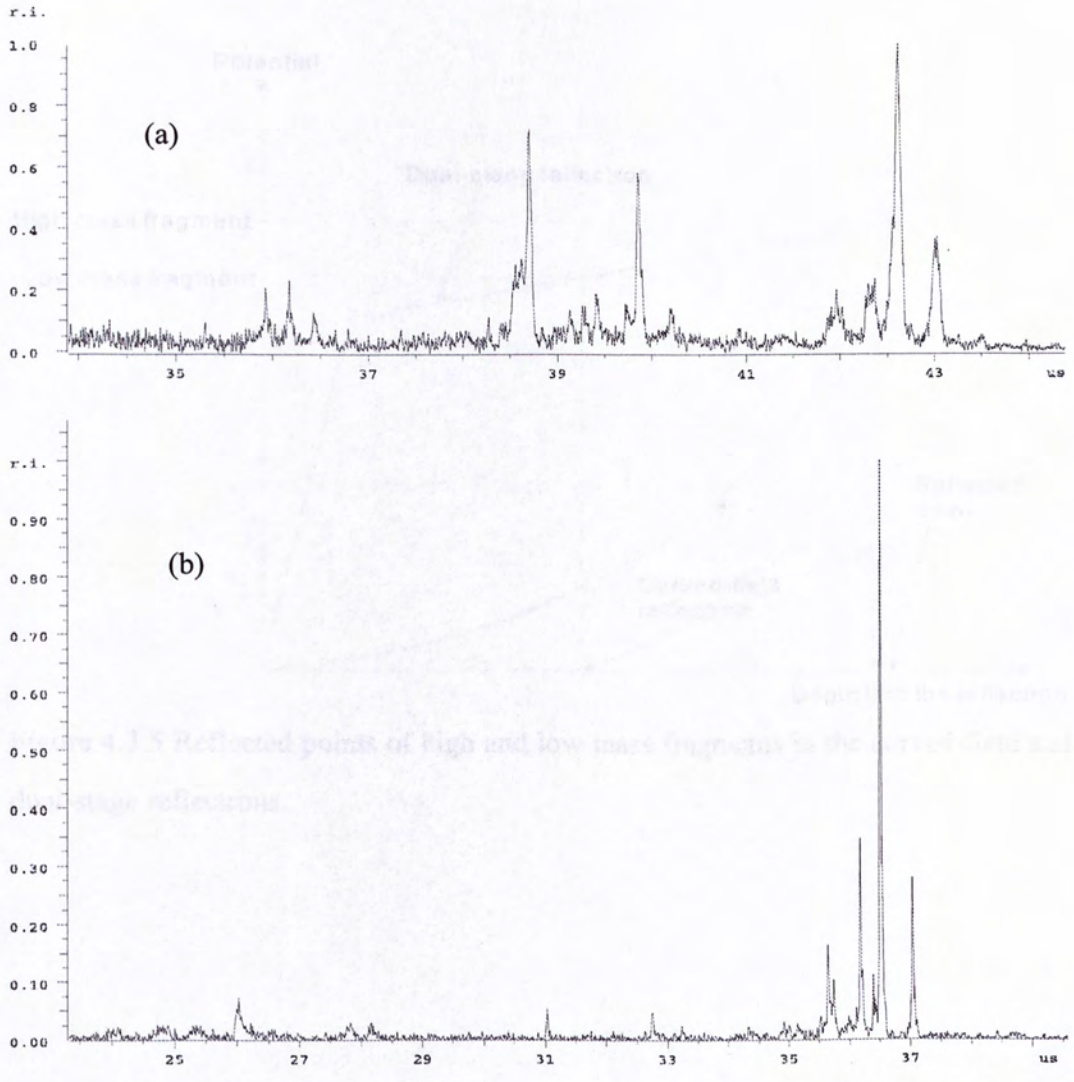

Figure 4.3.4 Mass range recorded by curved-field reflectron (a) and dual-stage reflectron (b) under a lower reflectron voltage. The reflectron voltage for curved-field reflectron is 9.90kV.

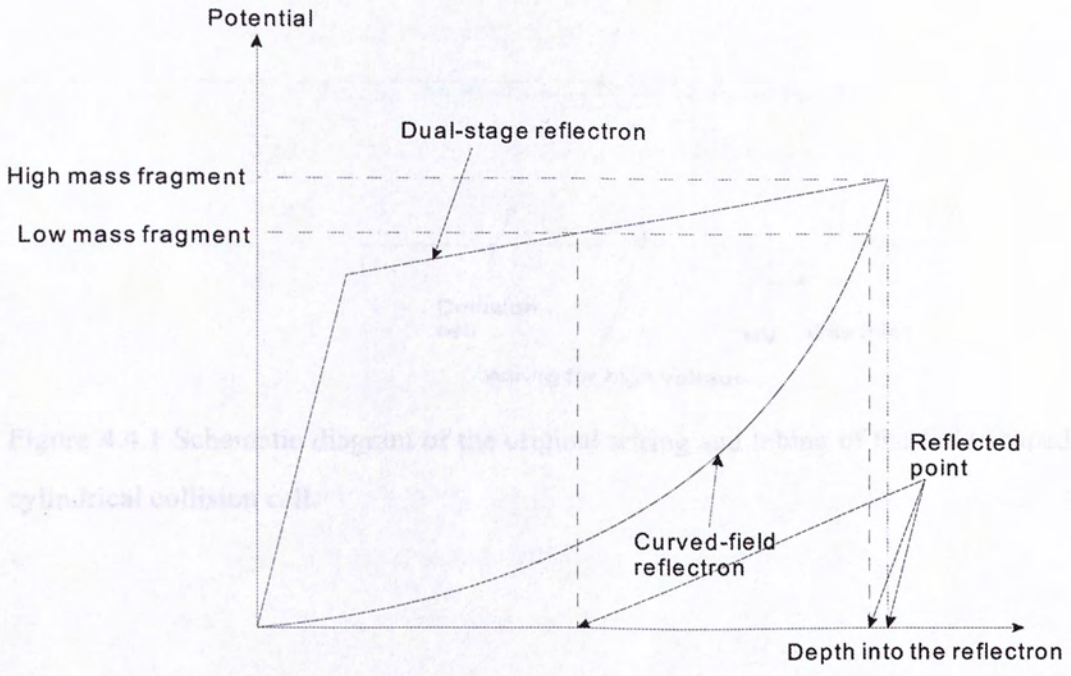

Figure 4.3.5 Reflected points of high and low mass fragments in the curved-field and dual-stage reflectrons.

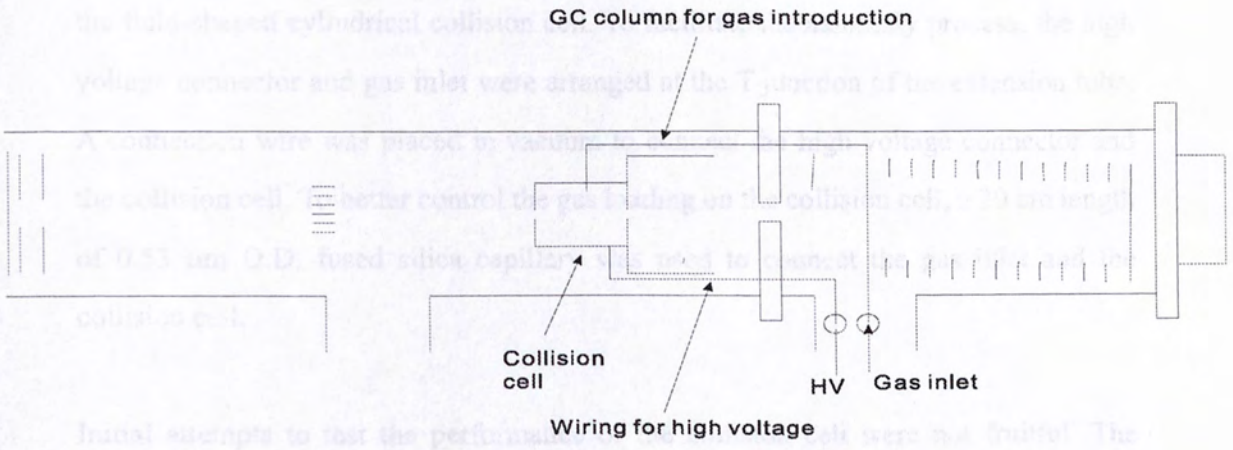

Figure 4.4.1 Schematic diagram of the original wiring and tubing of the field-shaped cylindrical collision cell.

the field-shaped cylindrical collision cell. To facilitate the assembly process, the high voltage connector and gas inlet were arranged at the T-junction of the extension tube. A connection wire was placed in vacuum to connect the high voltage connector and the collision cell. To better control the gas loading on the collision cell, a 20 cm length of 0.53 μm O.D. fused silica capillary was used to connect the gas inlet and the collision cell.

Initial attempts to test the performance of the collision cell were not fruitful. The precursor ion signal was largely suppressed when a high voltage of 1-2 kV was loaded onto the collision cell (see below for explanation). Therefore, much of the evaluation work was conducted on the grounded collision cell. Upon loading the collision gas, the base pressure of the instrument was elevated from 5.0×10^{-7} mbar to 2.5×10^{-6} mbar. Angiotensin II precursor ions were accelerated to 18.00 keV and were selected using the time ion-selector before directing into the collision cell for dissociation experiments. The reflectron voltage was set at 18.01 kV. Figure 4.4.2 (a) and (b) show the CID spectrum and the PSD spectrum of the Angiotensin II ions. As expected, the precursor ion intensity in the CID spectrum is only 10% of that of the PSD spectrum. However, it was noted that the high mass PSD fragment ions were also attenuated substantially under CID conditions. Since the measurement of low-mass fragment ions was prohibited by the small active area of the reflectron detector, the reflectron voltage was successively reduced to make the measurement feasible. From Figure 4.4.3 - 4.4.6, apart from a significant improvement of the low-mass fragment ion intensities, new fragment ions that were not observed in the corresponding PSD spectra could be detected in the CID spectra.

Regarding the precursor ion suppression effect at floated collision cell, it was recently discovered that this effect was caused by the wiring of the instrument, as shown in Figure 4.4.1. At high voltage, the wire connecting the high voltage connector and the collision cell would generate substantial stray field around the entrance of the reflectron and hence deflecting the precursor ion beam. Attempts to shield the wiring

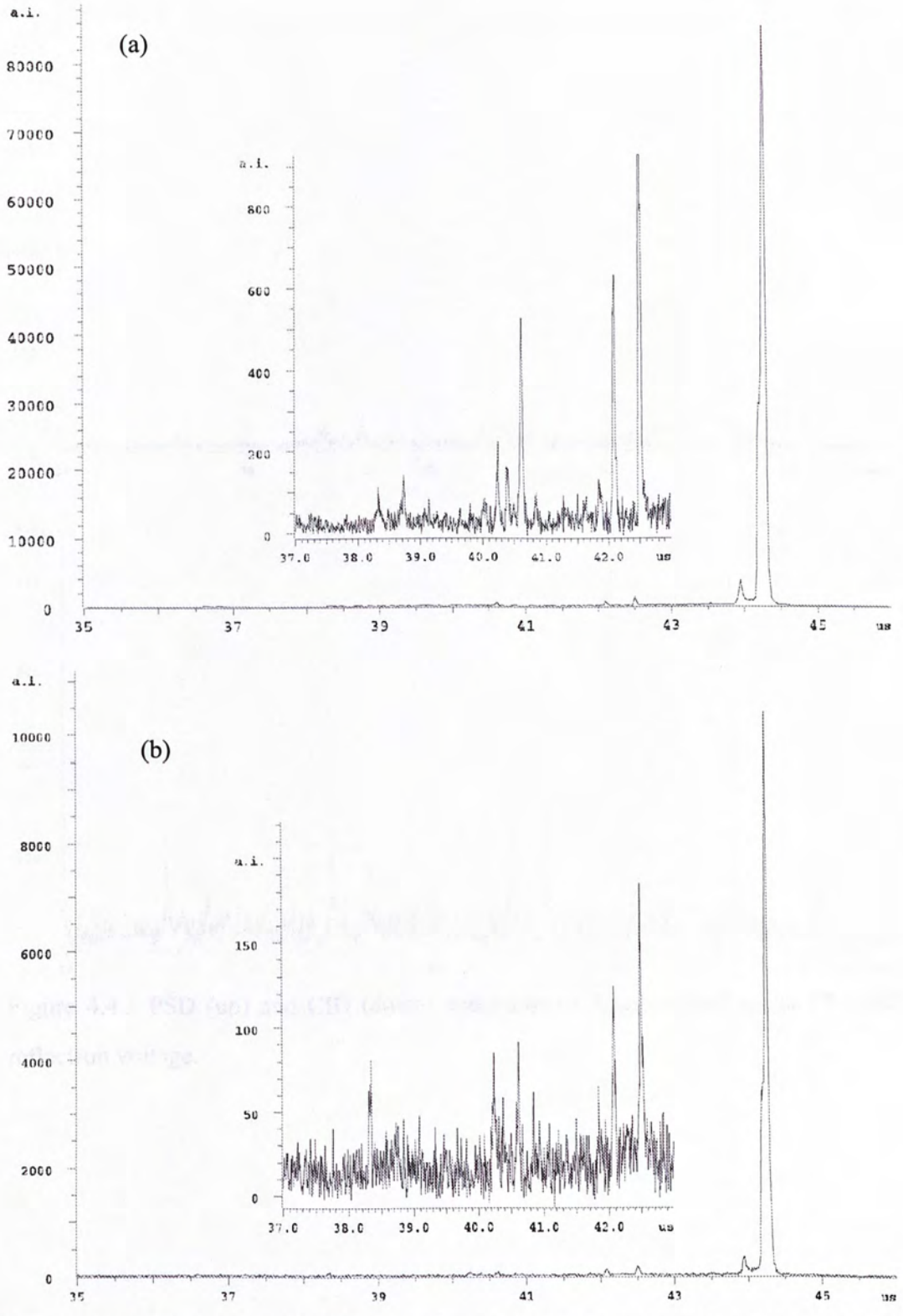

Figure 4.4.2 PSD (a) and CID (b) spectrums of AngiotensinII under 18.01kV reflectron voltage.

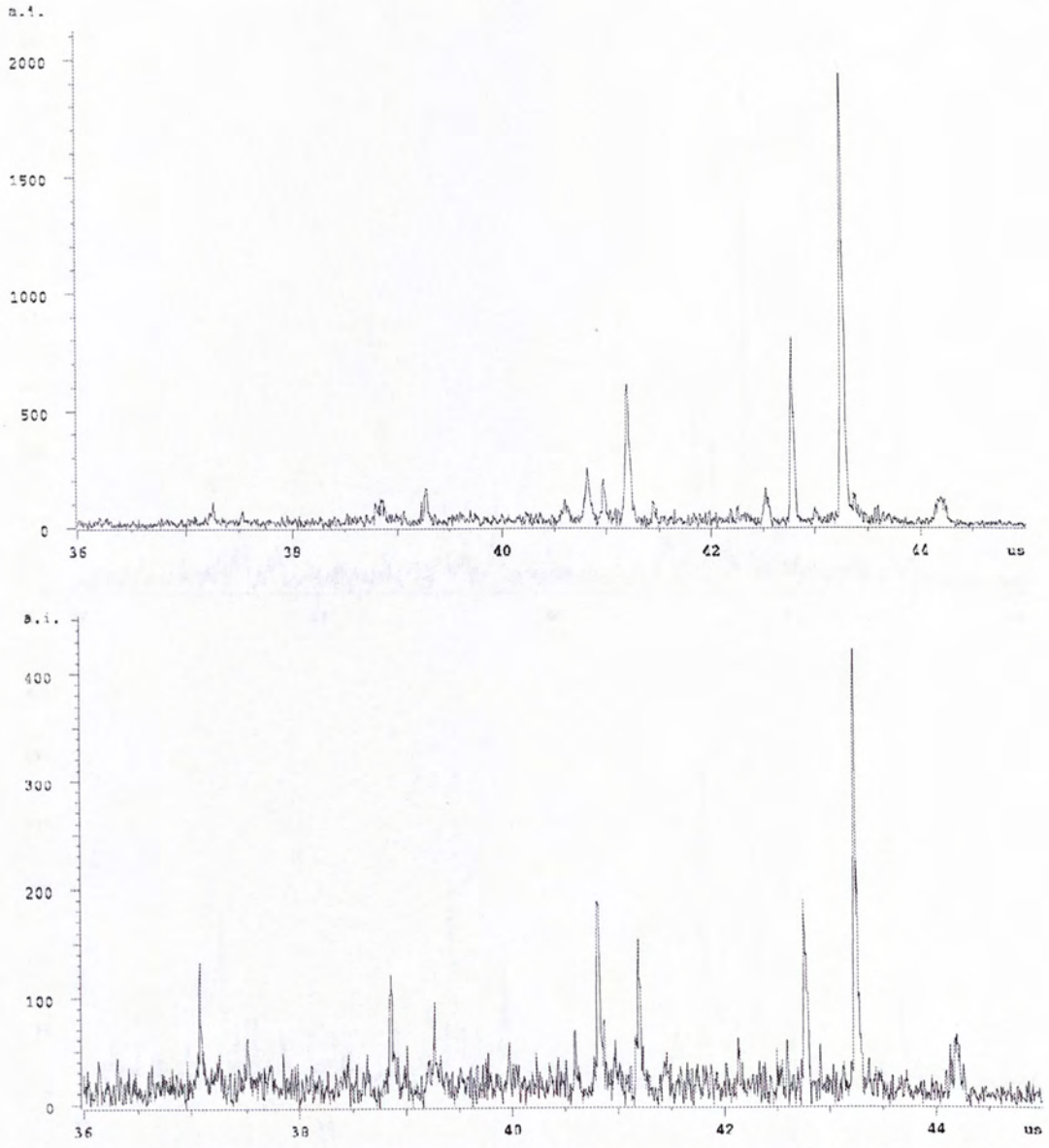

Figure 4.4.3 PSD (up) and CID (down) spectrums of AngiotensinII under 17.01kV reflectron voltage.

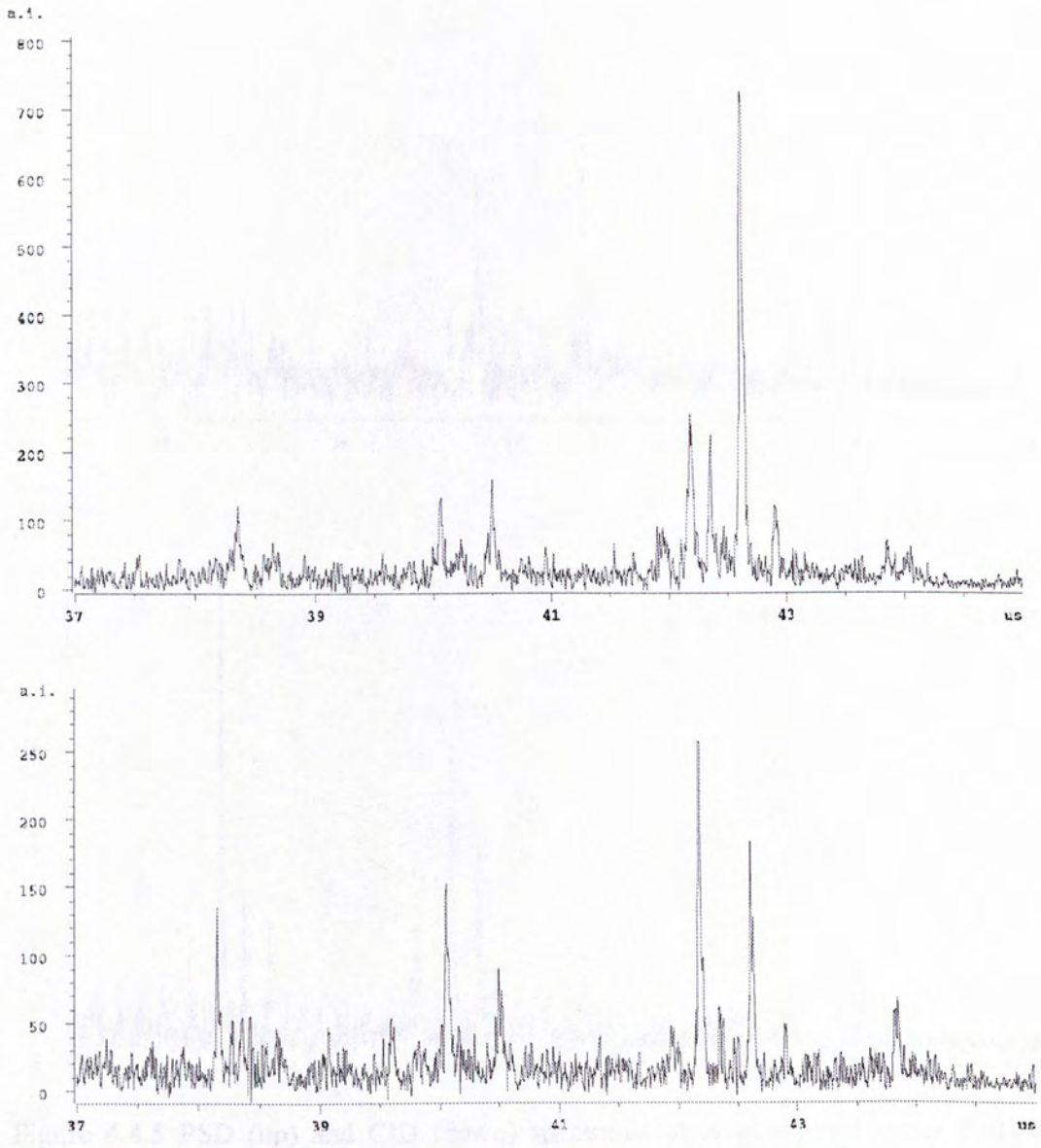

Figure 4.4.4 PSD (up) and CID (down) spectrums of AngiotensinII under 15.01kV reflectron voltage.

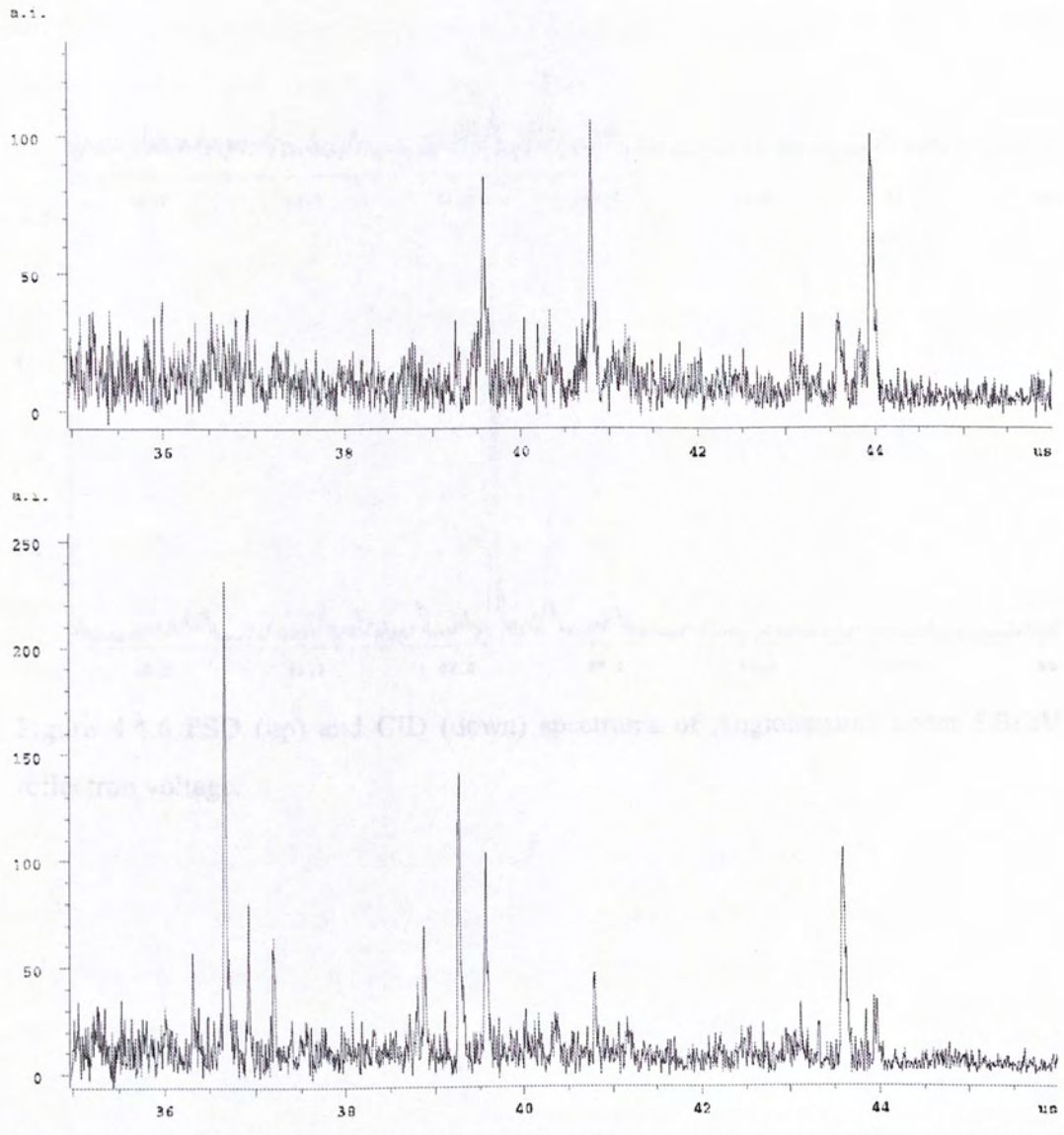

Figure 4.4.5 PSD (up) and CID (down) spectrums of AngiotensinII under 9.01kV reflectron voltage.

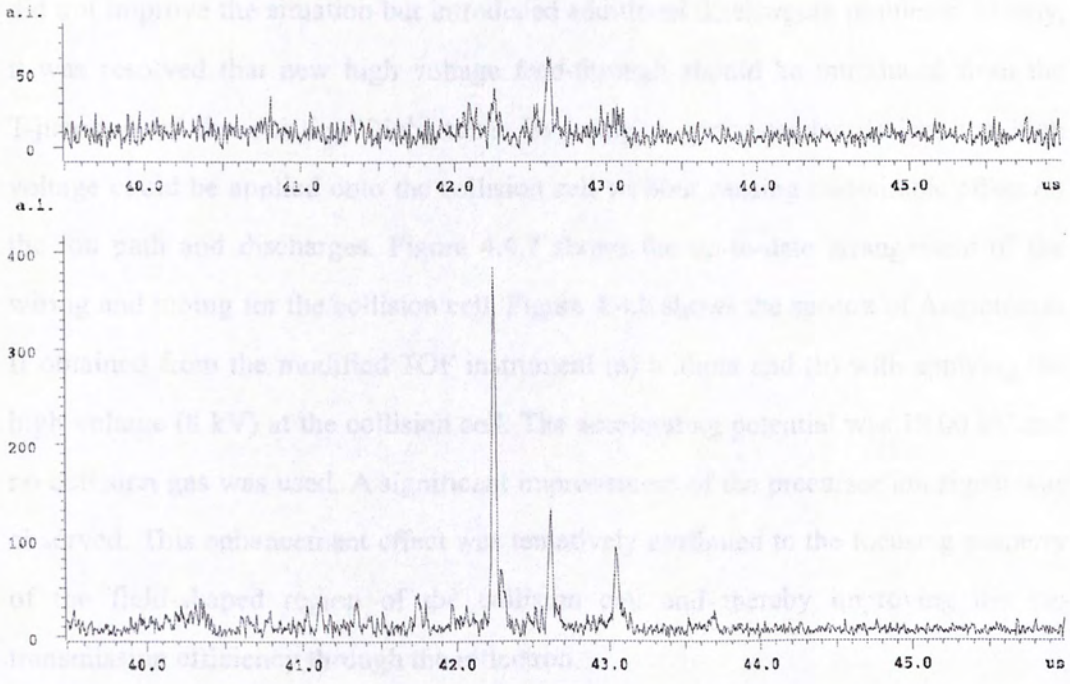

Figure 4.4.6 PSD (up) and CID (down) spectrums of AngiotensinII under 5.01kV reflectron voltage.

did not improve the situation but introduced additional discharging problems. Finally, it was resolved that new high voltage feed-through should be introduced from the T-junction of the existing flight tube. By using a spring-loader design, the high voltage could be applied onto the collision cell without causing undesirable effect on the ion path and discharges. Figure 4.4.7 shows the up-to-date arrangement of the wiring and tubing for the collision cell. Figure 4.4.8 shows the spectra of Angiotensin II obtained from the modified TOF instrument (a) without and (b) with applying the high voltage (8 kV) at the collision cell. The accelerating potential was 18.00 kV and no collision gas was used. A significant improvement of the precursor ion signal was observed. This enhancement effect was tentatively attributed to the focusing property of the field-shaped region of the collision cell and thereby improving the ion transmission efficiency through the reflectron.

4.5 Conclusions

The proposed field-shaped cylindrical collision cell and curved-field reflectron were fabricated and were successfully installed into the Bruker MALDI time-of-flight mass spectrometer. Several practical challenges were encountered during the instrumental evaluation and thus prohibiting the full realization of the potential of this tandem time-of-flight instrument prior to the writing of this thesis. However, the preliminary evaluation of these devices has shown promising results. The field-shaped device in the collision cell was found to improve not only the collection efficiency of the fragment ions but also the precursor ion intensity. Collision-induced dissociation of the model peptide ions was successfully demonstrated by using reduced reflectron potential(s). In comparison with that of PSD results obtained from two-stage linear-field reflectron, substantial reduction of the spectral resolution was resulted by using curved-field reflectron. The expected improvement in spectral resolution using floated collision cell remains to be demonstrated in future. Experiments to improve the instrumental design is in progress, including (a) the replacement of the off-axis detector with a co-axial detector; (b) installation of the flowmeter for fine control of

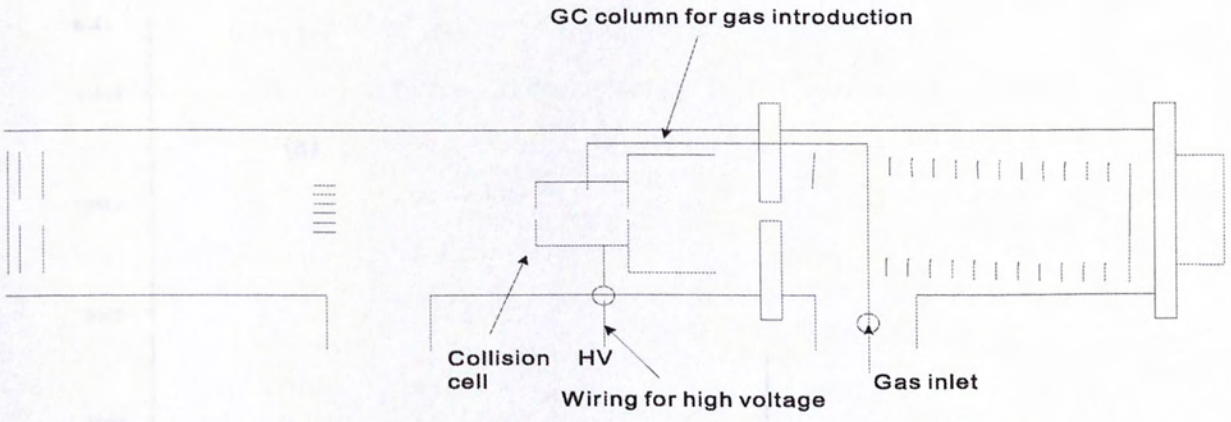

Figure 4.4.7 Up-to-date arrangement of the wiring and tubing for the collision cell.

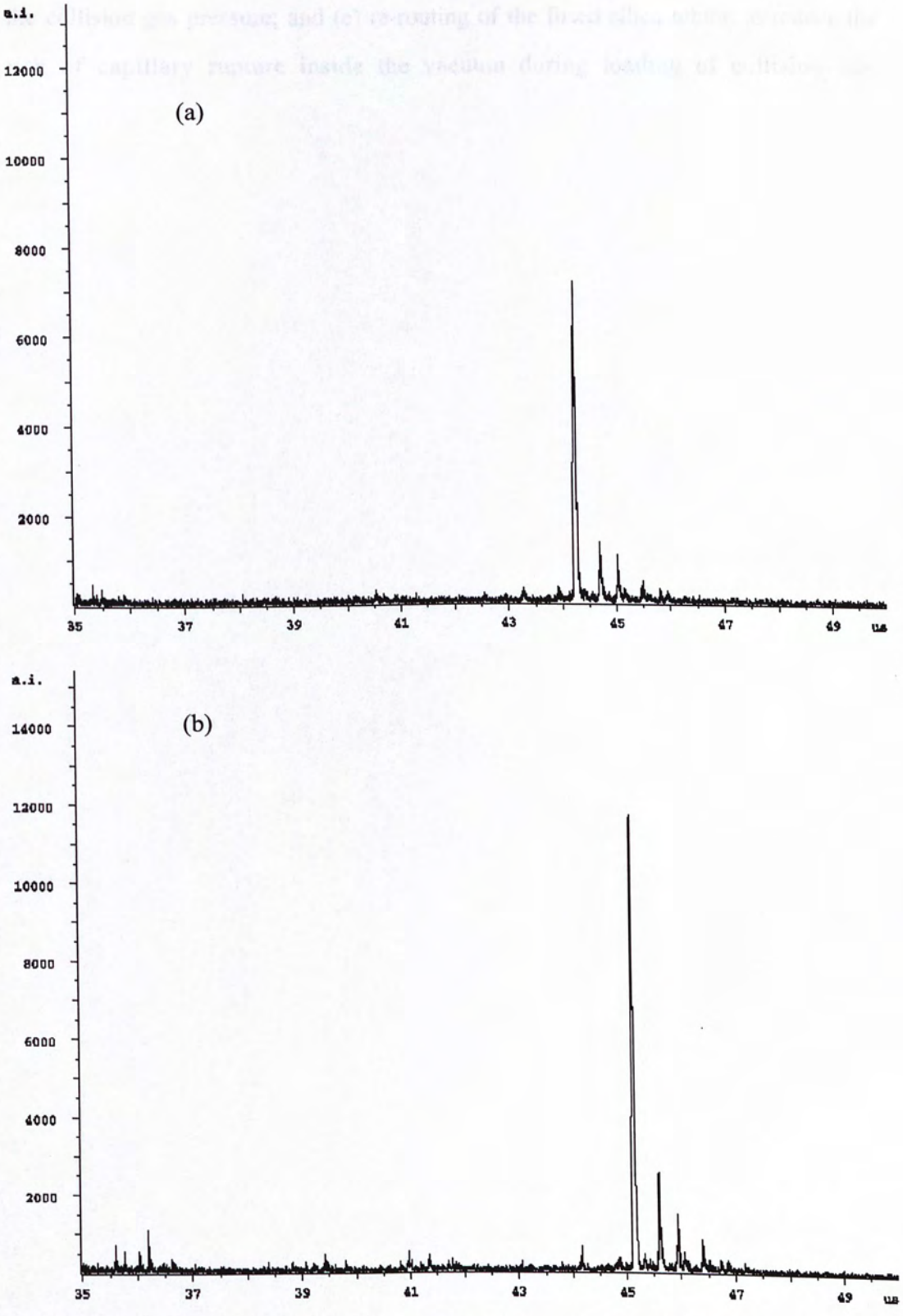

Figure 4.4.8 Spectra of Angiotensin II obtained from the modified TOF instrument (a) without and (b) with applying the high voltage (8 kV) at the collision cell.

the collision gas pressure; and (c) re-routing of the fused silica tubing to reduce the risk of capillary rupture inside the vacuum during loading of collision gas.

Chapter Five
Concluding Remarks

5.1 Concluding Remarks

This project includes simulations of time ion selector, collision cells and curved-field reflectron, and designs of the collision cell and curved-field reflectron. The electronic device for the current single-stage time ion selector is not suitable to the dual-stage time ion selector, and a lot of time should be spent in designing a new electronic device, so the design of dual-stage time ion selector will be considered as a part of my next project.

The discharge to the computer caused by applying high voltage to the collision cell has been eliminated recently by changing the way of applying high voltage, and after the ordered co-axial detector arrived, the experiments will be continued.

Further tuning of the delay extraction voltage, reflectron voltage, and gas pressure inside the collision cell is necessary to improve the performance of new mass spectrometer. The mass calibration procedure of this new mass spectrometer is not included in this thesis, because we cannot get a spectrum of the fragment ions and precursor ions within full mass range at a time using current off-axis detector, and the study of calibration equations for the new instrument is on the way.

References

1. Vastola, F. J.; Mumma, R. O. and Pirone, A.; *J. Org. Mass Spectrom.* 1970, **3**,101.
2. Posthumus, M. A.; Kistemker, P. G.; Meuzelaar, H. L. C.; deBrauw, M.C. tenNoever; *Anal. Chem.* 1978, **50**, 985.
3. Stoll, R. and Rollgen, F. W.; *Org. Mass Spectrom.* 1979, **14**, 642.
4. Cotter, R.J.; *Anal. Chem.* 1981, **53**, 1306.
5. Hardin, E.D. and Vestal, M.L.; *Anal. Chem.* 1981, **53**, 1492.
6. Karas, M. and Hillenkamp, F.; *Anal. Chem.* 1988, **60**, 2299.
7. Karas, M. and Bahr, U.; *Mass Spectrom. Rev.* 1991, **10**, 335.
8. Overberg, A.; Hassenburger, A.; Hillenkamp, F.; *In Mass Spectrometry in biological Sciences*: *a tutorial,* M. L. Gross (Ed.), Kluwer Academic Publisher, Amsterdam, 1992, p181.
9. Mock, K. K.; Davey, M. and Cottrell, J. S.; *Biochem. Biophy. Res. Commun.*, 1991, **177**, 2, 644.
10. Harvey, D. J.; *Rapid Commun. Mass Spectrom.*, 1993, **7**, 614.
11. Chan, T.-W.D.; Colburn, A. W. and Derrick, P. J.; *Org. Mass Spectrom.*; 1992, **27**, 53.
12. Wada, Y.; Gu, J. G.; Okamoto, N. and Inui K.; *Biol. Mass Spectrom.* 1994, **23**, 108.
13. Chait, B. T.; Wang, R.; Beavis, R. C. and Kent, S. B.; *Science* 1993, **262**, 89.
14. Moniatte, M.; Van der Goot F. G.; Buckley, J. T.; Pattus, F. and Van, D. A.; *FEBS Lett.* 1996, **384**, 269.
15. Nelson, R. W.; Dogruel, D. and William, P.; *Rapid Commun. Mass Spectrom.* 1994, **8**, 627.
16. Strupat, K. and Karas M.; Hillenkamp, F.; *Int. J. Mass Spectrom Ion Proc.* 1991, **11**, 89.
17. Rademark, G. J.; Pergantis, S. A.; L. Blok- Tip J. I. Langride; Kleen, A.; Thomas Oates, J. E.; *Anal. Chem.* 1998, **257**, 149.
18. Hillenkamp, F.; Karas, M.; Beavis, R. C. and Chait, B. T.; *Anal. Chem.* 1991, **63**,

1193A.

19. Andersen, J. S. and Svensson B.; *Nature*, 1996, **14**, 449.
20. Karas, M.; Bachmann, D.; Bahr, U.; Hillenkamp, F.; *Int. J. Mass Spectrom. Ion Proc.* 1987, **78**, 53.
21. Karas, M.; Bahr, U.; Giessman, U.; *Mass Spectrom. Rev.* 1991, **10**, 335.
22. Cotter, R.; *Anal. Chem.* 1992, **64**, 1027A.
23. Hillenkamp, F.; Karas, M.; *Methods in Enzymology, Vol193: Mass Spectrometry.* Academic Press, New York, 1990, 280.
24. Beavis, R. C.; Chait, B. T.; *Anal. Chem.* 1990, **62**, 1836.
25. Ens, W.; Mao, Y.; Mayer, F.; Standing, K. G.; *Rapid Commun. Mass Spectrom.*, 1991, **5**, 117.
26. Speir, J. P.; Gorman, G. S. and Amster, I. J.; *Anal. Chem.* 1991, **63**, 65.
27. Ehring, H.; Hillenkamp, F. and Karas, M.; *Org. Mass Spectrom.* 1992, **27**, 472.
28. Tabet, J. C. and Cotter, R. J.; *Anal. Chem.* 1984, **56**, 1662.
29. Keesee, R. G. and Castleman, A. W.; *J. phys. Chem. Ref. Data,* 1986, **15**, 1011.
30. Solouki, T.; Gillig, K. J.; Russell, D.; *Rapid Commun. Mass Spectrom.*, 1994, **8**, 26.
31. Cornett, D. S.; Duncan, M. A.; Amster, I. J.; *Anal. Chem.* 1993, **65**, 2608.
32. Fitzgerald, M. C.; Parr, G. R.; Smith, L. M.; *Anal. Chem.* 1993, **65**, 3204.
33. Beavis, R. C.; Chait, B. T.; *Rapid Commun. Mass Spectrom.*, 1989, **3**, 432.
34. Strupat, K.; Karas, M.; Hillenkamp, F.; *Int. J. Mass Spectrom. Ion Proc.* 1991, **111**, 89.
35. Beavis, R.C.; Chaudhary, T.; Chait, B. T.; *Org. Mass Spectrom.* 1992, 27, 156.
36. Juhasz, P.; Costello, C. E.; Biemann, K. *J. Am. Soc. Mass Spectrom.* 1993, **4**, 399.
37. Beavis, R. C.; Chait, B. T. In: Ens, W.; Standing, K. G., eds. *Methods and Mechanisms for Producing Ions from Large Molecules.* Plenum, New York, 1991. NATO Advanced Study Institute, Science Series.
38. Vertes, A.; Gijbels, R.; Levine, R. D.; *Rapid Commun. Mass Spectrom.*, 1990, **4**, 228.
39. Ehring, H.; Karas, M.; Hillenkamp, F.; *Org Mass Spectrom.* 1992, **27**, 472.

40. Gimon, M. E.; Preston, L. M.; Solouki, T.; White, M. A.; Russell, D. H.; *Org Mass Spectrom.* 1992, **27**, 827.

41. Balazs, L.; Gijbels, R. and Vertes, A.; *Anal. Chem.* 1991, **63**, 314.

42. Vertes, A. and Gijbels, R.; Laser Desorption Mass Analysis, in the Chemical Analysis 124, Ed. By Vertes, A.; Gijbels, R. and Adams, F., John Wiley and Sons Inc. p. 127.

43. Johnson, R. E.; Sundqvist, B. U. R.; *Rapid Commun. Mass Spectrom.*, 1991, **5**, 574.

44. Menzel, D. and Gomer, R.; *J. Chem. Phys.*, 1964, **41**, 3311.

45. Antoniewicz, P. R.; *Phys. Rev.* B, 1980, **21**, 3811.

46. Ingendoh, A.; Karas, M.; Hillenkamp, F.; Giessman, U.; *Int. J. Mass Spectrom. Ion Proc.* 1994, **131**, 345.

47. Grundwürmer, J. M.; Bönisch, M.; Kinsel, G. R.; Grotemeyer, J.; Schlag, E. W.; *Int. J. Mass Spectrom. Ion Proc.* 1994, **131**, 139.

48. Mamyrin, B. A.; Karatajev, V. J.; Shmikk, D. V. and Zagulin, V. A.; *Sov. Phys. JETP* 1973, **37**, 45.

49. Katalin, F. M.; Jennifer, M. C.; Michael, A. B.; Arnold, M. F.; Peter, J.; Marvin, L. V. and Alma, L. B.; *Anal. Chem.* 2000, **72**, 552.

50. Colburn, A. W.; Giannakopulos, A. E. and Derrick, P. J.; *Eur. J. Mass Spectrom.* 2000, **6**, 523.

51. John, F.; Daniel, H.; Johan, B.; Jacek, B.; Daniel, I.; *J. Biochem. Biophys. Methods.* 2004, **60**, 319.

52. Cornish, T. J.; Cotter, R. J.; *Rapid Commun. Mass Spectrom.* 1993, **7**, 1037.

53. Leonid, V. Z. and Barbara, J. G.; *Rapid Commun. Mass Spectrom.* 1998, **12**, 1273.

54. Stefan, B.; Christoph, M.; Franz, H. and Klaus, D.; *J. Am. Soc. Mass Spectrom.* 2002, **13**, 209.

55. Kaufmann, R.; Kirsch, D.; Tourmann, J. L.; Machold, J. and Hucho, F.; *Eur. Mass Spectrom.* 1995, **1**, 313.

56. Chaurand, P.; Kaufmann, R.; Lutzenkirchen, F.; Spengler, B.; Fournier, I.; Brunot, A.; Tabet, J. –C. and Bolbach, G.; in *Proceedings of the 45th Annual Conference*

on Mass Spectrometry and Allied Topics, Palm Springs, CA, June 1-5, 1997.

57. Zhou, J.; Ens, W., Standing, K. G. and Verentchikov, A.; *Rapid Commun. Mass Spectrom.* 1992, **6**, 671.
58. Spengler, B.; Kirsch, D.; Kaufmann, R. and Lemoine, J.; *J. Mass Spectrom*, 1995, **30**, 782.
59. Lemoine, J.; Chirat, F. and Domon, B.; *J. Mass Spectrom.* 1996, **31**, 908.
60. Harvey, D. J.; *J. Chromatogr. A* 1996, **720**, 429.
61. Harvey, D. J.; David, J.; Naven, T. J. P.; Kuster, B.; Bateman, R. H.; Green, M. R. and Critchley, G.; *Rapid Commun. Mass Spectrom.* 1995, **9**, 1556.
62. Huberty, M. C.; Vath, J. E.; Yu, W. and Martin, S. A.; *Anal. Chem.* 1993, **65**, 2791.
63. Karfmann, R.; Spengler, B.; Lütz enkirchen, F.; *Rapid Commun. Mass Spectrom* 1993; **7**: 902.
64. Fournier, I.; Marie, A.; Lesage, D.; Bolbach, G.; Fournier, F.; Tabet, J. C.; *Rapid Commun. Mass Spectrom.* 2002, **16**, 696.
65. Spengler, B; Kirsch, D.; Kaufmann, R.; *Rapid Commun. Mass Spectrom.* 1991, **5(4)**, 198.
66. Spengler, B.; Kirsch, D.; Kaufmann, R.; Jaeger, E.; *Rapid Commun. Mass Spectrom.* 1992, **6(2)**, 105.
67. Spengler, B.; Kirsch, D.; Kaufmann, R.; *J. Phys. Chem.* 1992, **96(24)**, 9678.
68. Spengler, B.; *J. Mass Spectrom.* 1997, **32**, 1019
69. Della-negra, S. and Beyec, Y. Le; *Anal. Chem.* 1985, **57**, 2035.
70. Tang, X.; Ens, W.; Standing, K. G. and Westmore, J. B.; *Anal. Chem.* 1988, **60**, 1791.
71. Tang, X.; Beavis, R.; Ens, W.; Lafortune, F.; Schueler, B. and Standing, K. G.; *Int. J. Mass Spectrom. Ion Processes* 1988, **85**, 43.
72. Cordero, M. M.; Cornish, T. J.; Cotter, R. J. and Lys, I. A.; *Rapid Commun. Mass Spectrom.* 1995, **9**, 1356.
73. Cotter, R. J.; Iltchenko, S.; Wang, D. X.; *Int. J. Mass Spectrom*, 2005, **240**, 169.
74. Qin, J.; and Chait, R. T.; *Int. J. Mass Spectrom.* 1999, **190/191**, 313.

75. Kleinova, M.; Belgacem, O.; Pock, K.; Rizzi, A.; Buchacher, A. and Allmaier, G.; *Rapid Commun. Mass Spectrom.* 2005, **19**, 2965.

76. Wiley, W. C. and Mclaren, L. H.; *Rev. Sci. Instrum.* 1955, **26**, 1150.

77. Brown R, Lennon J.; *Anal. Chem.* 1995, **67**, 3990.

78. Whittal, R. M.; Schriemer, D. C. and Li, L.; *Anal. Chem.* 1997, **69**, 2734.

79. Beavis, R. C. and Chait, B. T.; *Chem. Phys. Lett.* 1991, **5**, 479.

80. Pan, Y. and Cotter, R. J.; *Org. Mass Spectrom.* 1992, **27**, 3.

81. Lennon, J. J. and Brown, R. S.; Proceedings of *the 42nd Annual Conference on Mass Spectrometry and Allied Topics*, Chicago, IL, ASMS, Santa FE, 1994, p.501.

82. Colby, S. M.; King, T. B. and Reilly, J. P.; *Rapid Commun. Mass Spectrom.* 1994, **8**, 865.

83. Brown, R. S. and Lennon, J. J.; *Anal. Chem.* 1995, **67**, 1998.

84. Whittal, R. M. and Li, L.; *Anal. Chem.* 1995, **67**, 1950.

85. Vstal, M. L.; Juhasz, P. and Martin, S. A.; *Rapid Commun. Mass Spectrom.* 1995, **9**, 1044.

86. Juhasz P.; Roskey, M. T., Smirnov, I. P.; Haff, L. A.; Vestal, M. L. and Martin, S. A.; *Anal. Chem.* 1996, **68**, 941.

87. Schey, K.; Cooks, R. G.; Grix, R. and Wollnik, H.; *Int. J. MassSpectrom. Ion Processes.* 1987, **77**, 49.

88. Rinnen, K. –D.; Kliner, D. A. V.; Blake, R. S. and Zare, R. N.; *Rev. Sci. Instrum.* 1989, **60**, 717.

89. LaiHing, K.; Cheng, P. Y.; Taylor, T. G.; Willey, K. F.; Peschke, M. and Duncan, M. A.; *Anal. Chem.* 1989, **61**, 1458.

90. Brechignac, C.; Cahuzac, P.; Leygnier, J. and Weiner, J.; *J. Chem. Phys.* 1989, **90**, 1492.

91. Jardine, D. R.; Morgan, J.; Alderdice, D. S. and Derrick, P. J.; *Org. Mass Spectrom.* 1992, **27**, 1077.

92. Williams, R. E.; Fang, L. and Zare, N. R.; *Int. J. Mass Spectrom. Ion Processes* 1993, **123**, 233.

93. Weinkauf, R.; Walter, K.; Weickhardt, C.; Boesl, U. and Schlag, E. W.; *Z. Naturforsch.* 1989, A**44**, 1219.

94. Cordero, M. M.; Cornish, T. J.; Cotter, R. J. and Lys, I. A.; *Rapid Commun. Mass Spectrom.* 1995, **9**, 1356.

95. Vlasak, P. R.; Beussman, D. J.; Davenport, M. R. and Enke, C. G.; *Rev. Sci. Instrum.* 1996, **67,** 68.

96. Haberland, H.; Kornmeier, H.; Ludewigt, C. and Risch, A.; *Rev. Sci. Instrum.* 1991, **62,** 2368.

97. Stoermer, C. W.; Gilb, S.; Friedrich, J.; Schooss, D. and Dappes M. M.; *Rev. Sci. Instrum.* 1998, **69,** 1661.

98. Piyadasa, C. K. G.; Hakansson, P.; Ariyaratne, T. R. and Barofsky D. F.; *Rapid Commun. Mass Spectrom.* 1998, **12**, 1655.

99. SIMION 3D Version 6.0 User's Manual, David A. Dahl, INEL-95/0403 Rev.4.

100. Geno, P. W. and McFarlane, R. D.; *Int. J. Mass Spectrom. Ion Precesses,* 1989, **92**, 195.

101. Barofsky, D. F.; Brinkmalm, G.; Hakansson, P. and Sundqvist, B.; *Int. J. Mass Spectrom. Ion Precesses,* 1994, **131**, 283.

102. Roepstorff, P. and Fohimann J.; *Biomad. Mass Spectrom.* 1984, **11**, 601.

103. Johnson, R. S.; Martin, S. A. and Biemann K.; *Int. J. Mass Spectrom. Ion Processes*, 1988, **86**, 137.

104. Yates, J. R.; *Electrophoresis* 1998, **19**, 893.

105. Mann, M.; Wilm, M.; *Anal. Chem.* 1994, **66**, 4390.

106. Fenyo, D.; Qin, J.; Chait, B. T.; *Electrophoresis* 1998, **19**, 998.

107. Amott, D.; Henzel, W. J.; Stults, J. T.; *Electrophoresis* 1998, **19**, 968.

108. http://www.chm.bris.ac.uk/ms/theory/cid-fragmentation.html.

109. Appelhans, A.D.; Dahl, D.A.; *Int. J. Mass Spectrom.* 2002, **216**, 269-284.

110. Mamyrin, B. A.; USSR Patent No. 198, 034, 1996.

111. Mamyrin B. A.; Darataev, V. I.; Shmikk, D. V.; Zagulin, V. A.; *Sov. Phys. JETP*, 1973, **37**, 45.

112. Karataev, V. I.; Mamyrin, B. A.; Shmikk, D. V.; *J. Tech. Phys.* 1971, **16**, 1498.

113.Yoshida, Y. U. S. Patent 4,625,112, 25, November 1986.

114.Doroshenko, V. M.; Cotter, R. J.; *J. Mass Spectrom* 1998, **33**, 305.

115.Giannakopulos, A. E.; Thomas, B.; Colburn, A. W.; Reynolds, D. J.; Raptakis, E. N.; Makarov, A. A.; Derrick, P. J.; *Rev. Sci. Instrum.* 2002, **73**, 2115.

116.Cornish, T. J.; Cotter, R. J.; *Rapid Commun. Mass Spectrom.* 1994, **8**, 781.

117.Cordero, M. M.; Cornish, T. J.; Cotter, R. J.; *Rapid Commun. Mass Spectrom.* 1995, **9**, 1356.

118.Amina, S. W.; Little, D. P.; Cornish T.; Cotter, R. J.; Daniel, P. L.; *J. Mass Spectrom. Soc. Jpn.* 1998, **46**, 91.

Appendix 1 User program for time ion selection

```
defa start_time_µsec 0
defa end_time_µsec 0
defa left_edge_amu 60.0
defa right_edge_amu 43.0
defa target_mass_amu 1347.0
defa KE_ion_ev
1.9e4
defa target_velocity_m_s 0
defa number_tstep 20.0
defa pulse_vol 700.0
defa gradient_vol_ns 0
defa ion_totalnumber 270.0
defa center_of_selector_mm 491.0
defa duration_µsec 0
defa distance_mm 485.0
defa center_detector_mm 24.5
defa R_mm 5.0
defa int_0 0
defa int_1 0
defa int_2 0
defa int_3 0
defa int_4 0
defa int1 0
defa int2 0
defa int3 0
defa int4 0
defa del_m 1.0

seg tstep_adjust
  rcl KE_ion_ev 1.6e-19 * 2.0 *
  rcl target_mass_amu 1.0e-3 * 6.02e23 / /
sqrt
  sto target_velocity_m_s
  2.0 x><y / 1000.0 *
  rcl number_tstep /
  sto ion_time_step

seg fast_adjust
  rcl ion_px_mm
  480.0 x>y exit
  x><y 501.0
  x<y exit
  rcl center_of_selector_mm
  rcl target_velocity_m_s / 1000.0 *
  sto center
  rcl KE_ion_ev 2.0 * 1.6e-19 * sqrt
  rcl center_of_selector_mm 0.001 *
  x><y / sto constant
  rcl target_mass_amu
  rcl left_edge_amu - 0.001 * 6.02e23 / sqrt
  rcl constant * 1.0e6 *
  sto start_time_µsec
  rcl center
  x><y - sto left
  rcl target_mass_amu
  rcl right_edge_amu + 0.001 * 6.02e23 / sqrt
  rcl constant * 1.0e6 *
  sto end_time_µsec
  rcl center -
  sto right
  rcl right
  rcl left +
  0.04 -
  sto duration_µsec
  rcl start_time_µsec
  rcl ion_time_of_flight
  x<y exit
  rcl pulse_vol 0.02 /
  sto gradient_vol_ns
  rcl start_time_µsec 0.02 +
  rcl ion_time_of_flight
  x>y goto lbl01
  rcl start_time_µsec -
  rcl gradient_vol_ns *
  rcl pulse_vol
  x><y -
  sto adj_elect03
  chs sto adj_elect02
  exit
  lbl lbl01
```

```
    rcl start_time_µsec 0.02 +
    rcl duration_µsec +
    rcl ion_time_of_flight
    x>y goto lbl02
    0 sto adj_elect02
    0 sto adj_elect03
    exit
    lbl lbl02
    rcl start_time_µsec 0.04 +
    rcl duration_µsec +
    rcl ion_time_of_flight
    x>y goto lbl03
    rcl start_time_µsec 0.02 +
    rcl duration_µsec +
    rcl ion_time_of_flight
    x><y -
    rcl gradient_vol_ns *
    sto adj_elect05
    chs sto adj_elect04
    0 sto adj_elect02
    0 sto adj_elect03
    exit
    lbl lbl03
    rcl pulse_vol
    sto adj_elect05
    sto adj_elect03
    chs sto adj_elect04
    sto adj_elect02

seg terminate
    rcl ion_py_mm
    rcl center_detector_mm - abs
    rcl R_mm
    x<y goto lbl04
    rcl target_mass_amu
    rcl ion_mass
    x<y goto lbl05
    x>y goto lbl06
    rcl int_0 1.0 +
    sto int_0
    goto lbl04
    lbl lbl05
    rcl target_mass_amu
    rcl del_m -
    rcl ion_mass
    x<y goto lbl07
    rcl int_1 1.0 +
    sto int_1
    goto lbl04
    lbl lbl07
    rcl target_mass_amu
    rcl del_m 2.0 * -
    rcl ion_mass
    x<y goto lbl08
    rcl int_2 1.0 +
    sto int_2
    goto lbl04
    lbl lbl08
    rcl target_mass_amu
    rcl del_m 3.0 * -
    rcl ion_mass
    x<y goto lbl11
    rcl int_3 1.0 +
    sto int_3
    goto lbl04
    lbl lbl11
    rcl int_4 1.0 +
    sto int_4
    goto lbl04
    lbl lbl06
    rcl target_mass_amu
    rcl del_m +
    rcl ion_mass
    x>y goto lbl09
    rcl int1 1.0 +
    sto int1
    goto lbl04
    lbl lbl09
    rcl target_mass_amu
    rcl del_m 2.0 * +
    rcl ion_mass
    x>y goto lbl10
    rcl int2 1.0 +
    sto int2
    goto lbl04
    lbl lbl10
    rcl target_mass_amu
    rcl del_m 3.0 * +
```

```
  rcl ion_mass
  x>y goto lbl12
  rcl int3 1.0 +
  sto int3
  lbl lbl12
  rcl int4 1.0 +
  sto int4
  lbl lbl04
  rcl ion_number
  rcl ion_totalnumber
  x>y exit
  rcl int_1
  rcl int_2
  rcl int_3
  rcl int_4
  mess ;int_4=# int_3=# int_2=# int_1=#
  rcl int_0
  mess ;int0=#
  rcl int4
  rcl int3
  rcl int2
  rcl int1
  mess ;int1=# int2=# int3=# int4=#
  rcl duration_µsec
  mess ;duration=#µsec
  rcl end_time_µsec
  rcl start_time_µsec
  rcl right_edge_amu
  rcl left_edge_amu
  mess  ;left=#amu  right=#amu  start=#µsec
end=#µsec
  rcl target_mass_amu
  rcl distance_mm
  rcl target_velocity_m_s / 1000.0 *
  rcl distance_mm 12.0 +
  rcl target_velocity_m_s / 1000.0 *
  mess    ;ion_exit=#µsec    ion_enter=#µsec
target=#
  rcl start_time_µsec
  rcl target_velocity_m_s * 1000.0 /
  rcl end_time_µsec
  rcl target_velocity_m_s * 1000.0 /
  mess ;pulse_end=#mm pulse_start=#mm
  rcl target_mass_amu
  rcl del_m 2.0 * -
  rcl target_mass_amu
  rcl del_m 1.0 * -
  rcl target_mass_amu
  rcl target_mass_amu
  rcl del_m 1.0 * +
  rcl target_mass_amu
  rcl del_m 2.0 * +
  rcl target_mass_amu
  rcl del_m 3.0 * +
  rcl target_mass_amu
  rcl del_m 4.0 * +
  mess ;# # # # # # #
  rcl target_mass_amu
  rcl del_m 4.0 * -
  rcl target_mass_amu
  rcl del_m 3.0 * -
  mess ;# #
```

Appendix 2 User program for gas collision

```
;Definition
defa gas_mass       4.0 ;collision gas mass
defa ratio          0.9
defa T_k            293.0       ;temperature
defa mean_free_path_mm    4.0
defa step_per_mfp       20.0
defa R              8.314       ;gas constant
defa k          1.38e-20 ;boltzman constant
defa pi             3.14159     ;pi
defa d          2.3e-10     ;diameter of gas atom
defa p     4e-1   ;presure in the collision cell
defs collisions   0    ;number of collision
defa KE_pre_ion   0    ;ke of precursor ion
defa KE_frag_ion  0    ;ke of fragment ion
defa frag_mass    0     ;mass of fragment
defa dispersion     0 ;ion space dispersion
defa ion_totalnumber    51.0  ;total   number
of ions
defa  parent_ion_mass  5.734e3      ;precursor
ion mass
defa fragment_number  0
defa dispersion_sqr     0
defa ave_disp           0
defa ave_disp_sqr       0
defa tof_sum          0 ;sum of tof of fragment
defa ave_tof_fragment  0            ;average
tof of fragment
defa tof_sqr_sum   0;sum of fragment tof
sqr
defa tof_parent_sum 0;sum of parent ion tof
defa parent_num_sum   0          ;sum    of
parention number

seg initialize

seg tstep_adjust

                ;calculate mfp

  rcl k rcl T_k *
  rcl d entr * rcl pi * rcl p * 1.414 * /
  sto mean_free_path_mm
        ;new mfp

  rcl ion_vz_mm
        ;load velocity vector
  rcl ion_vy_mm
  rcl ion_vx_mm
  >p3d
      ;convert to polar coords
  sto v
  rcl mean_free_path_mm
  rcl v / rcl step_per_mfp /
  sto tmax
  rcl ion_time_step
  x<y exit
  rcl tmax      ;else use tmax for time step
  sto ion_time_step
  exit

                ;collision simulation
seg other_actions
  rcl ion_px_mm 207.0 x>y exit        ;make
sure collisions occur in collision cell
  rcl ion_px_mm 267.0 x<y exit
  rcl mean_free_path_mm
  rcl ion_vz_mm
  rcl ion_vy_mm
  rcl ion_vx_mm
  >p3d
  sto v
  rlup sto az
  rlup sto el
  rcl ion_mass rcl v >ke            ;ke     of
precursor ion
  sto KE_pre_ion
  rcl v rcl ion_time_step *         ;test    for
collision
  rcl mean_free_path_mm / chs e^x
  1 x<>y -
     ;(1-e(-d/fp))
  rand
```

```
x>y goto skip2
rcl collisions 1 +
sto collisions
   ;collision number + 1
0.99999 rand *   ;get a random radius r
abs x>0 sqrt
asin
sto impact_angle_rad
    ;get impact angle
rcl ion_mass rcl gas_mass -
    ;calculate ion attenuated velocity
rcl ion_mass rcl gas_mass + /
x=0 0.0000001
rcl v * rcl impact_angle_rad cos * sto vr
rcl v rcl impact_angle_rad sin * sto vt
rcl vr rcl vr * rcl vt rcl vt * + sqrt sto v
  ;ion attenuated velocity
rcl impact_angle_rad rcl vt rcl vr / atan -
>deg                ;deflection angle
abs sto defl_angle
90 +
360 rand *
rcl v
>r3d
-90 >elr
rcl el >elr
rcl az >azr
sto ion_vx_mm
rlup sto ion_vy_mm
rlup sto ion_vz_mm
rand 0.5 x>y goto skip1
    ;determine whether to fragment
rcl ion_mass
    ;calculate fragment mass
rcl ratio *
sto ion_mass
lbl skip1
rcl ion_mass     ;calculate fragment KE
1.66e-27 *
rcl v 1000 * entr * * 2 / 1.602177e-19 /
sto KE_frag_ion
rcl ion_py_mm
rcl ion_px_mm
rcl KE_frag_ion
  rcl defl_angle
  rcl ion_mass
  rcl collisions
  rcl ion_number
  message ;ion=# col=# frg=# def=#
kefrg=#ev x=#mm y=#mm
  lbl skip2

seg terminate
  rcl ion_number
  rcl ion_totalnumber x=y goto skip5
  rcl ion_px_mm
  1160.0 x>y exit
  lbl skip5
  rcl ion_py_mm abs
  rcl dispersion +      ;calculate sum of
space dispersion
  sto dispersion        ;sum of space
dispersion
  rcl ion_py_mm
  rcl ion_px_mm
  rcl ion_time_of_flight
  rcl ion_vx_mm
  rcl ion_mass
  rcl ion_number
  message ;ion=# frag=# v=#mm/μsec
t=#μsec x=# y=#mm
  rcl ion_mass
  rcl parent_ion_mass x!=y goto skip4
  rcl parent_num_sum 1 +  ;calculate sum
of parent ion
  sto parent_num_sum      ;sum of parent
ion
  rcl ion_time_of_flight ;calculate sum of
tof_parent ion
  rcl tof_parent_sum +
  sto tof_parent_sum      ;sum of
tof_parent ion
  lbl skip4
  rcl ion_py_mm
  enter *
  rcl dispersion_sqr +
  sto dispersion_sqr
  rcl parent_ion_mass rcl ratio *
```

```
  rcl ion_mass x!=y goto skip3
  rcl fragment_number 1 +      ;calculate sum
of fragment
  sto fragment_number  ; sum of fragment
  rcl ion_time_of_flight
  rcl tof_sum +
  sto tof_sum          ;sum of tof_fragment
  rcl ion_time_of_flight
  enter *
  rcl tof_sqr_sum +
  sto tof_sqr_sum
  lbl skip3

       ;judge whether the last ion
  rcl ion_number
  rcl ion_totalnumber x>y exit
  rcl tof_sum
  rcl fragment_number /
  sto ave_tof_fragment
  enter * sto ave_tof_sqr
  rcl dispersion
     ;calculate stadev of space dispersion
  rcl ion_totalnumber /
  sto ave_disp
  enter * sto ave_disp_sqr
  rcl ave_disp
  rcl dispersion * -2.0 *
  rcl dispersion_sqr +
  rcl ion_totalnumber /
  rcl ave_disp_sqr + sqrt          ;stadev   of
space dispersion
  rcl ave_disp
  rcl mean_free_path_mm
  rcl fragment_number
  message        ;frg_num=#        mfp=#mm
ave_disp=#mm stadev=#mm
  rcl tof_parent_sum
  rcl parent_num_sum /
  sto tof_parent_ave
  rcl ave_tof_fragment
  rcl tof_sum * -2.0 *
  rcl tof_sqr_sum +
  rcl fragment_number /
  rcl ave_tof_sqr + sqrt
  rcl ave_tof_fragment
  message       ;average_tof_fragment=#μsec
stadev=#μsec
  rcl tof_parent_ave
  message ;average_tof_parent=#μsec
```

Appendix 3 Mathematica program used in calculation for curved-field reflectron

```
e3 = 19000;
Δe3 = 12;
e1 = (m1/m3) (e3 - v) + v;
Δe1 = (m1/m3) × Δe3;
e2 = (m2/m3) (e3 - v) + v;
Δe2 = (m2/m3) × Δe3;
v1 = R × Cos[(α/180) π];
v2 = v1 - 20000;
x1 = √(R^2 - v1^2);
x2 = √(R^2 - v2^2);
θ = (1/180) π;
equation = f[x_] = v1 - √(R^2 - ((x2 - x1)/L x + x1)^2);
solution = Solve[Cos[θ] × Cos[θ] × z == f[x], {x}];
y[z_] = solution[[2, 1, 2]];
Off[NIntegrate::precw]
Off[NIntegrate::ncvb]
a1[l_] = N[1000 l / (Cos[θ] √(2 e1 × 1.6×10^-19 ÷ (m1 ÷ (6.02×10^26)))) +
  2 × ∫_0^y[e1] 1000 / (Cos[θ] √((2 × (e1 + 0.0000000001 - equation) × 1.6×10^-19) / (m1 ÷ (6.02×10^26)))) dx, 20];
a11[l_] = a1[l] × a1[l];
a2[l_] = N[1000 l / (Cos[θ] √(2 e2 × 1.6×10^-19 ÷ (m2 ÷ (6.02×10^26)))) +
  2 × ∫_0^y[e2] 1000 / (Cos[θ] √((2 × (e2 + 0.0000000001 - equation) × 1.6×10^-19) / (m2 ÷ (6.02×10^26)))) dx, 20];
a21[l_] = a2[l] × a2[l];
a3[l_] = N[1000 l / (Cos[θ] √(2 e3 × 1.6×10^-19 ÷ (m3 ÷ (6.02×10^26)))) +
  2 × ∫_0^y[e3] 1000 / (Cos[θ] √((2 × (e3 + 0.0000000001 - equation) × 1.6×10^-19) / (m3 ÷ (6.02×10^26)))) dx, 20];
a31[l_] = a3[l] × a3[l];

b1[l_] = N[1000 l / (Cos[θ] √(2 (e1 + Δe1) × 1.6×10^-19 ÷ (m1 ÷ (6.02×10^26)))) +
  2 × ∫_0^y[e1+Δe1] 1000 / (Cos[θ] √((2 × (e1 + Δe1 + 0.0000000001 - equation) × 1.6×10^-19) / (m1 ÷ (6.02×10^26)))) dx, 20];
b11[l_] = b1[l] × b1[l];
b2[l_] = N[1000 l / (Cos[θ] √(2 (e2 + Δe2) × 1.6×10^-19 ÷ (m2 ÷ (6.02×10^26)))) +
  2 × ∫_0^y[e2+Δe2] 1000 / (Cos[θ] √((2 × (e2 + Δe2 + 0.0000000001 - equation) × 1.6×10^-19) / (m2 ÷ (6.02×10^26)))) dx, 20];
b21[l_] = b2[l] × b2[l];
b3[l_] = N[1000 l / (Cos[θ] √(2 (e3 + Δe3) × 1.6×10^-19 ÷ (m3 ÷ (6.02×10^26)))) +
  2 × ∫_0^y[e3+Δe3] 1000 / (Cos[θ] √((2 × (e3 + Δe3 + 0.0000000001 - equation) × 1.6×10^-19) / (m3 ÷ (6.02×10^26)))) dx, 20];
```

```
b31[l_] = b3[l] × b3[l];

c1[l_] = N[1000 l / (Cos[θ] √(2 (e1 + 2×Δe1) × 1.6×10^-19 ÷ (m1 ÷ (6.02×10^26)))) +
  2× ∫_0^y[e1+2×Δe1] 1000 / (Cos[θ] √((2× (e1 + 2×Δe1 + 0.0000000001 - equation) × 1.6×10^-19) / (m1 ÷ (6.02×10^26)))) dx, 20];
c11[l_] = c1[l] × c1[l];
c2[l_] = N[1000 l / (Cos[θ] √(2 (e2 + 2×Δe2) × 1.6×10^-19 ÷ (m2 ÷ (6.02×10^26)))) +
  2× ∫_0^y[e2+2×Δe2] 1000 / (Cos[θ] √((2× (e2 + 2×Δe2 + 0.0000000001 - equation) × 1.6×10^-19) / (m2 ÷ (6.02×10^26)))) dx, 20];
c21[l_] = c2[l] × c2[l];
c3[l_] = N[1000 l / (Cos[θ] √(2 (e3 + 2×Δe3) × 1.6×10^-19 ÷ (m3 ÷ (6.02×10^26)))) +
  2× ∫_0^y[e3+2×Δe3] 1000 / (Cos[θ] √((2× (e3 + 2×Δe3 + 0.0000000001 - equation) × 1.6×10^-19) / (m3 ÷ (6.02×10^26)))) dx, 20];
c31[l_] = c3[l] × c3[l];

d1[l_] = N[1000 l / (Cos[θ] √(2 (e1 + 3×Δe1) × 1.6×10^-19 ÷ (m1 ÷ (6.02×10^26)))) +
  2× ∫_0^y[e1+3×Δe1] 1000 / (Cos[θ] √((2× (e1 + 3×Δe1 + 0.0000000001 - equation) × 1.6×10^-19) / (m1 ÷ (6.02×10^26)))) dx, 20];
d11[l_] = d1[l] × d1[l];
d2[l_] = N[1000 l / (Cos[θ] √(2 (e2 + 3×Δe2) × 1.6×10^-19 ÷ (m2 ÷ (6.02×10^26)))) +
  2× ∫_0^y[e2+3×Δe2] 1000 / (Cos[θ] √((2× (e2 + 3×Δe2 + 0.0000000001 - equation) × 1.6×10^-19) / (m2 ÷ (6.02×10^26)))) dx, 20];
d21[l_] = d2[l] × d2[l];
d3[l_] = N[1000 l / (Cos[θ] √(2 (e3 + 3×Δe3) × 1.6×10^-19 ÷ (m3 ÷ (6.02×10^26)))) +
  2× ∫_0^y[e3+3×Δe3] 1000 / (Cos[θ] √((2× (e3 + 3×Δe3 + 0.0000000001 - equation) × 1.6×10^-19) / (m3 ÷ (6.02×10^26)))) dx, 20];
d31[l_] = d3[l] × d3[l];

q1[l_] = N[1000 l / (Cos[θ] √(2 (e1 + 4×Δe1) × 1.6×10^-19 ÷ (m1 ÷ (6.02×10^26)))) +
  2× ∫_0^y[e1+4×Δe1] 1000 / (Cos[θ] √((2× (e1 + 4×Δe1 + 0.0000000001 - equation) × 1.6×10^-19) / (m1 ÷ (6.02×10^26)))) dx, 20];
q11[l_] = q1[l] × q1[l];
q2[l_] = N[1000 l / (Cos[θ] √(2 (e2 + 4×Δe2) × 1.6×10^-19 ÷ (m2 ÷ (6.02×10^26)))) +
  2× ∫_0^y[e2+4×Δe2] 1000 / (Cos[θ] √((2× (e2 + 4×Δe2 + 0.0000000001 - equation) × 1.6×10^-19) / (m2 ÷ (6.02×10^26)))) dx, 20];
q21[l_] = q2[l] × q2[l];
q3[l_] = N[1000 l / (Cos[θ] √(2 (e3 + 4×Δe3) × 1.6×10^-19 ÷ (m3 ÷ (6.02×10^26)))) +
  2× ∫_0^y[e3+4×Δe3] 1000 / (Cos[θ] √((2× (e3 + 4×Δe3 + 0.0000000001 - equation) × 1.6×10^-19) / (m3 ÷ (6.02×10^26)))) dx, 20];
q31[l_] = q3[l] × q3[l];
```

$$f1[l\_] = N\left[\frac{1000\,l}{\cos[\theta]\sqrt{2\,(e1+5\times\Delta e1)\times 1.6\times 10^{-19}+(m1+(6.02\times 10^{26}))}}+\right.$$
$$\left.2\times\int_0^{y[e1+5\times\Delta e1]}1000\Big/\left(\cos[\theta]\sqrt{\left(\frac{2\times(e1+5\times\Delta e1+0.0000000001-\text{equation})\times 1.6\times 10^{-19}}{m1+(6.02\times 10^{26})}\right)}\right)dx,\,20\right];$$

$$f11[l\_] = f1[l]\times f1[l];$$

$$f2[l\_] = N\left[\frac{1000\,l}{\cos[\theta]\sqrt{2\,(e2+5\times\Delta e2)\times 1.6\times 10^{-19}+(m2+(6.02\times 10^{26}))}}+\right.$$
$$\left.2\times\int_0^{y[e2+5\times\Delta e2]}1000\Big/\left(\cos[\theta]\sqrt{\left(\frac{2\times(e2+5\times\Delta e2+0.0000000001-\text{equation})\times 1.6\times 10^{-19}}{m2+(6.02\times 10^{26})}\right)}\right)dx,\,20\right];$$

$$f21[l\_] = f2[l]\times f2[l];$$

$$f3[l\_] = N\left[\frac{1000\,l}{\cos[\theta]\sqrt{2\,(e3+5\times\Delta e3)\times 1.6\times 10^{-19}+(m3+(6.02\times 10^{26}))}}+\right.$$
$$\left.2\times\int_0^{y[e3+5\times\Delta e3]}1000\Big/\left(\cos[\theta]\sqrt{\left(\frac{2\times(e3+5\times\Delta e3+0.0000000001-\text{equation})\times 1.6\times 10^{-19}}{m3+(6.02\times 10^{26})}\right)}\right)dx,\,20\right];$$

$$f31[l\_] = f3[l]\times f3[l];$$

$$g1[l\_] = N\left[\frac{1000\,l}{\cos[\theta]\sqrt{2\,(e1+6\times\Delta e1)\times 1.6\times 10^{-19}+(m1+(6.02\times 10^{26}))}}+\right.$$
$$\left.2\times\int_0^{y[e1+6\times\Delta e1]}1000\Big/\left(\cos[\theta]\sqrt{\left(\frac{2\times(e1+6\times\Delta e1+0.0000000001-\text{equation})\times 1.6\times 10^{-19}}{m1+(6.02\times 10^{26})}\right)}\right)dx,\,20\right];$$

$$g11[l\_] = g1[l]\times g1[l];$$

$$g2[l\_] = N\left[\frac{1000\,l}{\cos[\theta]\sqrt{2\,(e2+6\times\Delta e2)\times 1.6\times 10^{-19}+(m2+(6.02\times 10^{26}))}}+\right.$$
$$\left.2\times\int_0^{y[e2+6\times\Delta e2]}1000\Big/\left(\cos[\theta]\sqrt{\left(\frac{2\times(e2+6\times\Delta e2+0.0000000001-\text{equation})\times 1.6\times 10^{-19}}{m2+(6.02\times 10^{26})}\right)}\right)dx,\,20\right];$$

$$g21[l\_] = g2[l]\times g2[l];$$

$$g3[l\_] = N\left[\frac{1000\,l}{\cos[\theta]\sqrt{2\,(e3+6\times\Delta e3)\times 1.6\times 10^{-19}+(m3+(6.02\times 10^{26}))}}+\right.$$
$$\left.2\times\int_0^{y[e3+6\times\Delta e3]}1000\Big/\left(\cos[\theta]\sqrt{\left(\frac{2\times(e3+6\times\Delta e3+0.0000000001-\text{equation})\times 1.6\times 10^{-19}}{m3+(6.02\times 10^{26})}\right)}\right)dx,\,20\right];$$

$$g31[l\_] = g3[l]\times g3[l];$$

$$h1[l\_] = N\left[\frac{1000\,l}{\cos[\theta]\sqrt{2\,(e1+7\times\Delta e1)\times 1.6\times 10^{-19}+(m1+(6.02\times 10^{26}))}}+\right.$$
$$\left.2\times\int_0^{y[e1+7\times\Delta e1]}1000\Big/\left(\cos[\theta]\sqrt{\left(\frac{2\times(e1+7\times\Delta e1+0.0000000001-\text{equation})\times 1.6\times 10^{-19}}{m1+(6.02\times 10^{26})}\right)}\right)dx,\,20\right];$$

$$h11[l\_] = h1[l]\times h1[l];$$

$$h2[l\_] = N\left[\frac{1000\,l}{\cos[\theta]\sqrt{2\,(e2+7\times\Delta e2)\times 1.6\times 10^{-19}+(m2+(6.02\times 10^{26}))}}+\right.$$
$$\left.2\times\int_0^{y[e2+7\times\Delta e2]}1000\Big/\left(\cos[\theta]\sqrt{\left(\frac{2\times(e2+7\times\Delta e2+0.0000000001-\text{equation})\times 1.6\times 10^{-19}}{m2+(6.02\times 10^{26})}\right)}\right)dx,\,20\right];$$

$$h21[l\_] = h2[l]\times h2[l];$$

$$h3[l\_] = N\left[\frac{1000\,l}{\cos[\theta]\sqrt{2\,(e3+7\times\Delta e3)\times 1.6\times 10^{-19}+(m3+(6.02\times 10^{26}))}}+\right.$$
$$\left.2\times\int_0^{y[e3+7\times\Delta e3]}1000\Big/\left(\cos[\theta]\sqrt{\left(\frac{2\times(e3+7\times\Delta e3+0.0000000001-\text{equation})\times 1.6\times 10^{-19}}{m3+(6.02\times 10^{26})}\right)}\right)dx,\,20\right];$$

$$h31[l\_] = h3[l]\times h3[l];$$

$$i1[l\_] = N\left[\frac{1000\,l}{\cos[\theta]\sqrt{2\,(e1+8\times\Delta e1)\times 1.6\times 10^{-19}+(m1+(6.02\times 10^{26}))}}+\right.$$
$$\left.2\times\int_0^{y[e1+8\times\Delta e1]}1000\Big/\left(\cos[\theta]\sqrt{\left(\frac{2\times(e1+8\times\Delta e1+0.0000000001-\text{equation})\times 1.6\times 10^{-19}}{m1+(6.02\times 10^{26})}\right)}\right)dx,\,20\right];$$

$$i11[l\_] = i1[l] \times i1[l];$$

$$i2[l\_] = N\left[\frac{1000\,l}{\cos[\theta]\sqrt{2\,(e2+8\times\Delta e2)\times 1.6\times 10^{-19}\div(m2\div(6.02\times 10^{26}))}} + 2\times\int_0^{y[e2+8\times\Delta e2]} 1000\Big/\left(\cos[\theta]\sqrt{\left(\frac{2\times(e2+8\times\Delta e2+0.0000000001-\text{equation})\times 1.6\times 10^{-19}}{m2\div(6.02\times 10^{26})}\right)}\right) dx,\ 20\right];$$

$$i21[l\_] = i2[l] \times i2[l];$$

$$i3[l\_] = N\left[\frac{1000\,l}{\cos[\theta]\sqrt{2\,(e3+8\times\Delta e3)\times 1.6\times 10^{-19}\div(m3\div(6.02\times 10^{26}))}} + 2\times\int_0^{y[e3+8\times\Delta e3]} 1000\Big/\left(\cos[\theta]\sqrt{\left(\frac{2\times(e3+8\times\Delta e3+0.0000000001-\text{equation})\times 1.6\times 10^{-19}}{m3\div(6.02\times 10^{26})}\right)}\right) dx,\ 20\right];$$

$$i31[l\_] = i3[l] \times i3[l];$$

$$j1[l\_] = N\left[\frac{1000\,l}{\cos[\theta]\sqrt{2\,(e1+9\times\Delta e1)\times 1.6\times 10^{-19}\div(m1\div(6.02\times 10^{26}))}} + 2\times\int_0^{y[e1+9\times\Delta e1]} 1000\Big/\left(\cos[\theta]\sqrt{\left(\frac{2\times(e1+9\times\Delta e1+0.0000000001-\text{equation})\times 1.6\times 10^{-19}}{m1\div(6.02\times 10^{26})}\right)}\right) dx,\ 20\right];$$

$$j11[l\_] = j1[l] \times j1[l];$$

$$j2[l\_] = N\left[\frac{1000\,l}{\cos[\theta]\sqrt{2\,(e2+9\times\Delta e2)\times 1.6\times 10^{-19}\div(m2\div(6.02\times 10^{26}))}} + 2\times\int_0^{y[e2+9\times\Delta e2]} 1000\Big/\left(\cos[\theta]\sqrt{\left(\frac{2\times(e2+9\times\Delta e2+0.0000000001-\text{equation})\times 1.6\times 10^{-19}}{m2\div(6.02\times 10^{26})}\right)}\right) dx,\ 20\right];$$

$$j21[l\_] = j2[l] \times j2[l];$$

$$j3[l\_] = N\left[\frac{1000\,l}{\cos[\theta]\sqrt{2\,(e3+9\times\Delta e3)\times 1.6\times 10^{-19}\div(m3\div(6.02\times 10^{26}))}} + 2\times\int_0^{y[e3+9\times\Delta e3]} 1000\Big/\left(\cos[\theta]\sqrt{\left(\frac{2\times(e3+9\times\Delta e3+0.0000000001-\text{equation})\times 1.6\times 10^{-19}}{m3\div(6.02\times 10^{26})}\right)}\right) dx,\ 20\right];$$

$$j31[l\_] = j3[l] \times j3[l];$$

$$k1[l\_] = N\left[\frac{1000\,l}{\cos[\theta]\sqrt{2\,(e1+10\times\Delta e1)\times 1.6\times 10^{-19}\div(m1\div(6.02\times 10^{26}))}} + 2\times\int_0^{y[e1+10\times\Delta e1]} 1000\Big/\left(\cos[\theta]\sqrt{\left(\frac{2\times(e1+10\times\Delta e1+0.0000000001-\text{equation})\times 1.6\times 10^{-19}}{m1\div(6.02\times 10^{26})}\right)}\right) dx,\ 20\right];$$

$$k11[l\_] = k1[l] \times k1[l];$$

$$k2[l\_] = N\left[\frac{1000\,l}{\cos[\theta]\sqrt{2\,(e2+10\times\Delta e2)\times 1.6\times 10^{-19}\div(m2\div(6.02\times 10^{26}))}} + 2\times\int_0^{y[e2+10\times\Delta e2]} 1000\Big/\left(\cos[\theta]\sqrt{\left(\frac{2\times(e2+10\times\Delta e2+0.0000000001-\text{equation})\times 1.6\times 10^{-19}}{m2\div(6.02\times 10^{26})}\right)}\right) dx,\ 20\right];$$

$$k21[l\_] = k2[l] \times k2[l];$$

$$k3[l\_] = N\left[\frac{1000\,l}{\cos[\theta]\sqrt{2\,(e3+10\times\Delta e3)\times 1.6\times 10^{-19}\div(m3\div(6.02\times 10^{26}))}} + 2\times\int_0^{y[e3+10\times\Delta e3]} 1000\Big/\left(\cos[\theta]\sqrt{\left(\frac{2\times(e3+10\times\Delta e3+0.0000000001-\text{equation})\times 1.6\times 10^{-19}}{m3\div(6.02\times 10^{26})}\right)}\right) dx,\ 20\right];$$

$$k31[l\_] = k3[l] \times k3[l];$$

$$r1[l\_] = a1[l] + b1[l] + c1[l] + d1[l] + q1[l] + f1[l] + g1[l] + h1[l] + i1[l] + j1[l] + k1[l];$$

$$r2[l\_] = a2[l] + b2[l] + c2[l] + d2[l] + q2[l] + f2[l] + g2[l] + h2[l] + i2[l] + j2[l] + k2[l];$$

$$r3[l\_] = a3[l] + b3[l] + c3[l] + d3[l] + q3[l] + f3[l] + g3[l] + h3[l] + i3[l] + j3[l] + k3[l];$$

```
n1[l_] = Expand[r1[l] / 11];
n2[l_] = Expand[r2[l] / 11];
n3[l_] = Expand[r3[l] / 11];

n11[l_] = Expand[n1[l] * n1[l]];
n21[l_] = Expand[n2[l] * n2[l]];
n31[l_] = Expand[n3[l] * n3[l]];

o1[l_] = Expand[a11[l] + b11[l] + c11[l] + d11[l] + q11[l] + f11[l] + g11[l] + h11[l] + i11[l] + j11[l] + k11[l]];
o2[l_] = Expand[a21[l] + b21[l] + c21[l] + d21[l] + q21[l] + f21[l] + g21[l] + h21[l] + i21[l] + j21[l] + k21[l]];
o3[l_] = Expand[a31[l] + b31[l] + c31[l] + d31[l] + q31[l] + f31[l] + g31[l] + h31[l] + i31[l] + j31[l] + k31[l]];

p1[l_] = n1[l] / Sqrt[Expand[o1[l] / 11] - n11[l]];
p2[l_] = n2[l] / Sqrt[Expand[o2[l] / 11] - n21[l]];
p3[l_] = n3[l] / Sqrt[Expand[o3[l] / 11] - n31[l]];

solution01 = Solve[p1'[l] == 0];
solution02 = Solve[p2'[l] == 0];
solution03 = Solve[p3'[l] == 0];
data = {solution01[[1, 1, 2]], solution02[[1, 1, 2]], solution03[[1, 1, 2]]}
Mean[data]
Sqrt[Variance[data]]
p1[solution01[[1, 1, 2]]];
p2[solution02[[1, 1, 2]]];
p3[solution03[[1, 1, 2]]];
Mean[data] / Sqrt[Variance[data]]
Plot[{p1[l], p2[l], p3[l]}, {l, -50, 500}, PlotRange → All];
```